Split-Hopkinson Pressure Bar Testing and Constitutive Model Evaluation for 7050-T7451 Aluminum, IN718 Superalloy, & 300M Steel

Jason Gao



Department of Mining and Materials Engineering McGill University, Montreal Quebec, Canada

A thesis submitted to McGill University in partial fulfillment of the requirements of the degree of Master of Engineering

© Jason Gao, 2017

Abstract

The understanding of material's response to high strain rate loading is essential for a range of applications such as high-speed forming, machining, crashworthiness of automotive structures, and similarly ballistics impact performance of armor and engine fan blade containment structures. For reliable numerical modelling of such processes, accurate high strain rate materials data and constitutive models describing the strain rate dependence of the material's stress-strain response are necessary. The Split-Hopkinson pressure bar (SHPB) has been a commonly used method for evaluating the high strain rate response of materials in the range of $10^2 \mathrm{s}^{-1}$ to $10^4 \mathrm{s}^{-1}$. Measurements from this technique is useful for producing precise data to calibrate constitutive models, and to facilitate modeling and simulation of high strain rate processes.

In this study, a compressive Split-Hopkinson pressure bar (SHPB) setup was used to evaluate the stress-strain response for three alloys, Aluminum 7050-T7451, Inconel 718, and 300M steel for the modelling of shot-peening, cold-work surface modification process. Shot peening involves impacting a material's surface with spherical media to generate sub-surface deformed layers containing strain hardening and residual stress. During the peening process, strain rates of the peened material can reach up to 10^5s^{-1} to 10^6s^{-1} , which is greater than strain rates measurable using the SHPB. To enable a higher strain rate response, SHPB tests were carried out at a low temperature by cooling to represent the response of an increase in strain rate through the equivalent effect of lower temperatures and higher strain rates on the measured stress. In addition, SHPB tests were carried out at specific strain rate and temperature conditions for calibrating constitutive models. For Aluminum 7050-T7451, stress-strain results were measured between strain rates of 8×10²s⁻¹ to 2.8×10³s⁻¹ at 25°C. Temperature dependent tests were from -110°C to 200°C compared at 2×10³s⁻¹. Results obtained for IN718 were at 2.7×10^3 s⁻¹, 4×10^3 s⁻¹ and 25° C, and at temperatures of -110°C and 500°C tested at 4×10^3 s⁻¹. For 300M steel, results were obtained at 2.4×10³s⁻¹, 3×10³s⁻¹ and 25°C. Temperature-dependent results were measured at -70°C, 200°C, and 500°C, and at a strain rate of 2.4×10³s⁻¹.

i

From SHPB tests, Aluminum 7050-T7451 stress-strain results showed an increase in strain rate sensitivity above 10^3s^{-1} at 25°C . For varying temperature tests measured at $2 \times 10^3 \text{s}^{-1}$, the stress-strain at -110°C showed higher strength and initial strain hardening rate compared to the result at 25°C. Negative strain hardening occurred for results at 100°C and 200°C and the rate of thermal softening increased at 200°C.

IN718 exhibited a moderate increase in strength from $10^3 s^{-1}$ to $4 \times 10^3 s^{-1}$ at 25° C. For varying temperature tests at $4 \times 10^3 s^{-1}$, the strength increased at -110°C relative to 25° C and the strain hardening rate was comparable in both tests. At 500°C, the measured strain hardening rate was notably lower compared to the result at 25° C.

300M steel alloys tested at 3×10s⁻¹ and 25°C displayed stress saturation and slight negative strain hardening with increasing strain. At a strain rate of 2.4×10³s⁻¹, the strength at -70°C was greater than that at 25°C, and strain hardening trends were similar for both conditions. Stress-strain response at 200°C displayed an initial increase in strain hardening prior to softening, and stress saturation at 500°C was comparable to the result at 25°C. In addition, shear failure occurred in samples tested at varying temperatures and strain to failure was comparable in all conditions.

The SHPB results attained at high strain rates, varying temperatures as well as quasi-static data at 25°C, were used to evaluate the Johnson Cook (J-C) model parameter for each alloy. A modified Johnson Cook model with Voce strain hardening law and a modified Khan-Huang-Liang (KHL) model were evaluated and provided closer fit to Aluminum 7050-T7451 and IN718 results, respectively compared to the J-C model. For 300M steel, a modified J-C model with Cowper Symonds strain rate form provided comparable correlation to experiments as the J-C model. The J-C model, and models with more adequate correlations were used to extrapolate the stress at higher strain rates to represent the response encountered during peening. In addition, the fitted models were used to estimate the corresponding strain rate at 25°C of the low temperature SHPB test result for each alloy.

Résumé

Comprendre l'effet des charges mécaniques à haute vitesse sur le matériau est essentiel pour plusieurs applications telles que le formage à haute vitesse, l'usinage ainsi que la résistance aux chocs des structures automobiles et de divers équipements de protection balistique. Pour obtenir un modèle numérique fiable d'un tel processus, une relation constitutive précise décrivant la dépendance entre le taux de déformation du matériau et sa réponse à la traction et compression est nécessaire. Les barres d'Hopkinson (BH) est une méthode couramment utilisée pour déterminer les propriétés du matériau à des taux de déformation élevés allant de $10^2 \mathrm{s}^{-1}$ à $10^4 \mathrm{s}^{-1}$. Les mesures obtenues par cette technique sont utiles pour fournir des données précises pour l'étalonnage des relations constitutives, et pour faciliter la modélisation et la simulation des processus à haute vitesse de déformation.

Dans cette étude, des BH avec une configuration de compression uniaxiale ont été utilisées pour évaluer la courbe de contrainte-déformation à des taux de contrainte spécifiques et des températures variables pour trois alliages, incluant l'aluminium 7050-T7451, l'Inconel 718 et l'acier 300M. Toutefois, le grenaillage induit des taux de déformation allant de 10⁵s⁻¹ to 10⁶s⁻¹, soit 1 à deux ordres de grandeur plus rapide que les barres d'Hopkinson. Afin de simuler des taux de déformation représentatifs de ceux rencontrés lors de l'application du grenaillage, des essais ont été conduits à des températures inférieures à la température ambiante. En effet, la littérature démontre qu'il y a une corrélation entre les effets de la vitesse de chargement et de la température sur l'écrouissage induit par l'essai.

Pour l'aluminium 7050-T7451, les tests à taux de contraintes élevés étaient entre $8\times10^2\text{s}^{-1}$ et $2.8\times10^2\text{s}^{-1}$ à 25°C, et pour des températures allant de -110°C à 200°C à $2.0\times10^3\text{s}^{-1}$. Les résultats de contrainte-déformation pour IN718 ont été obtenus à $2.7\times10^3\text{ s}^{-1}$, $4\times10^3\text{ s}^{-1}$ et 25°C ainsi qu'à des températures de -110°C et 500°C. Pour l'acier 300M, les tests ont été effectués à $2.4\times10^3\text{s}^{-1}$, $3\times10^3\text{s}^{-1}$ et 25°C. De plus, des tests évaluant l'influence de la température, à un taux de contrainte de $2.3\times10^3\text{s}^{-1}$, ont été effectués à -70°C, 200°C et 500°C. En outre, des essais de traction quasi statiques à 10^4 s^{-1} et 25°C ont été utilisés pour évaluer la sensibilité du taux de déformation de chaque alliage.

D'après les tests avec les BH, les résultats pour la courbe de contrainte-déformation de l'aluminium 7050-T7451 ont montré une augmentation de la sensibilité au taux de contraintes supérieur à $10^3 s^{-1}$ à 25° C. Pour des tests de température variés, mesurée à $2x10^3 s^{-1}$, la courbe de contrainte-déformation à -110°C a montré une résistance et un taux de durcissement sous tension initiale élevé par rapport aux résultats obtenus à 25° C. Un taux de durcissement sous tension négatif s'est produit pour les résultats de contrainte-déformation à 100° C et 200° C et le taux de d'adoucissement thermique a augmenté à 200° C.

IN718 a montré une augmentation modérée de sa résistance sous un taux de contrainte de 10^3s^{-1} à $4 \times 10^3 \text{s}^{-1}$ et une température de 25°C . Pour les essais à température variable et un taux de contrainte de $4 \times 10^3 \text{s}^{-1}$, la résistance a augmenté à -110°C par rapport à 25°C et le taux de durcissement sous tension était comparable dans les deux cas. À 500°C , le taux de durcissement sous tension mesuré était nettement inférieur par rapport au résultat à 25°C .

Les alliages d'acier 300M testés à $3x10^3s^{-1}$ et 25°C ont montré une saturation de contraintes et un léger durcissement sous tension négatif pour une tension croissante. Pour une vitesse de déformation de $2.4\times10^3s^{-1}$, la résistance à -70°C était supérieure à celle de 25°C, et les tendances d'écrouissage étaient similaires pour les deux conditions. La courbe de contrainte-déformation à 200°C a montré une augmentation initiale de l'écrouissage avant adoucissement, et une saturation de la contrainte à 500°C était comparable à celle mesurée à 25°C. En outre, une rupture en cisaillement s'est produite dans des échantillons testés à des températures variables et la défaillance due à la contrainte était comparable dans tous les cas.

Les résultats du test avec les BH obtenus à des taux de contrainte élevés, des températures variables et les données quasi statiques ont été utilisés pour adapter le modèle constitutif Johnson Cook (J-C) pour chaque alliage. Un modèle modifié de Johnson Cook incluant la loi de Voce sur le durcissement par tension et le modèle modifié de Khan-Huang-Liang (KHL) était plus représentatif pour l'aluminium 7050-T7451 et IN718 lorsque comparé avec le modèle J-C. Pour l'acier 300M, le modèle J-C modifié avec le modèle Cowper-Symonds pour le taux de déformation a fourni une corrélation relativement plus comparable aux tests par rapport au modèle J-C.

Acknowledgements

This work was made possible by the guidance and support from many individuals to whom I would like to express my sincere gratitude and appreciation. I first thank my project supervisors, Prof. Richard Chromik from McGill and Prof. Martin Levesque from École Polytechnique de Montreal, for providing me with the opportunity to take part in the project, and the support, guidance and advice they provided throughout this work.

At McGill, thanks are given to Huseyin Aydin for providing training on the Split-Hopkinson pressure bar (SHPB) apparatus; Robert Paquette and Monique Reindeau for providing access to laboratories and lending test supplies; and the machine shop staff at Mining and Materials and Mechanical Engineering departments for re-sizing samples and custom fabrications. I would like to thank Prof. John Jonas, Prof. Frank Mucciardi, and Prof. Guillaume Gervais, for the opportunities to discuss materials properties and experimental methods. I also acknowledge and thank my research group for their support, Sara for assistance with the French translation of the abstract, and Barbara Hanley for assistance with administrative tasks.

Special thanks to Mr. Thierry Lafrance and his technical staff from the Meckanic Company. Their work improved the pneumatic capacity, reliability and safety aspects of the SHPB apparatus, which enabled for regular use of the setup. I also extend my appreciation to Benedict Besner and Nour Aimene from École Polytechnique for their technical assistance with the setup and repairs of SHPB instrument.

At École Polytechnique, I acknowledge and thank Amrita Bag for her assistance with heat treatment of 300M steel samples, and Prof. Myriam Brochu for discussions of the process. I also thank Thierry, Charles, and Amrita for providing material specifications, tensile test results, Antonio, Fubin for discussions of SHPB results, and Hongyan Miao for discussions and the organization of project meetings.

Financial assistance and project support from the following sponsors and organizations are gratefully acknowledged: Pratt & Whitney Canada, Héroux Devtek, Bell Helicopter, L3 Communications, Centre Technologique en Aérospatiale, the Consortium for Research and Innovation in Aerospace in Quebec (CRIAQ), and Natural Sciences and Engineering Research Council of Canada (NSERC).

Finally, I would like to thank my parents for their love, support, and encouragement throughout my studies.

Table of Contents

Abstract	i
Résumé	iii
Acknowledgements	v
Table of Contents	vi
List of Figures	ix
List of Tables	
Chapter 1 Introduction	1
1.1 Background	1
1.2 High Strain Rate Material Response	3
1.3 Scope and Objective	
Chapter 2 Literature Review	
2.1. Split Hopkinson Pressure Bar (SHPB) Method	
2.1.1 Overview of SHPB Setup and Operation	
2.1.1.1 SHPB Dynamic Stress and Strain Evaluation	
2.1.2 SHPB Instrument Parameters	
2.1.3 SHPB Compression Pulse Shaping	12
2.1.4 SHPB Modified Temperature Setup	14
2.2 High Strain Rate Stress-Strain Response of Alloys	15
2.2.1 Aluminum 7050-T7451	15
2.2.1.1 High Strain Rate Properties of Aluminum 7050-T7451	16
2.2.2 Inconel 718	18
2.2.2.1 High Strain Rate Properties of IN718	18
2.2.3 300M Steel	20
2.2.3.1 High Strain Rate Properties of 300M Steel	21
2.2.4 Low Temperature Stress-Strain Response	23
2.3 Dynamic Stress-Strain Material Constitutive Models	26
2.3.1 Johnson Cook Model	27
2.3.1.1 Applications of the Johnson Cook Model	28
2.3.2 Modified Johnson Cook Models	
2.3.3 Modified Khan-Huang (KH) Model	33

2.4. Literature Review Summary	34
Chapter 3 Experimental Procedures	35
3.1 Material Specifications	35
3.1.1 Aluminum 7050-T7451	35
3.1.2 Inconel 718	35
3.1.3 300M Steel	36
3.2 SHPB Experiment Summary	37
3.3 Compressive Split-Hopkinson Pressure Bar Setup	38
3.3.1 SHPB Heating and Cooling Setup	41
3.4 Pulse Shaping	43
3.5 Data Processing and Evaluation	44
3.5.1 Average Strain Rate	47
3.5.2 Strain Hardening Rate and Thermal Softening	49
3.6 SHPB Testing Summary	49
3.7 Quasi-Static Tensile Tests	50
3.8 Constitutive Model Fitting	51
5.6 Constitutive Woder I Itting	
	52
Chapter 4 Results and Analysis	52 52
Chapter 4 Results and Analysis	
Chapter 4 Results and Analysis 4.1 Aluminum 7050-T7451 4.1.1 Strain Rate Sensitivity at 25°C.	
Chapter 4 Results and Analysis 4.1 Aluminum 7050-T7451 4.1.1 Strain Rate Sensitivity at 25°C 4.1.2 Temperature Dependence	
Chapter 4 Results and Analysis 4.1 Aluminum 7050-T7451 4.1.1 Strain Rate Sensitivity at 25°C 4.1.2 Temperature Dependence 4.2 Inconel 718	
Chapter 4 Results and Analysis 4.1 Aluminum 7050-T7451 4.1.1 Strain Rate Sensitivity at 25°C 4.1.2 Temperature Dependence 4.2 Inconel 718 4.2.1 Strain Rate Sensitivity at 25°C	
Chapter 4 Results and Analysis	
Chapter 4 Results and Analysis 4.1 Aluminum 7050-T7451 4.1.1 Strain Rate Sensitivity at 25°C 4.1.2 Temperature Dependence 4.2 Inconel 718 4.2.1 Strain Rate Sensitivity at 25°C 4.2.2 Temperature Dependence 4.3 300M Steel 4.3.1 Strain Rate Sensitivity at 25°C 4.3.2 Temperature Dependence Chapter 5 Constitutive Model Evaluation 5.1 AA7050-T7451	
Chapter 4 Results and Analysis 4.1 Aluminum 7050-T7451	

5.2 IN718	
5.2.1 Johnson Cook Model	80
5.2.2 Modified KHL Model	83
5.3 300M Steel	85
5.3.1 Johnson Cook Model	85
5.3.2 Johnson Cook – Cowper Symonds Model	88
5.3.3 Johnson Cook – Voce Strain Hardening Model	89
5.4 Constitutive Model Stress-Strain at 25°C	91
5.4.1 AA7050-T7451	91
5.4.2 IN718	95
5.4.3 300M	97
Chapter 6 Conclusion	101
6.1 Summary	101
6.2 Future Work	104
References	105
Appendix A	115

List of Figures

Figure 1.1. a) The generation of sub-surface compressive strain (εres) and stress (σres) by a shot particle
impact. (σrr) and (σzz) denote the contact stress developed in the radial and perpendicular directions
respectively relative to particle impact. (τmax) indicates the maximum shear stress. b) Plastic stretching
of the surface from multiple impacts (Adapted from [3])
Figure 2.1. Representative schematic of a compressive Split-Hopkinson bar setup [25]7
Figure 2.2. A time-position diagram of transient impact waves [26].
Figure 2.3. Typical measured strain gage signals from a SHPB compression test [24]9
Figure 2.4. Attachment of a thin metal sheet to the incident bar for pulse shaping [45]
Figure 2.5. Application of Ni-Mo pulse shaper in SHPB compression testing of Ni-Ti alloy. a) Loading
wave profiles with different shaper thickness (area = 31.5 mm ²). b) Stress-strain and strain rate-strain
results with a 1.8 mm thick shaper [46].
Figure 2.6. An example of the use of a mechanically actuated specimen holder to move the sample into
furnace for heating and align the sample with SHPB loading bars for impact [56]
Figure 2.7. Stress-strain of AA7050-T7451 at different temperatures (1: 20°C, 2: 100°C, 3: 200°C, 4:
300°C) and varying strain rates. a) 0.001s ⁻¹ . b) 1050s ⁻¹ . c)2350s ⁻¹ . d) 6200s ⁻¹ [63]16
Figure 2.8. Experimental true stress-strain (symbols) at different temperatures and strain rates for
AA7050-T7451: a) 10 ⁻⁴ s ⁻¹ . b) 2500s ⁻¹ . c) 7000s ⁻¹ . Solid lines were constitutive model correlations [67]17
Figure 2.9. The dependence of strain hardening on strain, strain rates at different temperatures for
AA7050-T7451: (a) 25°C. b) 200°C [67]18
Figure 2.10. Precipitation hardened IN718 Hopkinson compression data 25°C. a) True stress-strain data.
b) Stress at 0.1% strain vs. strain rate [69]
Figure 2.11. Hopkinson compression data at 25°C for precipitation hardened and annealed IN718 [49]19
Figure 2.12. Hopkinson compression data for solution and aging treated IN718 at different strain rates and
20°C. [70]
Figure 2.13. a) True stress-strain data at 25°C for AISI 4340 steel alloy. b) Stress vs strain rate at specific
strains [74]
Figure 2.14. True stress-strain of 4340 steel at 25°C and varying striker bar impact velocities of a) 17 m/s
and b) 20 m/s [75]
Figure 2.15. True stress-strain data for 4340 steel at various strain rates and 25°C [76]23
Figure 2.16. True stress-strain data for HSLA-65 steel at various strain rates and temperatures. a) $10^3 s^{-1}$
b) 3000s ⁻¹ (Adapted from [80])
Figure 2.17. Experimental data and Johnson Cook model correlation for AA7050-T7451 from SHB
tensile tests at 25°C [96]
Figure 2.18. Experimental data (solid lines) and Johnson Cook model fitting (dashed lines) for annealed
and precipitation hardened IN718 at 25°C. a) Quasi-static compression results. b) Dynamic compression
results [49]29

Figure 2.19. Flow stress vs strain rate at 5% plastic strain, 25°C and 200°C for Aluminum 2139-T8.
The solid line shows the general trend of strain rate sensitivity at different temperatures [97]30
Figure 2.20. Comparison of experimental data, Johnson Cook and Johnson Cook - Adiabatic heating
models for IN718 subjected to quasi-static and dynamic torsion tests at 25°C [104]32
Figure 2.21. Comparison between experimental data (symbols) and modified KHL model (solid lines) for
Titanium 6-4: a) Strain rate sensitivity at 25°C. b) Effect of strain rate and temperature at dynamic strain
rates [106]
Figure 4.1. Comparison of AA7050-T7451 sample orientations for strain rates of 2000s ⁻¹ and 10 ⁻⁴ s ⁻¹ 53
Figure 4.2. Strain rate sensitivity results of AA7050-T7451 at 25°C. a) True stress vs true strain. b) True
strain vs strain rate. c) Deformed sample from varying strain rate tests
Figure 4.3. Strain rate sensitivity of AA7050-T7451 at 25°C. a) True stress vs strain rate. b) Strain rate
hardening rate at varying strain rates
Figure 4.4. Temperature sensitivity results of AA7050-T7451 at a nominal strain rate of 2000s ⁻¹ . a) True
stress vs true strain. b) Strain rate vs true strain. c) Deformed samples from varying temperature tests 57
Figure 4.5. Temperature sensitivity of AA7050-T7451 at 5, 10 and 15% true strain. a) Thermal softening.
b) Strain hardening rate
Figure 4.6. Dynamic stress-strain and quasi-static tensile results of IN718 at 25°C. a) True stress vs true
strain. b) Dynamic strain rate vs true strain. c) Deformed Hopkinson test samples at varying strain rates.
60
Figure 4.7. Strain rate sensitivity of IN718 at 25°C. a) True stress vs strain rate. b) Strain rate hardening
vs true strain
Figure 4.8. Temperature sensitivity results of IN718 at an average strain rate of 4000s ⁻¹ . a) True stress vs
true strain. b) Strain rate vs true strain. c) Deformed samples from varying temperature tests
Figure 4.9. Temperature sensitivity of IN718 at an approximate average strain rate of 4000s ⁻¹ . a) Thermal
softening. b) Strain hardening
Figure 4.10. 300M steel test results at varying strain rates, 25°C. a) True stress vs true strain. b) True
strain vs strain rate. c) Deformed samples from tests at 25°C
Figure 4.11. Strain rate sensitivity of 300M at 25°C. a) True stress vs true strain. b) Strain rate hardening
vs true strain
Figure 4.12. Temperature sensitivity of 300M at approximately an average strain rate of 2450s ⁻¹ . a) True
stress vs true strain. b) Strain rate vs true strain. c) Deformed samples from varying temperature tests 69
Figure 4.13. Temperature sensitivity of 300M steel at an average strain rate of 2400s ⁻¹ . a) Thermal
softening vs true strain. b) Strain rate hardening vs true strain
Figure 5.1. Comparison of AA7050-T7451 experiment data to Johnson Cook model fitting. a) Including
data at 200°C. b) Excluding data at 200°C
Figure 5.2 Comparison of fitted stress using Johnson Cook – Adiabatic heating model to experiments for
AA7050-T745175
Figure 5.3. Comparison of fitted stress using Johnson Cook – Voce strain hardening model to experiments
for AA7050-T745177
Figure~5.4.~Comparison~of~fitted~stress~using~modified~KHL~model~to~experiments~for~AA7050-T7451.~78
Figure 5.5. Comparison of Johnson Cook model fitted stress to experiment for IN71880

Figure 5.6. Comparison of modified KHL model fitting to experiment for IN71883
Figure 5.7. Comparison of Johnson Cook model fitting to experiments for 300M steel86
Figure 5.8. Comparison of fitted stress using Johnson Cook – Cowper-Symonds model to experiments for
300M steel88
Figure 5.9. Comparison of fitted stress using Johnson Cook - Voce strain hardening model to experiments
for 300M steel89
Figure 5.10. Constitutive model stress-strain extrapolated at varying strain rates and 25°C for Aluminum
7050-T7451. a) Johnson Cook model. b) Johnson Cook—Voce strain hardening model92
Figure 5.11. Measured stress-strain at -110°C and 1950s ⁻¹ compared to the fitted stress at 25°C and94
Figure 5.12. Johnson Cook model stress-strain extrapolated at varying strain rates and 25°C for IN718. 95
Figure 5.13. Modified KHL model stress-strain extrapolations at varying strain rates and 25°C for IN718.
96
Figure 5.14. Measured stress-strain at -110°C and 4130s ⁻¹ compared to the fitted stress at 25°C and a
higher strain rate using the Johnson Cook model for IN718
Figure 5.15. Constitutive model stress-strain extrapolated at varying strain rates and 25°C for 300M Steel.
a) Johnson Cook model. b) J–C – Cowper Symonds model. c) J–C – Voce strain hardening model 98
Figure 5.16. Measured stress-strain at -70°C and 2350s ⁻¹ compared to the fitted stress at 25°C and a
higher strain rate using the J-C Voce strain hardening model for 300M Steel

List of Tables

Table 3.1. Aluminum 7050-T7451 composition based on AMS Specification 4050H	35
Table 3.2. IN718 composition based on AMS Specification 4050H.	36
Table 3.3. 300M Steel composition based on manufacturing specification AMS 6257E.	36
Table 3.4. Summary of AA7050-T7451 experiments for three machined orientations	37
Table 3.5. Inconel 718 and 300M steel experiments summary. L and T are longitudinal and transverse	
machined orientations	37
Table 3.6. Pulse shapers applied for each Hopkinson-bar test sample.	44
Table 4.1. Hopkinson test conditions for AA7050-T7451 at 25°C	52
Table 4.2. Temperature dependent tests of AA7050-T7451 at a target strain rate of 2000s ⁻¹	56
Table 4.3. Dynamic strain rate tests of IN718 at 25°C.	
Table 4.4. Temperature dependent tests of IN718 at a target strain rate of 4000s ⁻¹	62
Table 4.5. Dynamic strain rate tests of 300M steel at 25°C	65
Table 4.6. Temperature dependent tests of 300M steel at a target strain rate of 2400s ⁻¹	68
Table 5.1. Elastic modulus value of AA7050-T7451 at different temperatures [63]	71
Table 5.2. Boundary values for the least squares evaluation of Johnson Cook model correlation to	
AA7050-T7451 experiments.	71
Table 5.3. Closeness-of-fit values for Johnson Cook model correlation to AA7050-T7451 experiments	s. 73
Table 5.4. Closeness-of-fit values for Johnson Cook model correlation to AA7050-T7451 experiments	;
excluding 200°C data	73
Table 5.5. Johnson Cook model parameters obtained and literature values for Aluminum 7050- T7451	74
Table 5.6. Heat capacity of AA7050-T7451 at different temperatures [63]	75
Table 5.7. Boundary value and parameters obtained for Johnson Cook – Adiabatic heating model	
correlation to AA7050-T7451 experiments.	76
Table 5.8. Closeness-of-fit values for Johnson Cook – Adiabatic heating model correlation to AA7050	
T7451 experiments	
Table 5.9. Boundary values and parameters obtained for Johnson Cook - Voce strain hardening model	Į
correlation to AA7050-T7451 experiments.	77
Table 5.10. Closeness-of-fit values for Johnson Cook – Voce strain hardening model correlation to	
AA7050-T7451 experiments.	
Table 5.11. Boundary values and parameters obtained for modified KHL model correlation to AA7050	
T7451 experiments	
Table 5.12. Closeness-of-fit values for modified KHL model correlation to AA7050-T7451 experiment	ıts.
	79
Table 5.13. Summary of mean square error and R ² values for model correlations to AA7050-T7451	
experiments	
Table 5.14. Elastic modulus of IN718 at different temperatures.	80
Table 5.15. Boundary values and parameters obtained for Johnson Cook model correlation to IN718	
experiments	
Table 5.16. Closeness-of-fit values for Johnson Cook model correlation to IN718 experiments	81
Table 5.17. Johnson Cook model parameters obtained and literature values for IN718	82

Table 5.18. Boundary values and parameters obtained for modified KHL model correlation to IN718	
experiments	84
Table 5.19. Closeness-of-fit values for modified KHL model correlation to IN718 experiments	84
Table 5.20. Mean square error and R ² values for model correlations to IN718 experiments	84
Table 5.21. Elastic modulus of 300M steel at various temperatures	85
Table 5.22. Boundary values and parameters obtained for Johnson Cook model correlation to 300M	
experiments	86
Table 5.23. Closeness-of-fit values for Johnson Cook model correlation to 300M experiments	86
Table 5.24. Johnson Cook model parameters obtained and literature values for 300M and 300 Maragin	g
steel	87
Table 5.25. Boundary values and parameters obtained for Johnson Cook – Cowper Symonds model	
correlation to 300M experiments.	88
Table 5.26. Closeness-of-fit values for Johnson Cook – Cowper Symonds model correlations to 300M	
experiments.	89
Table 5.27. Boundary values and parameters obtained for Johnson Cook – Voce strain hardening mode	1
correlations to 300M experiments	90
Table 5.28. Closeness-of-fit values for Johnson Cook – Voce strain hardening model correlations to	
300M experiments.	90
Table 5.29. Summary of mean square error and R ² values for model correlations to 300M experiments.	. 90
Table 5.30. Average measured stress and extrapolated stress at 25°C for AA7050-T7451	93
Table 5.31. Equivalent strain rate of cooling test at 25°C and closeness of fit values for AA7050-T745	
	94
Table 5.32. Average measured stress and extrapolated stress at 25°C for IN718	
Table 5.33. Equivalent strain rate of cooling test at 25°C and closeness-of-fit values for IN718	
Table 5.34. Average measured stress and extrapolated stress at 25°C for 300M Steel	
Table 5.35. Equivalent strain rate of cooling test at 25°C and closeness-of-fit values for 300M Steel	

Chapter 1 Introduction

1.1 Background

The mechanical response of materials subjected to high strain rate loading often differs from that observed at quasi-static conditions. High strain rate loading conditions from $10^2 s^{-1}$ to $10^4 s^{-1}$ and above notably occurs for example in machining, mechanical surface modifications shot peening and laser shock peening of materials, and in the events of ballistics, foreign object or debris impact damage to components and structures. High strain rate characterizations thus have been an important aspect of material research to understand basic microstructural mechanisms, properties such as failure criteria, energy absorption for instance in the selection and design of materials and components. In addition, material tests provide data for developing constitutive models and input values applied in the numerical modelling of material responses in high strain rate applications to reduce experimental cost and complexities.

In shot peening, a widely applied surface modification method to improve the fatigue tolerance of metallic components, a material surface is modified by impacts using streams of small, hard spherical projectiles or "shots", which typically travel in the range of 20 to 100 m/s propelled by compressed air [1, 2]. From an individual particle impact, the material undergoes plastic strain and develops sub-surface compressive stress from the elastic recovery of the strained region as shown in Figure 1.1 a) [3]. Multiple, progressive particle impacts further plastically stretches the surface and modifies the sub-surface stress profile as shown in Figure 1.2 b). The two processes impart beneficial compressive residual stress that impedes crack initiation and propagation, and thereby enhance the fatigue resistance of the component. During shot particle impacts, the plastic strain rates developed in the peened surface for instance can approximately reach between 10^3 s⁻¹ to 10^4 s⁻¹ in aluminum alloys [4], and up to around 6×10^5 s⁻¹ in steel [1, 4]. Thus, in finite element analysis of peening-induced plastic strain response and residual stress for example, an accurate constitutive model capable of describing the relationship between the plastic strain and strain rate is an important input for reliable modelling of the process [5, 6]. Experimental high strain rate tests are applied to evaluate the strain rate dependence of material's mechanical properties, and to validate material constitutive models and parameter values [4, 7].

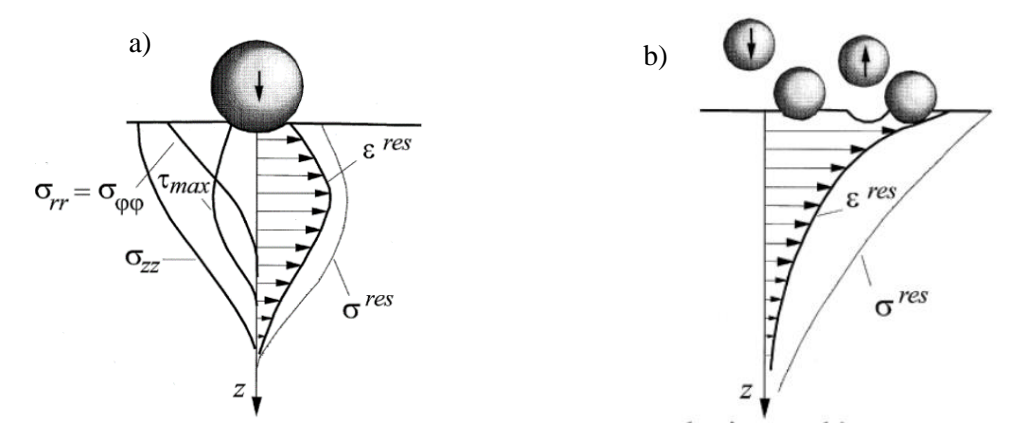


Figure 1.1. a) The generation of sub-surface compressive strain (ε^{res}) and stress (σ^{res}) by a shot particle impact. (σ_{rr}) and (σ_{zz}) denote the contact stress developed in the radial and perpendicular directions respectively relative to particle impact. (τ_{max}) indicates the maximum shear stress. b) Plastic stretching of the surface from multiple impacts (Adapted from [3]).

The three alloys examined in this work are used in the manufacturing of aircraft components which require high tolerance against fatigue. Aluminum 7050-T7451 possess a combination of strength and fracture toughness, and is typically used for thick-section components such as fuselage and bulkheads [8, 9]. IN718 is commonly used for rotating components such as turbine disks in hot sections of the aircraft engine, which requires high thermal-mechanical strength, and low cycle fatigue resistance [10]. 300M steel, typically used for landing gear components, experiences low cycle fatigue over the course of take-off, landing, and high cycle fatigue from ground contact vibrations during taxiing [11]. Shot peening is applied for these materials to further mitigate possible surface-initiated damage arising from defects or discontinuities, including machining and drilling marks [12], microstructural inclusions, and grain boundaries [13], which are detrimental to fatigue resistance in the manufactured components.

1.2 High Strain Rate Material Response

For metallic materials, the rate-dependence of plastic stress at a specific strain, or engineering strain rate sensitivity $(\partial \sigma/\partial \dot{\varepsilon})_{\varepsilon}$ [14] typically display an exponential relation at 25°C such as shown in Figure 1.2. The trend has been attributed to a change in dislocation rate controlling mechanisms that occurs at different regimes of strain rates [15, 16]. Between quasi-static strain rates of 10^{-4} s⁻¹ up to approximately 10^{3} s⁻¹, plastic stress-strain is governed by a thermally activated process [17]. Thermal activation is where thermal vibrations, in addition to external applied stress, assist dislocations in overcoming certain types of microstructural obstacles. With an increase in temperature, dislocation mobility becomes enhanced and the plastic stress decreases. Increasing the strain rate has kinetically the same effect of lowering thermal contributions that lowers mobility of dislocations and increases the strength [18]. The principles of strain rate and temperature reciprocal effects on strength are based upon thermal activation analysis of dislocation motion [14, 19]. At higher strain rates starting generally above 10^{3} s⁻¹, the stress and strain rate sensitivity increases. The traditional hypothesis of strengthening has been the onset of dislocation drag interactions in addition to thermal activation of dislocation slip [17, 18].

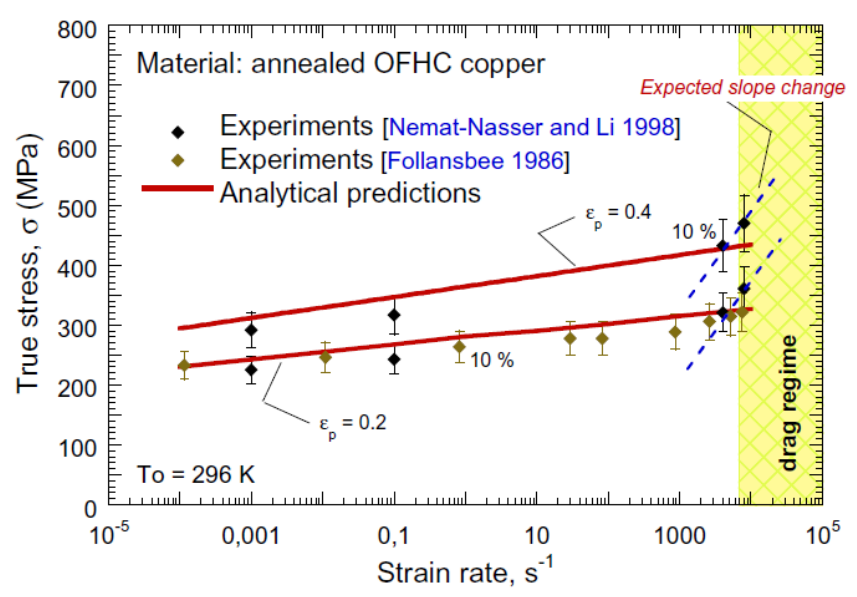


Figure 1.2. Illustration of the strain rate dependence of true stress for annealed OFHC (99% pure) Copper at 25°C [20].

Common mechanical testing methods with corresponding experimental range of strain rates and test conditions are shown in Figure 1.3 [21]. The Split-Hopkinson pressure bar, also known as the Kolsky bar, has been widely used in studying the high strain rate properties of various alloys, ceramics, and composites between rates of 10^2s^{-1} to 10^4s^{-1} . The Split-Hopkinson bar test is an impact based method that involves a projectile bar launched from typically a pneumatic source, and the propagation of elastic waves in solid bars to induce high acceleration and strain rates in the test sample [22, 23]. Within typical strain rate regimes measured by the Hopkinson bar method, experimental considerations including inertial forces due to sample dimensions, and adiabatic heating generated in the sample from high strain rate plastic strain become important, which differentiates high strain rate tests from conventional quasi-static experiments.

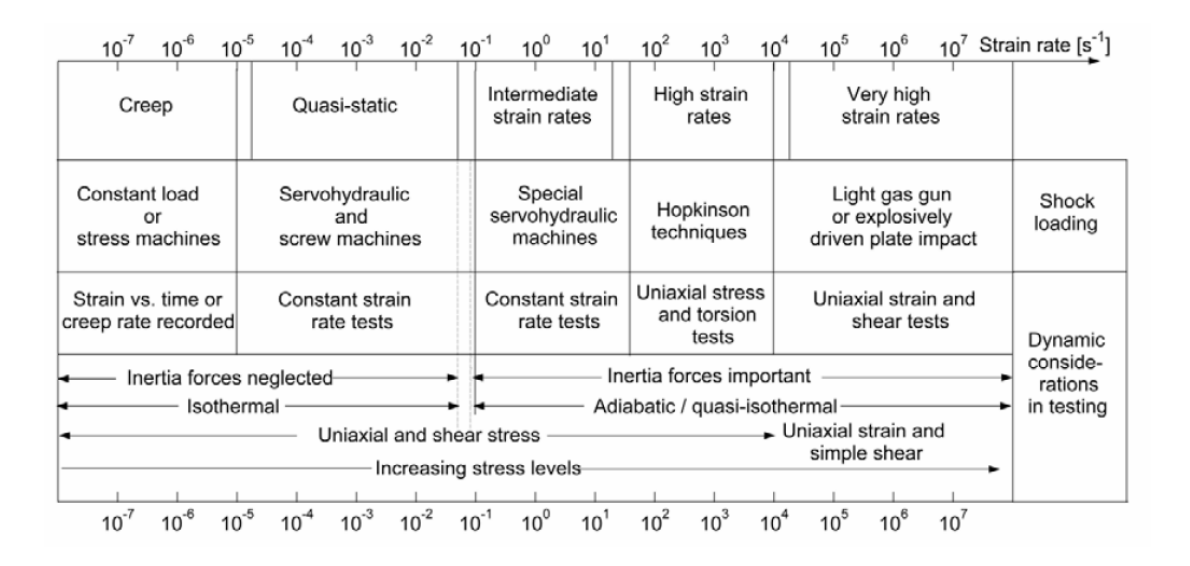


Figure 1.3. Common mechanical materials testing techniques, their corresponding strain rate regimes, and experimental conditions [21].

1.3 Scope and Objective

The thesis aims to evaluate the high strain rate response of Aluminum 7050-T7451, IN718 superalloy, and 300M steel, as well as the calibration of constitutive models to experimental stress-strain results for each material. The high strain rate tests were carried out using a Split-Hopkinson pressure bar (SHPB) compression setup at 25°C and at varying temperatures. In considering the use of the data and model results for shot-peening process simulation, the strain rate, test temperature parameters considered were approximately representative and inclusive of the conditions during shot impacts. A range of strain rate and temperature testing conditions also serves to obtain varying stress-strain response for the evaluation of constitutive model parameters.

Given the highest rate attainable by the Split-Hopkinson bar method is considerably lower than typical rates observed in peening, the measured stress using the Hopkinson setup is expected to be lower than the expected response in peening as alloys in general show an increase in strength with increasing strain rates at 25°C. Hopkinson-bar tests results of alloys at low temperatures and low strain rates have been shown in literature to result in strength equivalent to that attained at higher strain rates at 25°C, such as for Aluminum 7075-T6, IN718, and high-strength low-alloy steel. Therefore, Split-Hopkinson bar tests at sub-room temperatures were applied in this work for each material to examine the extent of increase in strength and to represent the stress-strain response at a higher strain rate and 25°C.

Cooling tests for each alloy involved the lowest test temperature attainable using liquid nitrogen, and the highest target strain rate level below which the sample exhibited stress saturation and shear failure from dynamic compression. The lowest test temperatures used were -110°C for Aluminum 7050-T7451, IN718, and -70°C for 300M steel. The high strain rates tested for Aluminum 7050-T7451, IN718 and 300M steel were at $2x10^3s^{-1}$, $4\times10^3s^{-1}$ and $2.4\times10^3s^{-1}$, respectively. Hopkinson-bar tests at 25° C at the same strain rates as cooling tests were obtained for comparison of strength effect due to cooling. Lower dynamic strain rates and quasi-static tensile results at $10^{-4}s^{-1}$ were used to evaluate the strain rate sensitivity at 25° C.

In addition, Hopkinson-bar compression tests were carried out at high temperatures, and the same strain rate as for cooling and room temperature tests in each alloy. The higher temperatures serve to induce sufficient softening relative to tests at lower temperatures for evaluation of temperature sensitivity in constitutive model fitting. The high temperature limits considered for each alloy were to cover adiabatic heating effects at high strain rates, and to avoid microstructural effects such as recrystallization, phase transformations typically incurred during hot forming conditions.

Empirical based constitutive models, mainly the Johnson Cook, Khan-Huang-Liang equations and their modified forms, were the focus of this work given the relative simplicity of models forms and the ease of evaluation of model parameters. For each alloy, model parameters were obtained using stress-strain results from Split-Hopkinson bar, cooling, room and elevated temperature tests, and quasi-static tests. The constitutive model results were fitted to tests, and predicted stresses were extrapolated to higher strain rates of 10^4s^{-1} to 10^5s^{-1} and 25°C . The overall objective was to use constitutive model stress calibrated from stress-strain results obtained at lower strain rates to illustrate the higher strain rate material response typically observed under shot impact.

This thesis is organized as follows. Chapter 2 presents the literature review of the Split Hopkinson bar testing method, high strain rate material properties, and general effects of low temperatures on strength and application of constitutive material models. Chapter 3 presents a summary of dynamic strain rate experiments, material specifications, and experimental evaluation methodologies. Experimental results obtained from Hopkinson bar testing at varying strain rate and temperatures are presented in Chapter 4. Chapter 5 presents constitutive model fitting to stress-strain results, extrapolations of model stress at higher strain rates, followed by conclusions in Chapter 6.

Chapter 2 Literature Review

2.1. Split Hopkinson Pressure Bar (SHPB) Method

2.1.1 Overview of SHPB Setup and Operation

The Split-Hopkinson pressure bar (SPHB) or Kolsky Bar apparatus has been applied in several uniaxial loading configurations in compression, tension, or torsion for high strain rate tests. A typical SHPB compression setup, as shown in Figure 2.1, consists of two long, cylindrical and symmetrical solid bars, termed respectively the incident and transmitted bars [24]. The bars are usually made of Maraging steel or Inconel [24]. Mechanical supports with bearings provide accurate uniaxial alignment, and enable free axial motion while preventing perpendicular motion to the loading axis. A cylindrical test sample sits sandwiched between the two bars.

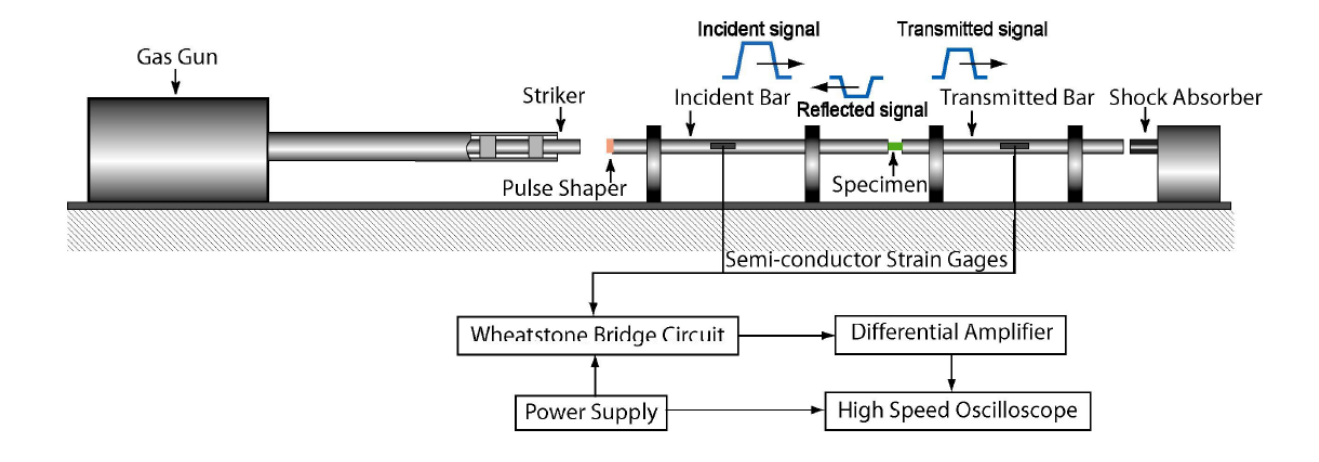


Figure 2.1. Representative schematic of a compressive Split-Hopkinson bar setup [25].

In operation, a projectile called the striker bar is launched from a pneumatic launcher and impacts the free-end of the incident bar at a high velocity. The striker bar is uniaxially aligned by the gas gun sleeve, and generally consists of the same material and cross-sectional area as the loading bars. The striker bar impact sends a compressive stress pulse or incident wave towards the sample, and shifts the loading bars with the sample towards a stop block or absorber. The incident pulse upon reaching the sample becomes partially reflected due to impedance mismatch of the bar-sample interface, and partially transmitted to the output bar [26]. The propagation of waves across the bars and sample illustrated in a time-position diagram is shown in Figure 2.2.

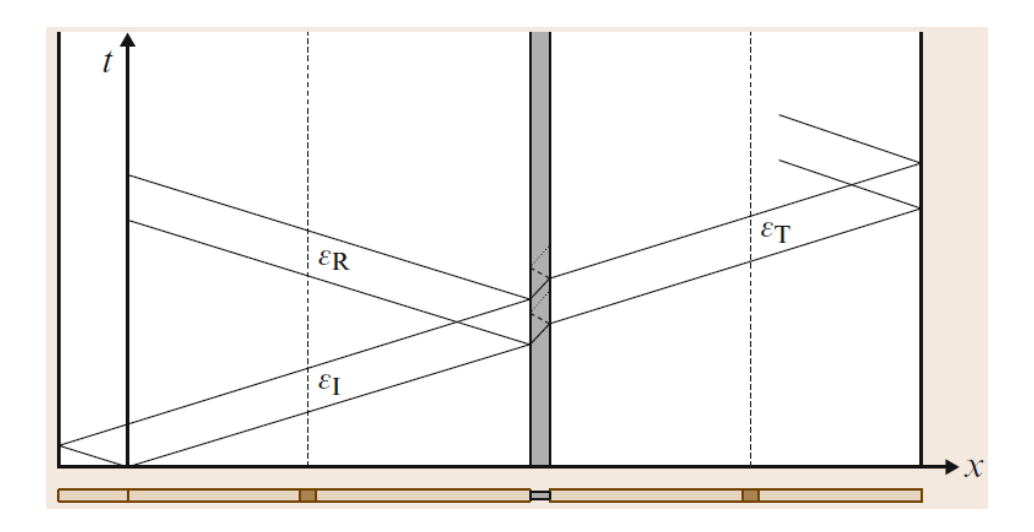


Figure 2.2. A time-position diagram of transient impact waves [26].

Time t = 0 corresponds to the instant of striker bar impact. ($\varepsilon_{\rm I}$) indicates the incident wave from the impact loading, ($\varepsilon_{\rm R}$) and ($\varepsilon_{\rm T}$) denote the reflected and transmitted waves, respectively. During the loading process, wave reflections occurs continuously across the length of the sample due to difference in impedance at both bar-sample interfaces, until the stress buildup is sufficient to cause plastic strain [26]. The elastic strain energy from the incident wave and kinetic energy of the incident bar motion together enable plastic strain of the sample [27].

The amplitudes of the incident wave, reflected and transmitted waves from the superposition of all transmissions at the bar-sample interfaces [28] are measured by foil-type or semi-conductor type gages attached on the surface of each bar. Strain gages are normally located at the mid-point of the bars such that incident and reflected waves do not overlap [24]. The strain gages undergo strain and change in resistance from stress induced by the stress waves. A Wheatstone bridge measures the resistance changes and converts the strain to voltage signals displayed on an oscilloscope. An example of wave signals acquired from a SHPB compression test is shown in Figure 2.3.

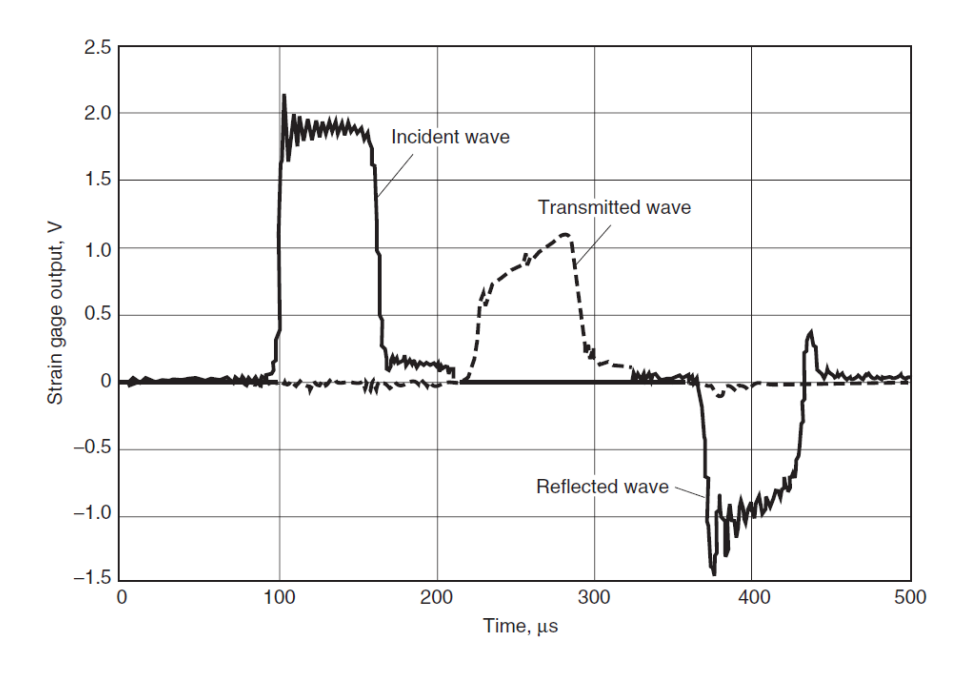


Figure 2.3. Typical measured strain gage signals from a SHPB compression test [24].

2.1.1.1 SHPB Dynamic Stress and Strain Evaluation

The equations for determining the sample stress, strain, and strain rate from the measured waves signals are derived based on the theory of one dimensional elastic wave propagation in a cylindrical solid rod [29]. The engineering stress, presented in equation 2.1, is evaluated using the transmitted strains (ε_t) from the initial transmitted wave. Constants (A_b) and (E_b) are the cross-sectional area and Young's modulus of the bar. (A_o) is the initial sample area. The engineering strain shown in equation 2.2 is evaluated by integrating the measured strains (ε_r) from the reflected wave signal with respective to time. Constant (L_o) denotes the initial sample length and (C_b) is the longitudinal wave velocity in the solid bar. The engineering strain rate, shown in equation 2.3 is the derivative of the strain. The main assumptions of the derivations are that the bars are linear, isotropic and free of wave dispersion effects during loading. Also, the sample is assumed to be in dynamic force equilibrium, with equal force imposed at both barsample interfaces during strain. The derivation has been presented in detail in a few reviews on SHPB principles of operation [24, 28].

$$\sigma(t) = \frac{A_b E \varepsilon_t}{A_o}$$
 (2.1)

$$\varepsilon(t) = \frac{(2C_b)}{L_o} * \int_0^t \varepsilon_r(t) dt$$
 (2.2)

$$\dot{\epsilon(t)} = \frac{2C_b(\epsilon_r)}{L_o} \tag{2.3}$$

2.1.2 SHPB Instrument Parameters

Several aspects must be considered to yield accurate wave signal measurements. First, the incident and transmit bars should possess high aspect ratio of length (L_b) to diameter (D_b) . Typical setups consist of L_b/D_b in the range of 100 to ensure uniform axial stress distribution over the bar cross-sections [24]. For cylindrical test specimens, the sample length (l_s) to diameter aspect ratio (d_s) , l_s/d_s , should be between 0.5 to 1 [28]. The range represents an optimal balance between reducing longitudinal inertia effect by using a shorter sample and reducing radial inertia and interface friction effects, that increase in the case of thin samples [24].

In addition, the sample to bar diameter ratio d_s/D_b must be less than 1 to ensure that the sample does not expand beyond the bar diameter during compression. A d_s/D_b ratio of 0.8 has been suggested to reduce bar-sample interface inertia and friction effects [28]. The use of lubrication at bar and sample interfaces is important to minimize friction [30, 31]. Common lubrications used at room temperatures includes MoS₂, PTFE [32], and boron nitride powder for high temperatures [28]. Similarly, the bar end surface should be checked over period of operation [24, 33]. Bouamoul and Bolduc for example used a coordinate measuring machine (CMM) with accuracy within 9.0 μ m (\pm 4.5 μ m) in the x, y, and z directions for measuring the end-surface roughness of a Maraging steel bar [34]. In addition, Bolduc and Arsenault provided recommendations of surface finish tolerance of RA4 and RA10 for the bars and Aluminum 6061-T6 cylindrical samples respectively examined in the study [33].

A typical impact pulse between two impedance-matched bars has a very brief rise time ($<10~\mu s$) that generates high frequency wave components [35]. Due to Poisson's effect, high frequency wave components propagate with different phase velocities than lower frequency waves, and the input pulse disperses as the wave travels along the bar [28]. The dispersed wave measured by strain gages appears as oscillations, and can mask important details in the evaluated strain and stress. A reduced bar diameter reduces dispersion based on the relation of wave phase velocity to dimension of the bar [28]. Maintaining even height support and bars neutral-axis alignment is also important to avoid excessive sliding friction, minor bending effects which may cause additional wave oscillations [36].

An additional advantage of reduced bars and sample dimensions is reducing the relative error of the stress measurement due to inertial errors and enabling a higher strain rate limited by inertia [26]. The highest strain rate attainable is inversely proportional to the initial sample length (L_0) as,

$$\dot{\varepsilon}_{\text{max}} = \frac{V}{L_0} \tag{2.4}$$

where (V) is the striker bar velocity. A lower dimension limit is defined by 1000 grains or unit cells in any cross-section for the sample to be representative of a bulk sample in terms of mechanical properties [37]. Also, the maximum compressive yield stress of the loading bar (σ_y) limits the striker bar impact velocity as [38],

$$V_{\text{max}} = \frac{2C_0 \sigma_y}{E} \tag{2.5}$$

where (E) is the elastic modulus of the bar. The length of the striker bar (L_s) influences the duration of the loading pulse, and the strain attained in the sample as [24].

$$\varepsilon = 2\dot{\varepsilon} \frac{L_s}{C_o} \tag{2.6}$$

The maximum length of striker bar should be less than half the length of the incident bar such that the incident and reflected signals measured by the incident gage do not overlap [24]. The relationship between the bars, sample geometries and operational factors provide a systematic guideline on experimental design and performance of the Hopkinson compression method.

2.1.3 SHPB Compression Pulse Shaping

The analysis of dynamic stress and strain involve important assumptions of uniform stress and strain rate. The duration of wave buildup to attain stress equilibrium across the length of a sample is termed as the "ring-up" time [39]. For plastically deforming alloys, the ring-up time has been approximated as 3 to 4 times of reverberation across the sample [40, 41]. The finite ring-up time (t) is related to initial sample length (L_s) as [24],

$$t^2 \ge \frac{\pi^2 \rho_s L_s^2}{\partial \sigma / \partial \varepsilon} \tag{2.7}$$

where (ρ_s) is the material density, and $(\partial \sigma / \partial \varepsilon)$ is the strain rate hardening rate. Due to the finite wave propagation time to attain equilibrium and wave dispersion effects, small strains evaluated from measured reflected signals are generally not considered as valid [42, 43]. Thus, the dynamic modulus and yield strength are difficult to measure accurately with the SHPB method. The sample length can be reduced to minimize the time to attain stress equilibrium. Alternatively, the rise time of the incident pulse can be increased to lower the ring up time by pulse shaping [41].

For a compressive SHPB setup, pulse shaping has been accomplished by placing additional component(s), including a dummy sample, an additional bar termed the pre-loading bar [35], or a combination of both between the striker bar and impact-end of the incident bar [22, 35]. The most commonly used pulse shaping component have been thin-sheet materials such as ductile metals, that are initially attached to the impact-end of the incident bar as shown in Figure 2.4. The rise time of the impact wave becomes extended by the elastic and plastic deformation of the thin metal insert [44].

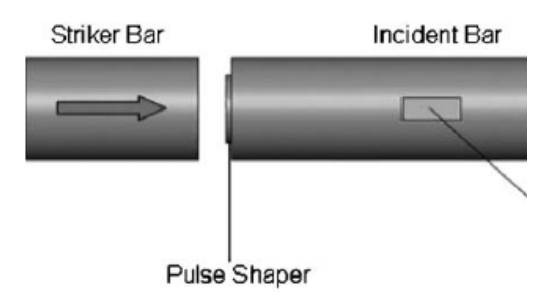


Figure 2.4. Attachment of a thin metal sheet to the incident bar for pulse shaping [45].

Vecchio and Jiang [46] examined a high strength, high strain hardening Ni-Mo alloy as a thin-sheet pulse shaper. The effect of the shaper on impact waves and stress-strain data for a Ni-Ti alloy at 25°C are shown in Figure 2.5. With the use a shaper of sufficient thickness, the incident wave rise time is increased, and peak oscillations in the incident and reflected signals are reduced, as shown in Figure 2.6 a). From the strain rate evaluated in Figure 2.6 b), the profile is steadier when compared to the test without a pulse shaper. The shaper was also shown to be applicable for different samples and test temperatures including single crystal Tungsten, MACOR ceramic at 25°C, and interstitial free steel at -196°C [46].

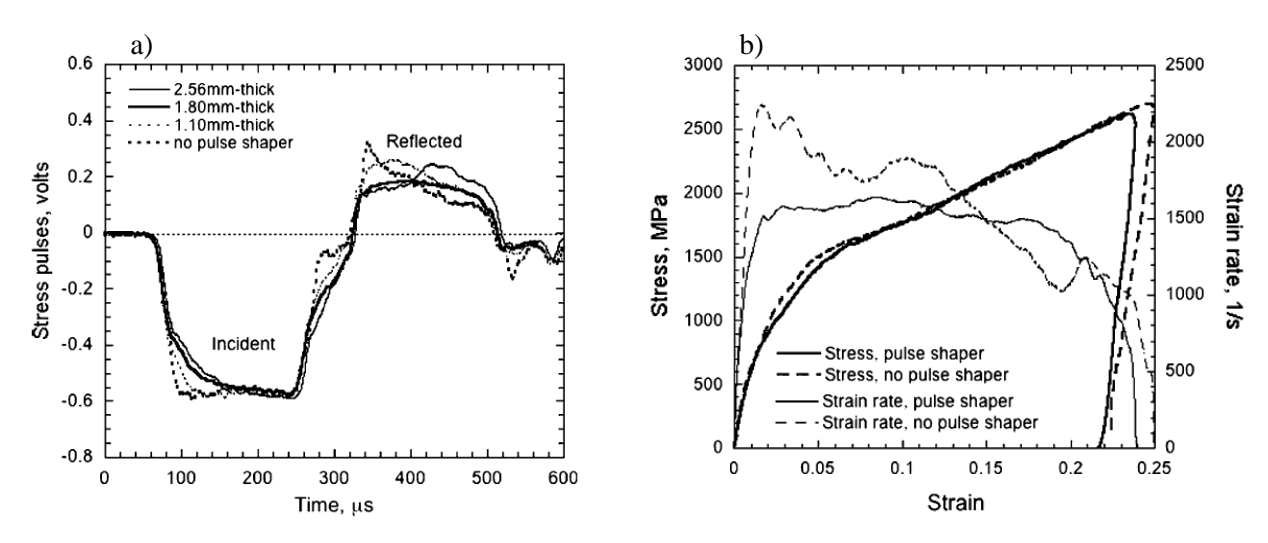
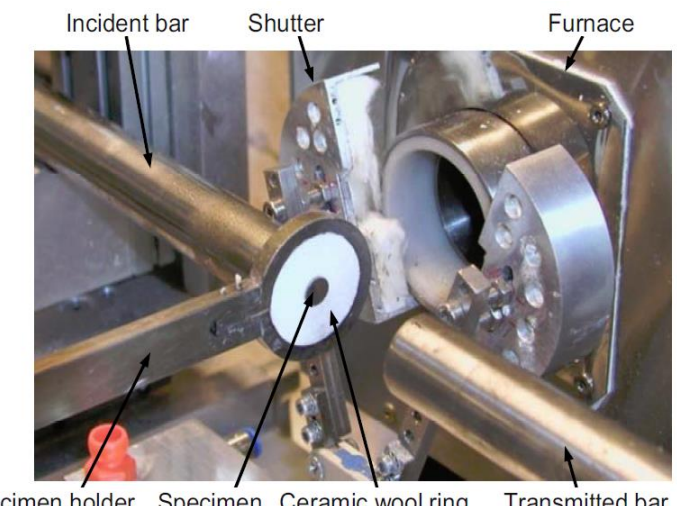


Figure 2.5. Application of Ni-Mo pulse shaper in SHPB compression testing of Ni-Ti alloy. a) Loading wave profiles with different shaper thickness (area = 31.5 mm²). b) Stress-strain and strain rate-strain results with a 1.8 mm thick shaper [46].

In general, ductile metals including aluminum, copper, brass, with thickness ranging between 0.1 to 2 mm, are most commonly used for testing different alloys including 304L steel [47, 48] and IN718 [49]. Copper shapers have also been applied in extending the rise time and the evaluation of stress-strain at low strains in brittle materials such as limestone [50] and Macor glass ceramic [51]. Thus, the use of a shaper may have quite different strength or strain hardening properties as the sample. The selection of a suitable shaper material, dimensions, has been mostly a trial and error process due to differences in geometry of the loading bars and sample properties among specific experiments.

2.1.4 SHPB Modified Temperature Setup

Modifications for heating or cooling the sample can be implemented to carry out high strain rate tests under modified temperatures. Heating methods which have been used include a radiation lamp [52], infrared spot heater [53], and an induction coil [54]. Conventionally, heating is applied to the sample while it is sandwiched between the incident and transmit bars, and both bars become partially heated in the process. A significant temperature gradient can therefore be induced in the bars, particularly if a high testing temperature is required, that modifies the bars elastic modulus. A variation in modulus can result in undesired wave reflections due to changes in acoustic impedance along the bar, that reduces the accuracy of stress-strain measurement [24, 55]. To avoid the thermal contact problem, modifications to the SHPB have been made to separately hold and heat the sample to a specific target temperature for example shown in Figure 2.6 [56]. A synchronized mechanical actuation system aligns the sample with the loading bars after heating and launches the striker bar as soon as the bars close onto the sample.



Specimen holder Specimen Ceramic wool ring Transmitted bar

Figure 2.6. An example of the use of a mechanically actuated specimen holder to move the sample into furnace for heating and align the sample with SHPB loading bars for impact [56].

The setup shown in Figure 2.6 has also been applied for low temperature tests. Instead of a furnace, a mixture of liquid nitrogen and cold nitrogen gas is flown into the chamber to attain a low temperature set point. A simplified cooling setup has also been used, where the sample and loading bars are placed together and cooled in a PTFE column [57]. The change in temperature in most setups is measured using K-type or T-type thermocouple wires for high or low temperature test conditions, respectively. The wires are typically placed in contact with the sample surface [53, 56], or spot welded onto the outer diameter of the sample [58, 59].

2.2 High Strain Rate Stress-Strain Response of Alloys

2.2.1 Aluminum 7050-T7451

Aluminum 7050-T7451 is a heat-treatable alloy with Zn, Mg, Cu, and Zr elements. The T7451 specification indicates an over-aged plate material [60]. The main strengthening mechanism in 7050 Aluminum is derived from precipitates formed from Cu, Zn, Mg elements during solution heat treatment and aging processes [61]. A good balance of high specific strength, fracture toughness and resistance to stress corrosion cracking makes the 7050-T7451 alloy ideal for aircraft bulkhead, fuselage, and wing skin applications [62].

2.2.1.1 High Strain Rate Properties of Aluminum 7050-T7451

High strain rate properties of Aluminum 7050-T7451 have been examined in a few studies with the compressive SHPB method. Figure 2.7 shows stress-strain results presented by Jiang et al. [63] at strain rates of 10^3 s⁻¹ to 6.2×10^3 s⁻¹, and temperatures from 25°C to 300°C. The lack of strain rate sensitivity at 25°C can be explained by the impedance of dislocation motion by precipitates, a long-range type barrier which raises the athermal stress [64]. At elevated temperatures, the strain rate sensitivity becomes more pronounced. At 100° C and between 10^{-3} s⁻¹ to 2×10^3 s⁻¹ for example, the stress and strain hardening increases. Increasing the temperature appears to counteract the athermal stress effect, enabling thermal activation to take greater effect. At the highest strain rate condition in Figure 2.7 d), the stress-strain at all temperatures show a certain degree of strain softening, likely attributed to thermal softening effects [65, 66].

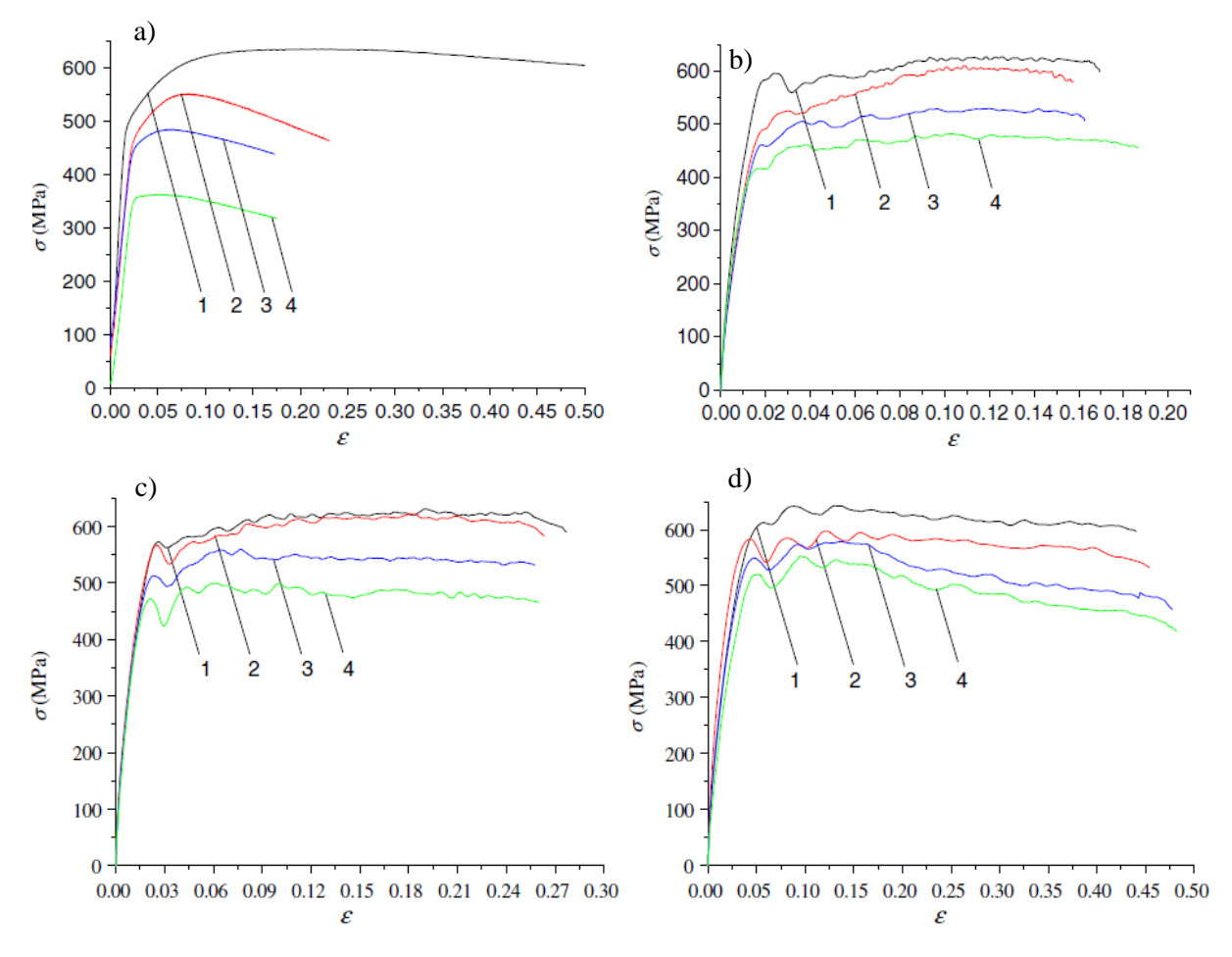


Figure 2.7. Stress-strain of AA7050-T7451 at different temperatures (1: 20°C, 2: 100°C, 3: 200°C, 4: 300°C) and varying strain rates. a) 0.001s⁻¹. b) 1050s⁻¹. c)2350s⁻¹. d) 6200s⁻¹ [63].

Chen at al. [67] have also shown that for AA7050-T7451, strain rate sensitivity at elevated temperatures is greater than that at 25°C as presented in Figure 2.8. The strain rate sensitivity at 25°C is more pronounced in comparison to the results in Figure 2.7. In addition, reported examples of strain hardening dependence as a function of strain rate and temperature are shown in Figure 2.9 [67]. At 25°C and large strains, the strain hardening rate changes from a near-zero value that indicates stress saturation due to dynamic recovery (DRV) to a negative value with increasing strain rates. The negative strain hardening of the stress-strain curve was explained by the onset of dynamic recrystallization (DRX) with grain refinement. As shown in Figure 2.9 b) at 200°C, recrystallization, phase transformation occurs more readily at lower strains, and even at quasi-static strain rates.

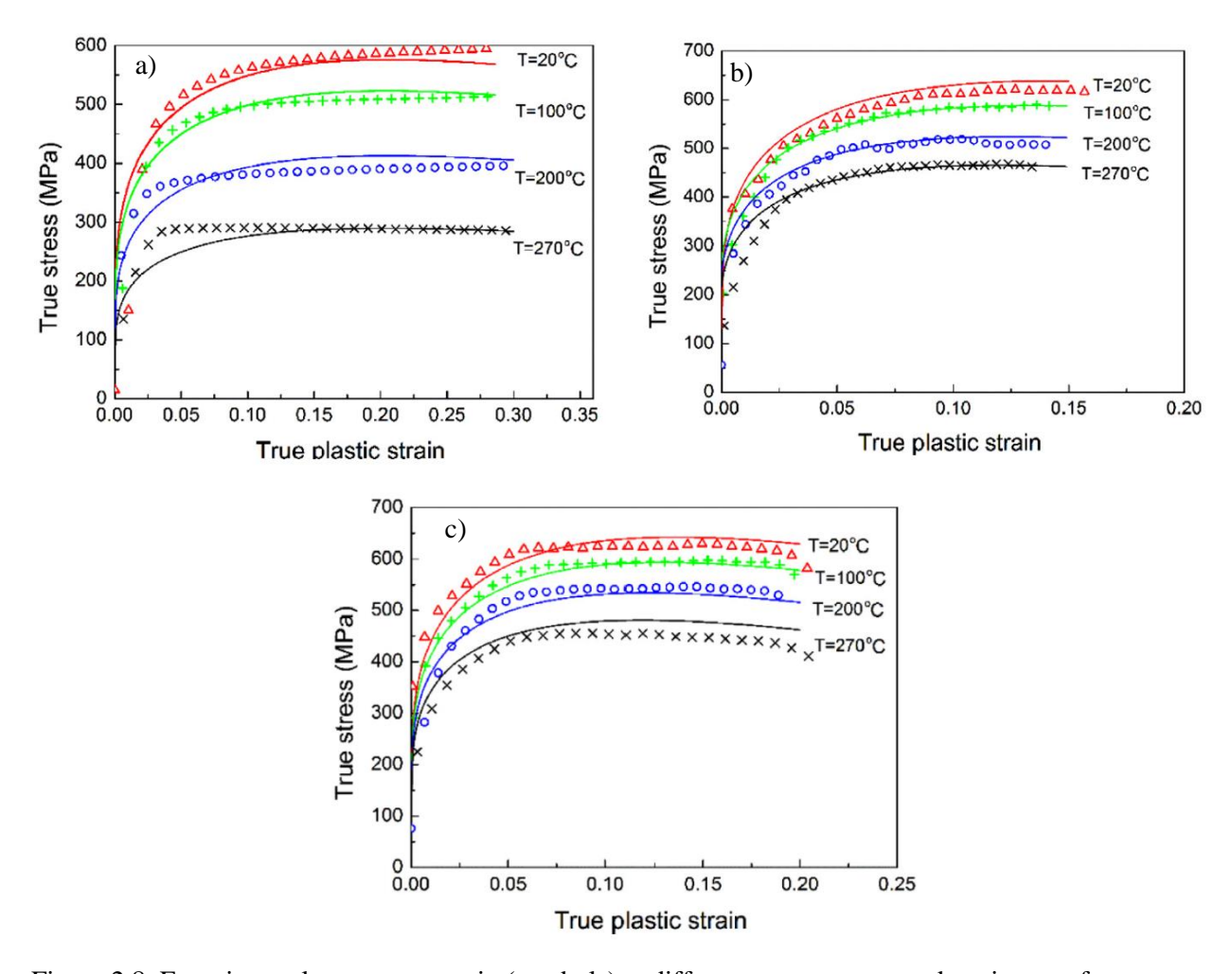


Figure 2.8. Experimental true stress-strain (symbols) at different temperatures and strain rates for AA7050-T7451: a) 10^{-4} s⁻¹. b) 2500s⁻¹. c) 7000s⁻¹. Solid lines were constitutive model correlations [67].

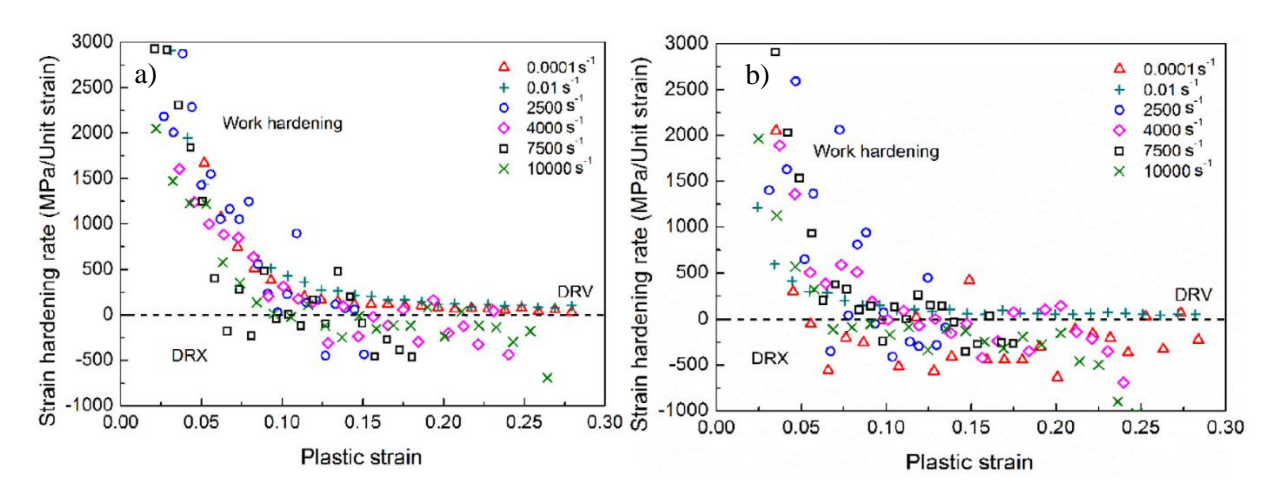


Figure 2.9. The dependence of strain hardening on strain, strain rates at different temperatures for AA7050-T7451: (a) 25°C. b) 200°C [67].

2.2.2 Inconel 718

Inconel 718 is a Ni-Fe alloy characterized by a combination of high temperature strength, oxidation resistance up to 650°C, good creep resistance, and low cycle fatigue strength [49]. IN718 is a commonly applied nickel based alloy for high temperature applications including rotatory turbine disks, engine fan blades, airfoils, and supporting structures in aircraft engines [68]. The strength and high temperature stability of precipitation hardened IN718 is provided by multiple intermetallic phases formed in the nickel, FCC matrix [49]. In the solution treated state, IN718 possesses less precipitation phases, and strengthening is mainly due to solid solution strengthening from elements dissolved in the FCC matrix [49].

2.2.2.1 High Strain Rate Properties of IN718

Dynamic stress-strain results of IN718 obtained by Hopkinson bar compression have been presented in several studies. Experimental data on a precipitation hardened IN718 presented by Liutkus [69], shown in Figure 2.10, display a non-linear increase in stress above 10^3s^{-1} at 0.1 strain and 25°C. In addition, the strain hardening is slightly dependent on the strain rate. As presented in Figure 2.10 a), the slope at 2000s^{-1} becomes progressively lower with strain, whereas the true stress-strain at quasi-static strain rates maintains positive strain hardening over the same interval.

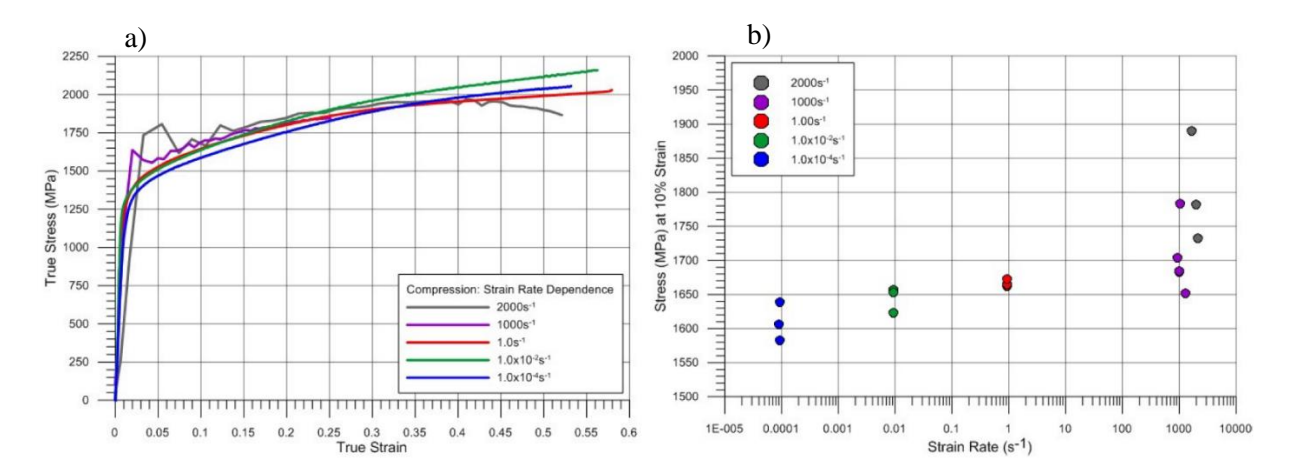


Figure 2.10. Precipitation hardened IN718 Hopkinson compression data 25°C. a) True stress-strain data. b) Stress at 0.1% strain vs. strain rate [69].

A study on precipitation hardened IN718 by Demange et al. [49], shown in Figure 2.11, displays similar strain hardening dependence on strain rate. This effect can be attributed to thermal softening at higher strain rates [49, 69]. Stress saturation occurs more readily in precipitation hardened IN718, which can be attributed to the restriction of dislocation slip in FCC matrix by (γ '') precipitates [49]. The alloy therefore can be susceptible to shear band formation with increasing rate, and shear failure was reported for a test at 4500s⁻¹ and 25°C in the study [49].

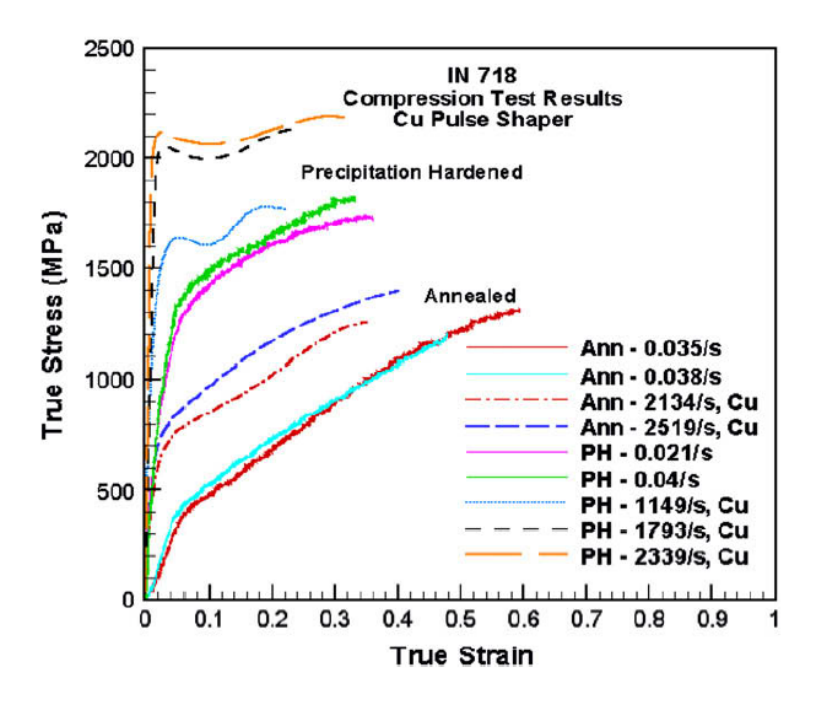


Figure 2.11. Hopkinson compression data at 25°C for precipitation hardened and annealed IN718 [49].

Wang et al. [70] examined a higher range of dynamic strain rates for a solution and aging treated IN718 alloy, as shown in Figure 2.12. At 20° C, a decrease in the stress-strain response occurred between strain rates of $9.1 \times 10^{3} \text{s}^{-1}$ and $1.1 \times 10^{4} \text{s}^{-1}$. From microstructural analysis, the strain softening effect was related to the dispersion of a strengthening phase in the nickel matrix by localized heating effects [70]. In addition, adiabatic heating facilitates dislocation annihilation, which occurs once a peak mobile dislocations density is reached at a specific level of strain rate and plastic strain. Prior to attaining peak dislocation density, strain hardening occurs due to dislocation pile up [70].

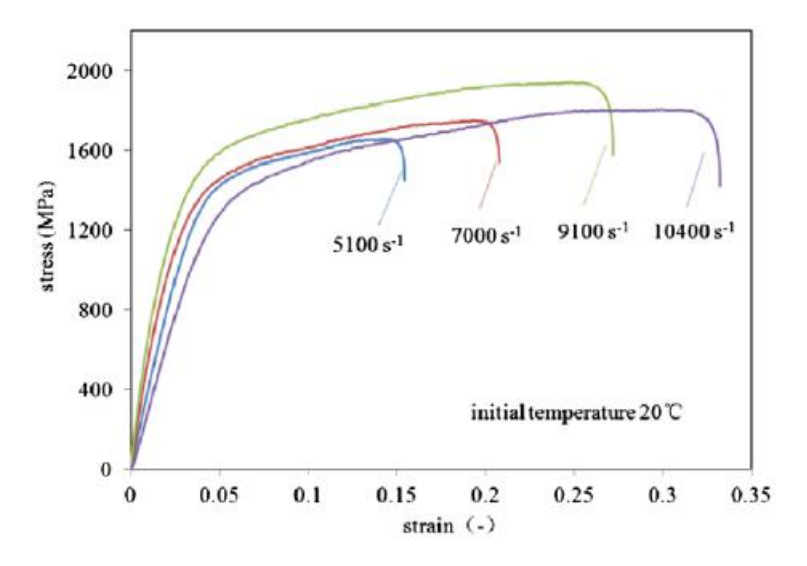


Figure 2.12. Hopkinson compression data for solution and aging treated IN718 at different strain rates and 20°C. [70].

2.2.3 300M Steel

300M steel is a type of ultrahigh-strength steel having a minimum tensile yield of approximately 1400 MPa [71]. 300M is a medium carbon (0.4-0.46 wt%), low-alloy steel with typical compositions of 1.65-2 wt% Ni, 0.7-0.9 wt% Co, and 0.3-0.45 wt% Mo [72]. The high strength and toughness properties of 300M enables its wide application in aircraft landing components, shafts, gears, and fasteners [72, 73].

2.2.3.1 High Strain Rate Properties of 300M Steel

Dynamic stress-strain properties of 300M steel have not yet been extensively examined, although several studies have presented results on 4340 type steel, the basis alloy from which 300M is modified from. True stress-strain results in a study by Lee and Lam [74] on AISI 4340 steel obtained using Hopkinson compression at 25°C, is illustrated in Figure 2.13.

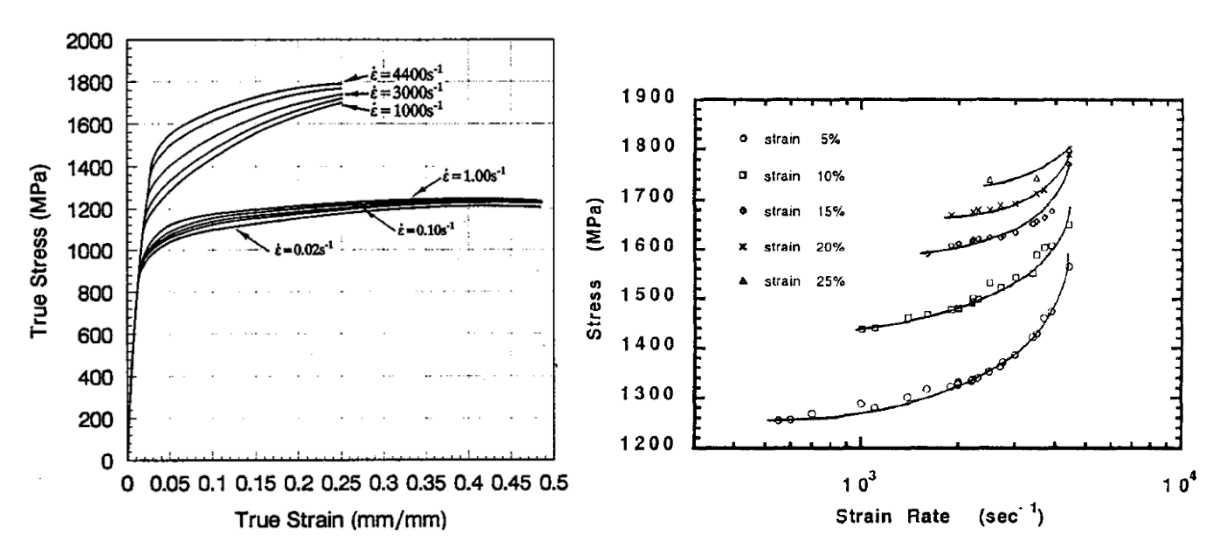


Figure 2.13. a) True stress-strain data at 25°C for AISI 4340 steel alloy. b) Stress vs strain rate at specific strains [74].

At all strain rates, the stress-strain curves maintained a steady, positive strain hardening. Strain hardening increased at dynamic strain rates in comparison to quasi-static compression results. Lee and Lam examined the microstructures of samples deformed under different strain rate conditions. At lower strain rates, the main features observed were dislocation pinning by carbide precipitates and the formation of non-uniform dislocation cells indicative of dislocation cross-slip, promoted by the high stacking fault energy. From 10^3s^{-1} to $4 \times 10^3 \text{s}^{-1}$, an increase in dislocation density, distinctive dislocation loops, and sub-structures with cell walls were observed. The increase in yield stress and strain hardening can be related to a decrease in dislocation cell sizes.

Owolabi et al. [75] focused on the study of shear bands formation in 4340 steel samples subjected to Hopkinson bar compression at 25°C. The true stress-strain results, as shown in Figure 2.14, consist of a high initial strain hardening followed by notable strain softening, and a decrease in strength due to adiabatic shear localization. The striker bar velocity of 17 m/s corresponded approximately to a plastic strain rate of $1670s^{-1}$ (computed from FE simulation). With increasing strain rate, the peak stress increased, and the critical strain to failure occurred earlier. Microscopic analysis revealed cleavage fracture along the shear band zones. The propensity to shear localization could be attributed to carbide particles acting as initial perturbation sites. The strain hardening trend and ductility under compression notably contrasts that in the data of Figure 2.13, where both higher strain and strain rate were reported without notable softening.

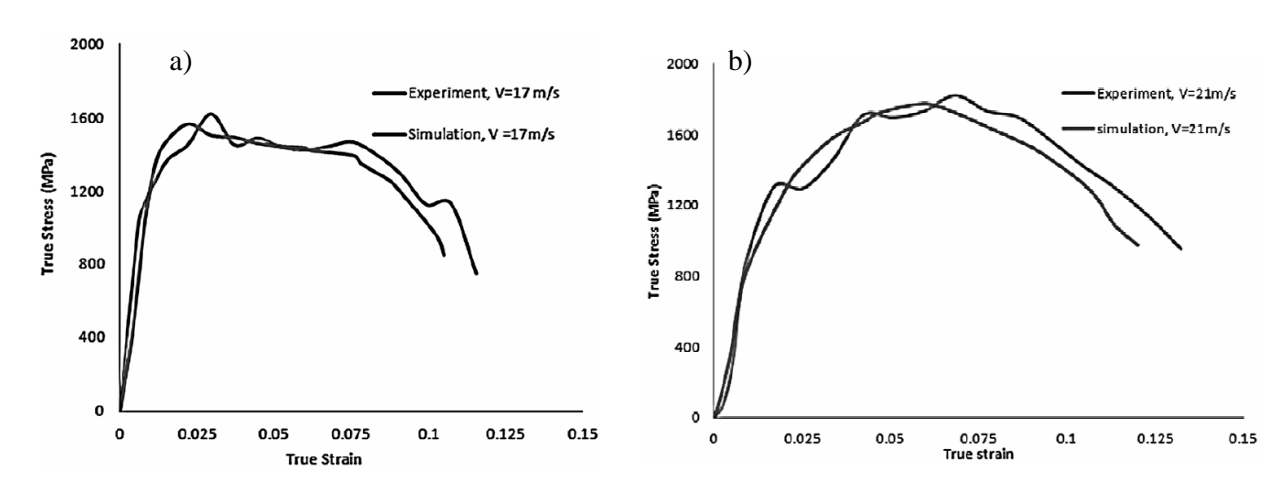


Figure 2.14. True stress-strain of 4340 steel at 25°C and varying striker bar impact velocities of a) 17 m/s and b) 20 m/s [75].

No notable strain softening was observed in results presented by Song et al. [76] on 4340 steel shown in Figure 2.15. Also, the strain hardening at dynamic strain rates do not exhibit a positive increase as the reference in Figure 2.13. The 4340 steel generally displays an enhanced strength starting at a strain rate of $10^3 \mathrm{s}^{-1}$ and $25^{\circ}\mathrm{C}$. The main factors explaining the behaviors from different studies are difficult to ascertain without additional details on material properties, and microstructural analysis available for comparison.

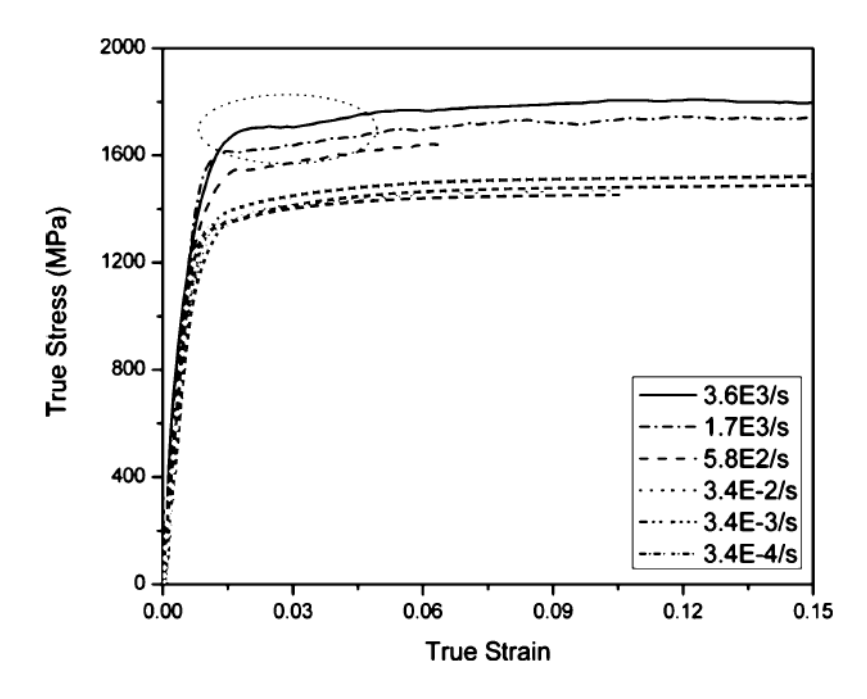


Figure 2.15. True stress-strain data for 4340 steel at various strain rates and 25°C [76].

2.2.4 Low Temperature Stress-Strain Response

Experimental stress-strain response obtained by Hopkinson tests for a 7000 series Aluminum and Inconel 718 alloys under sub-zero temperatures have been shown to exhibit an increase in yield strength and strain hardening compared to 25°C at the same dynamic strain rates. Lee and Lin [77] showed that the strength of Aluminum 7075-T6 increases under sub-room, cryogenic test temperatures due to dislocation multiplication, the effect of which was comparable to an increase in strain rate. From transmission electron microscopy (TEM) micrographs of post-strained samples tested at varying cooling temperatures of -196°C, -100°C, and 0°C, and strain rates of 10³s⁻¹, 5×10³s⁻¹, a decrease in temperature or increase in strain rate shows an increase in the accumulation of dislocations. Similarly, Lee et al. [78] similarly presented Hopkinson compression results for IN718 at -150°C that displayed higher strength relative to that obtained at 25°C and nominal strain rates of 10³s⁻¹ and 5×10³s⁻¹. TEM analysis of the post-strained substructure showed greater planar dislocation arrays, which act as barriers to mobile dislocations, resulting in an increase in strength at higher strain rates and lower temperatures.

The microstructural features which reflect strain rate and temperature effects on strength has been reviewed in general by Gray III [39]. In face-centered cubic (FCC) crystals such as pure Aluminum and Nickel where substructures are mainly formed by dislocation slip, the increase in strain hardening due to high strain rates or lower test temperatures can be related to the suppression of dynamic recovery processes. Dynamic recovery is the reorganization of previously-stored dislocations, a relaxation process that limits dislocation accumulation by annihilation and characterizes the reduction of strain hardening rate with increasing strain [79]. In addition, dynamic recovery in FCC structures involves cross-slip of dislocations, a thermally activated mechanism that is strain rate and temperature dependent [39]. The extent of recovery is reflected by sub-structural features including dislocation distribution, planarity of dislocation debris and local mis-orientation of dislocation structures. Therefore, trends in the dislocation substructure can be indicative of strain rate or temperature effect on kinetics of dynamic recovery, cross-slip activation which affect the measured strength.

The stress-strain response of alloys under quasi-static strain rate and sub-zero temperatures could also attain a level of strength that occurs at 25° C and above 10^{3} s⁻¹. Compressive stress-strain results presented by Nasser et al. [80] for high-strength low-alloy steel (HSLA-65) at varying strain rates and temperatures is shown in Figure 2.16. The peak stress-strain response at 10^{-3} s⁻¹, -60° C in Figure 2.16 a) for example is approximate 800MPa. The magnitude is approximately the same as that at 3×10^{3} s⁻¹, 23° C shown in Figure 2.16 b). The comparison indicates the lower strain rate stress-strain response under sufficiently low temperatures can approximate that of a higher strain rates due to equivalent effects of increasing the strain rate and cooling on strength.

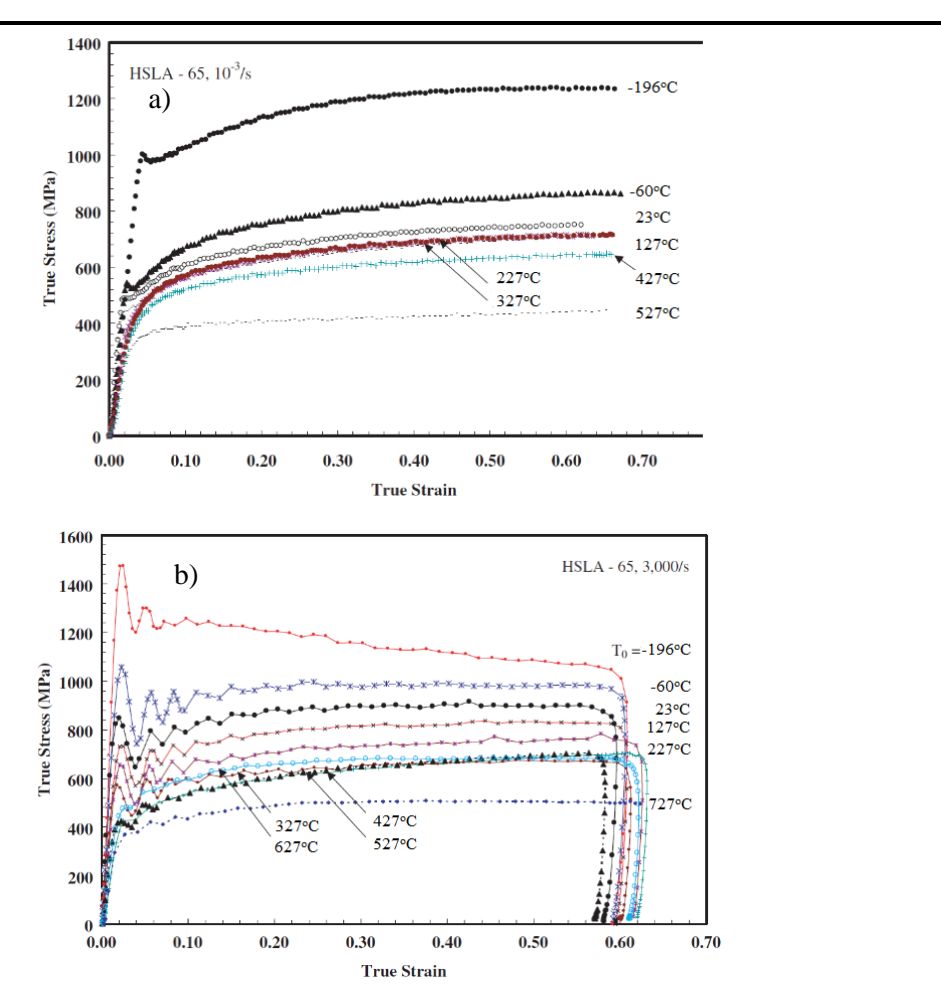


Figure 2.16. True stress-strain data for HSLA-65 steel at various strain rates and temperatures. a) $10^3 s^{-1}$ b) $3000s^{-1}$ (Adapted from [80]).

Meyers et al. [81] presented a modelling approach which applies low strain rates (<10²s⁻¹), sub-zero temperature data to estimate the yield stress at high strain rates up to 10⁵s⁻¹ for 1045 steel at 25°C. Based on the assumption that thermal activation is the main rate-controlling mechanism, the predicted flow stress at 1% strain were close to measured values at 25°C up to 10^4 s⁻¹ using the Hopkinson bar method and 10^5 s⁻¹ from flyer plate impact tests. The results show the yield stress at high strain rates and 25°C maybe describable using parameters evaluated at low temperature, lower strain rates, based on thermal activation analysis. The model correlation, however, was for only the 1% yield stress and excludes strain hardening at large strains which require constitutive relations relating the plastic stress to strain.

2.3 Dynamic Stress-Strain Material Constitutive Models

The plastic stress-strain behavior of metals and alloys, as discussed above, often display a strain rate and temperature dependence as evidenced by changes in yield stress, strain hardening, and onset of thermal softening effects due to adiabatic heating, microstructural recovery and transformations. Plasticity mechanisms also depend on the microstructural lattice structure, grain orientation and texture, alloying and phases, which opposes dislocation motion. Constitutive models aim to correlate to experimental stress-strain data, typically obtained under relatively controlled conditions [82], and to predict material behavior in specific applications where conditions are often comparatively complex [83]. Accurate, reliable models are important as they provide a basis for analytical and finite element modeling simulations employed to aid in material or process design, and to reduce experimental work and costs [82]. The relative ease of evaluating the model, the number and type of experiment involved, and implementation to computational tools therefore also determines the viability of a model [83].

Zerilli and Armstrong proposed physical based constitutive models of different forms for FCC and BCC lattice structures, in terms of their differences in dislocation-rate controlling mechanisms and strain hardening characteristics [84]. Based on short-range and long-range barriers on dislocation kinetics, models by Nemat Nasser and Li [85], Rusinek et al. [86], express the flow stress as a sum of a thermally activated, rate sensitive component, and an athermal stress part that depend only on strain hardening or accumulated dislocations. In another type of physical model called the internal state variable method, the Mechanical Threshold Stress model represents an internal state variable approach that considers changes in microstructure such as evolution of strain hardening rate [86]. A separate group of models, such as Preston-Wallace-Tonks, Steinberg-Gunan, are specifically intended for very high strain rates above 10⁴s⁻¹, due to the difference in stress state, dislocation mechanisms and strain hardening responses when compared to lower strain rates [87, 88].

Empirical models are formulated directly from experimental stress-strain trends [89], and model formulations do not involve mechanism based derivations [83]. In comparison to physical models, empirical models are generally limited to correlating to stress-strain conditions used in

determining the constants, and are less accurate in predictions outside the calibrated range of conditions due to lack of physical basis [90]. However, they have simpler forms, enabling for relatively straightforward evaluation, implementation, and are thus widely applied [89]. Commonly applied Johnson Cook and Cowper Symonds models for instance feature multiplicative, uncoupled strain hardening, rate and temperature effect terms, and relatively few material constants to be evaluated. An empirical model may be more suitable in general simulation of specific material or process, provided that the main effects of strain hardening, strain rate, and temperature can be captured [91]. The review focuses on commonly applied empirical models and their applications to experimental data within conventional strain rates typically obtained using the Hopkinson bar method.

2.3.1 Johnson Cook Model

The empirical model proposed by Johnson and Cook [92] expresses the stress as the product of plastic strain, strain rate, and temperature factors taken independently as,

$$\sigma = [A + B\epsilon_p^n] [1 + C \ln \left(\frac{\dot{\epsilon}}{\dot{\epsilon}_{ref}}\right)] [1 - \left(\frac{T - T_r}{T_m - T_r}\right)^m]$$
(2.8)

where (A) and (n) represent the yield strength and work hardening constants under quasi-static conditions. The strain rate is linear in the logarithm function of the strian rate, $\dot{\varepsilon}/\dot{\varepsilon}_{ref}$, where the variable (ε) is the experimental strain rate and $(\dot{\varepsilon}_{ref})$ is the reference strain rate typically defined at a quasi-static condition. Symbol (T) is experimentally measured temperature, and the melting temperature of the test material is (T_m) . The reference temperature, (T_r) , is typically defined as 25° C or the lowest temperature of the test conditions [93, 94]. The temperature ratio is defined as the homologous temperature (T^*) . Parameters (C) and (m) represent the strain rate sensitivity and thermal softening parameters, respectively. Given the thermal softening exponent (m) is a positive constant, test temperatures should be greater than or equal to the reference temperature for (T^*) to be numerically valid at all conditions. The multiplicative factors mean the model assumes work hardening, strain rate, and temperature effects as separate phenomena, and

parameters of each factor can be evaluated in separate steps. The model is relatively straightforward to interpret and evaluate with a limited number of experiments [95].

2.3.1.1 Applications of the Johnson Cook Model

Tan et al. [96] presented a Johnson Cook model fitting to Hopkinson bar, dynamic tensile test results at 25°C for Aluminum 7050-T7451 alloy as shown in Figure 2.17. The fitted stress does not adequately correlate to the experiment for two strain rates. This can be explained by variations in the strain hardening coefficient (C) as a function of the strain rate were not accounted for [96]. The variations of parameter (C) with strain was shown by solving for the Johnson Cook model with strain rate sensitivity data. A modification was proposed where the strain hardening rate coefficient was defined as a polynomial function of strain and strain rate. The modified model provided better correlations, although the total number of parameters to be solved were nine instead of five in the Johnson Cook model.

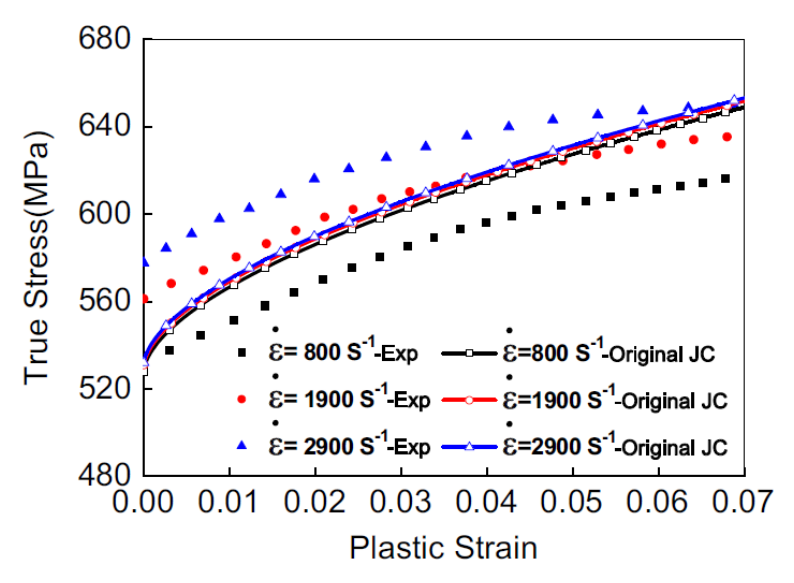


Figure 2.17. Experimental data and Johnson Cook model correlation for AA7050-T7451 from SHB tensile tests at 25°C [96].

Demanage et al. [49] applied the Johnson Cook model to quasi-static, Hopkinson compression results at 25°C for precipitation hardened and annealed IN718 samples. As shown in Figure 2.18, the strain hardening rate for the annealed sample does not vary significantly under high strain rate conditions, and the Johnson Cook model represented the data well. For the precipitation hardened sample, however, the strain hardening decreases and the plastic stress saturates with

strain under dynamic compression. Therefore, the model matches the quasi-static result, but overestimates the dynamic results with the same parameters. The result also represents a shortcoming of the Johnson Cook model due to uncoupled strain hardening and strain rate effects.

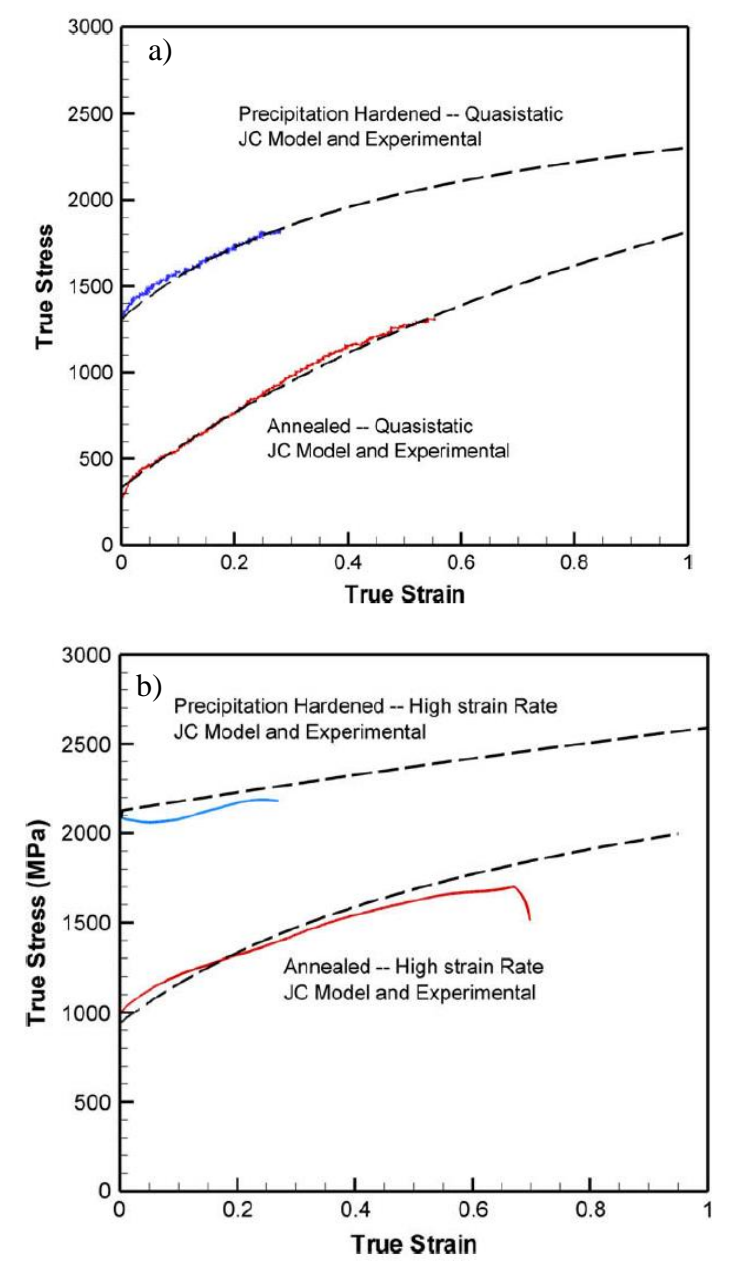


Figure 2.18. Experimental data (solid lines) and Johnson Cook model fitting (dashed lines) for annealed and precipitation hardened IN718 at 25°C. a) Quasi-static compression results. b) Dynamic compression results [49].

In application of Johnson Cook model to variable temperature tests, the uncoupled terms between strain hardening, strain rate sensitivity and temperature can also lead to inaccurate correlations under certain conditions. Vural and Caro [97] presented strain rate sensitivity of flow stress at 5% strain for Aluminum 2139-T8 alloy shown in Figure 2.19. The change in flow stress with strain rate is notably greater at 200°C in comparison to that observed at 25°C, which represents a dependence of rate sensitivity on the temperature. In this case, the Johnson Cook model predicts a limited strain rate dependency at elevated temperatures due to the uncoupled strain hardening and temperature terms.

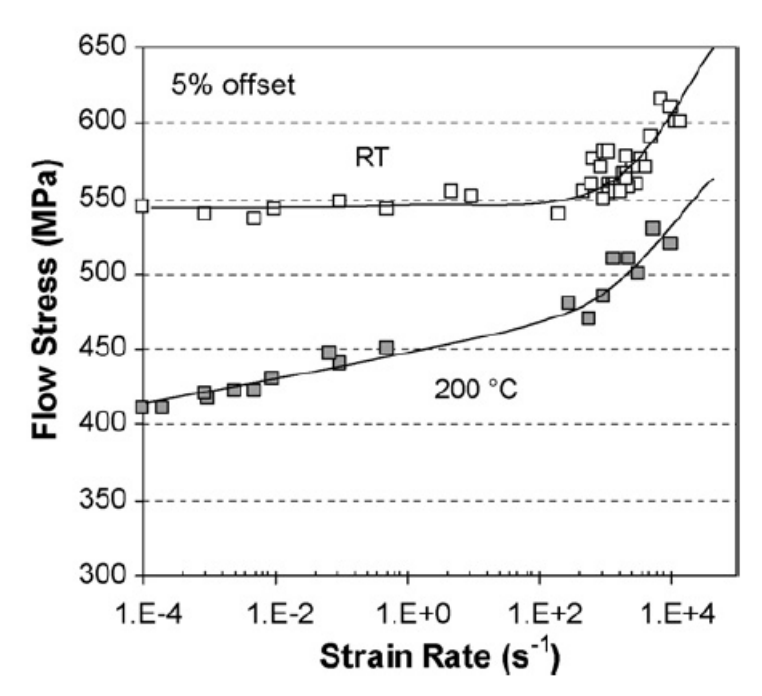


Figure 2.19. Flow stress vs strain rate at 5% plastic strain, 25°C and 200°C for Aluminum 2139-T8. The solid line shows the general trend of strain rate sensitivity at different temperatures [97].

Despite the shortcoming in accounting for interdependent effects of strain hardening, strain rate and temperature in the examples shown, the Johnson Cook model nonetheless has been broadly used for high strain rate applications given its simple form and availability of existing material parameters for comparison. The model has also been the subject of several modifications.

2.3.2 Modified Johnson Cook Models

In the Johnson Cook model, the strain rate in the linear logarithm form predicts a linear increase in stress, which underestimates the non-linear increase in stress often observed in alloys above 10^3s^{-1} . Johnson Cook models with modified strain rate forms have been proposed to account for such strengthening trend for example shown for mild steel [98] and 4340 steel [88]. A modification based on the Cowper Symonds model has been presented [99, 100] for example as,

$$\sigma = \left[A + B\varepsilon_p^n\right] \left[1 + \ln\left(\frac{\dot{\varepsilon}}{D}\right)^{\frac{1}{p}}\right] \left[1 - \left(\frac{T - T_r}{T_m - T_r}\right)^m\right]$$
(2.9)

where the strain rate ($\dot{\varepsilon}$) is the experimentally measured value, and parameters (D) and (p) are strain rate factor constants. Shin and Kim [101] proposed a modified model consisting of a logarithm and an exponential of strain rate terms as:

$$\sigma = [A + B(1 - \exp(-C\epsilon))] \left[D \times \ln\left(\frac{\dot{\epsilon}}{\dot{\epsilon}_{ref}}\right) + \exp(E \times \frac{\dot{\epsilon}}{\dot{\epsilon}_{ref}})\right] \left[1 - \frac{T - T_r}{T_m - T_r}\right]^m \quad (2.10)$$

The inclusion of the exponential strain rate term, where parameter (E) is a constant, aim to account for an exponential rise of stress with the logarithm of strain rate. A Voce strain hardening form was applied that accounts for stress saturation [101]. The temperature is term is also modified with the thermal softening term (m) applied to the entire bracket $[1-T^*]$, instead of only for the homologous temperature (T^*) , which removes the limitation of having the test temperature to be greater than the reference temperature when (T_r) is 25°C.

Important aspects of high strain rate plastic stress are recovery and strain softening due to adiabatic heating. Adiabatic heating condition arises in high strain rate tests due to less time available for temperature to equilibrate during sample deformation [18]. A relatively simple modification to the Johnson Cook model incorporates a temperature rise value (ΔT) from the rate of heat to work conversion as [102].

$$\sigma = [A + B\epsilon_p^n] [1 + C \ln \left(\frac{\dot{\epsilon}}{\dot{\epsilon}_{ref}}\right)] [1 - \left(\frac{T + \Delta T - T_r}{T_m - T_r}\right)^m]$$

$$\Delta T = \frac{\beta}{\rho C_p} \int_0^{\epsilon_f} \sigma d\epsilon$$
(2.11)

Heat generation accounts for most of the mechanical work expended in plastic deformation, with a relatively low fraction portion of energy stored as change in microstructure of the structure. The factor (β) is the fraction of rate of plastic work converted to heat, typically estimated as a constant of 0.9 [103]. Constants (ρ) and (C_p) are the density and temperature-dependent heat capacity of the sample. Kobayashi et al. [104] showed a correlation of equation 2.11 for IN718 results from torsional Hopkins bar tests as presented in Figure 2.20, where the stress-strain exhibited thermal softening and shear localization at 3500s⁻¹.

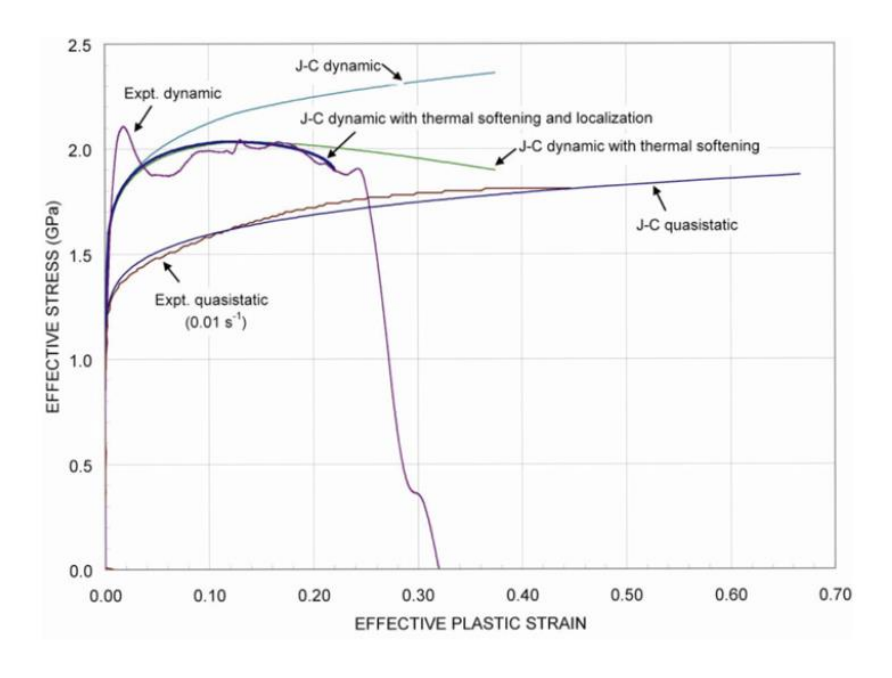


Figure 2.20. Comparison of experimental data, Johnson Cook and Johnson Cook - Adiabatic heating models for IN718 subjected to quasi-static and dynamic torsion tests at 25°C [104].

2.3.3 Modified Khan-Huang (KH) Model

The viscoplastic modified KH model was introduced for correlating to rate sensitivity response of Aluminum 1100 up to 10⁴s⁻¹ [105]. Khan et al. [106] presented a modified KHL model as expressed as,

$$\sigma = \left[A + B\left(1 - \frac{\ln \dot{\epsilon}}{\ln D_o^P}\right)^{n_1} \epsilon^{n_o}\right] \left(\frac{\dot{\epsilon}}{\dot{\epsilon}_{ref}}\right)^C \left(\frac{T_m - T}{T_m - T_r}\right)^m \tag{2.12}$$

Strain hardening parameter (B) is a function of the strain rate. Parameter (D_0^P) is defined as a constant set to $10^6 {\rm s}^{-1}$ that represents an upper strain rate limit. Exponents (n_1) and (n_0) are model constants. The coupling terms in the initial bracket accounts for a decrease in strain hardening with an increase in strain rate. Also, the temperature consists of a change in the numerator of the temperature factor to ($T_m - T$) instead of ($T - T_r$) as in the Johnson Cook model. The definition allows the model to be defined for test temperatures less than the reference of 25°C. The model well represented Titanium 6-4 alloy data for several strain rates and temperatures conditions as shown in Figure 2.21.

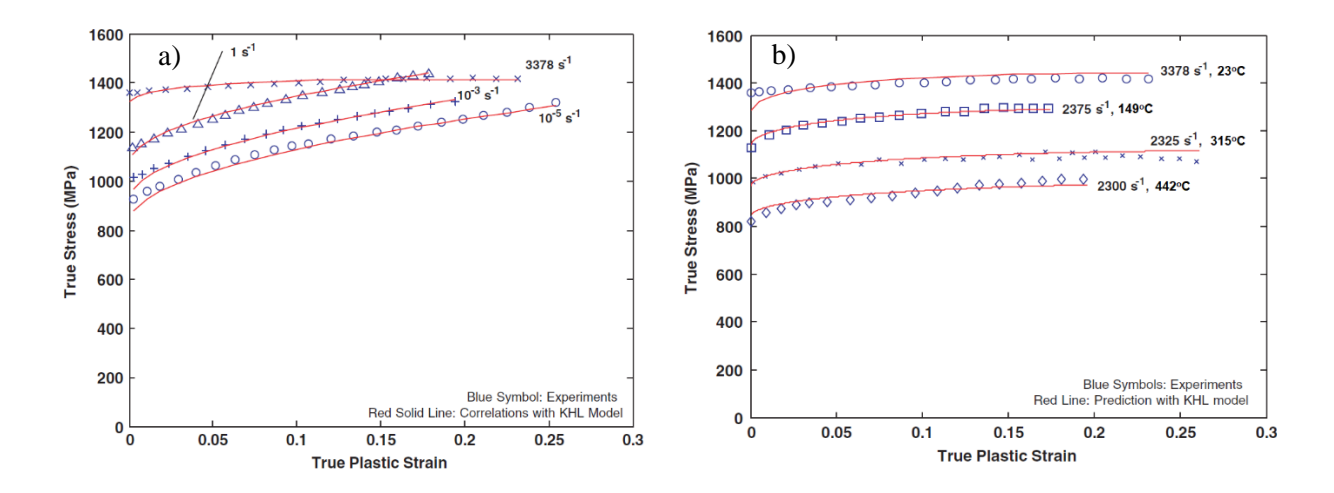


Figure 2.21. Comparison between experimental data (symbols) and modified KHL model (solid lines) for Titanium 6-4: a) Strain rate sensitivity at 25°C. b) Effect of strain rate and temperature at dynamic strain rates [106].

2.4. Literature Review Summary

The Split Hopkinson bar method that provides intermediate to high strain rates in the range of $10^2 s^{-1}$ to $10^4 s^{-1}$, consist of several important setup features including bar material, length, and diameter, allocation of strain gages, which influences wave propagation properties, maximum stress and strain attainable for a specific sample dimension, and proper measurement of transient waves used for stress-strain evaluation. A proper sample dimension is also critical in controlling the magnitude and validity of dynamic stress-strain measured. The use of lubricant is important to minimize excessive interface friction and pulse shapers serve to remove dispersion noise in the signals for accurate representation and evaluation of data.

The stress-strain response of AA7050-T7451, IN718, and 4340 steel alloy reviewed as a comparison to 300M, generally display an enhanced strain rate sensitivity above a transition strain rate around 10³s⁻¹. The stress saturates above a critical strain rate, due to adiabatic heating, and shear localization, marked by strain softening and a decrease in strength. The peak stress at a higher strain rate may consequently drop below that of the lower rate at some intervals of strain. In addition, at high strain rates and elevated temperatures, the strength decreases, and AA7050-T7451 and IN718 alloys can exhibit negative strain hardening due to dynamic recrystallization and dissolution of second phase particles. With lower temperatures, the measured strength could increase analogous the effect of an increase in strain rate given the reciprocal effect of strain rate, temperature on dislocation mobility, and strain hardening.

The different modified Johnson Cook and KHL models provide specific improvements, when compared to the Johnson Cook model such as enhanced strain rate sensitivity at 25°C, as well as coupling thermal softening with increasing strain and strain rates. As empirical models are developed from experimental observations, comparability of model parameters is dependent on the material properties. The calibration data depends the type of loading mode applied, and the range of strain rates and temperatures. Different parameters are therefore commonly found in literature for the same material. A detailed experimental plan suited to the purpose of the application is important for representation of the material response using constitutive models.

Chapter 3 Experimental Procedures

The dynamic stress-strain response for Aluminum 7050-T7451, IN718, and 300M Steel alloys were made across a range of strain rates and temperatures using a compressive Split-Hopkinson pressure bar. The specifications of the test samples, summary of experiments completed, and the Hopkinson-bar instrument and test procedures applied at McGill are described. Following, the data analysis procedures for evaluating the stress-strain and strain rate from Split-Hopkinson bar test data are presented. In addition, a summary of the method used to fit constitutive models to experimental stress-strain data is described.

3.1 Material Specifications

3.1.1 Aluminum 7050-T7451

Aluminum alloy (AA) 7050-T7451 samples provided by L3 Communication MAS were fabricated from a rolled plate by wire electro-discharge machining (WEDM). The chemical composition of AA7050-T7451 is presented in Table 3.1. The material was provided in three machined orientations, namely transverse, longitudinal, and short transverse. The dimensions specified were 6.4 mm in length and 6.09 mm in diameter. Machining tolerances were \pm 0.25 mm for length and diameter. Perpendicularity and parallelism between two cylindrical faces was specified as 0.003 TIR. Surface finishing specified was 32 μ -inch or better without polishing.

Element Zn Cu Mg Zr Si Fe Mn Τi Cr Min (%) 5.7 2.0 1.9 Max (%) 6.7 2.6 2.6 0.010 0.12 0.15 0.10 0.06 0.04

Table 3.1. Aluminum 7050-T7451 composition based on AMS Specification 4050H.

3.1.2 Inconel 718

IN718 cylindrical samples supplied by Pratt and Whitney Canada were fabricated with WEDM in longitudinal and transverse directions from a cylindrical bar. The chemical composition of the material is presented in Table 3.2. The IN718 alloy supplied for this work consists of a Vickers hardness of 44 HRC.

Table 3.2. IN718 composition based on AMS Specification 4050H.									
Element	Ni	Cr	Nb	Ti	Mo	Al	Co	Fe	
Min (wt%)	50	17	4.75	0.65	2.8	0.2			
								Remainder	
Max (wt%)	55	21	5.50	1.15	3.3	0.8	1	Remainder	
,									

The dimensions of as-provided Hopkinson sample were 10 mm in length (L_0) and 5 mm in diameter (D_0) . The main experiments used re-machined sample dimensions of 4 mm $(L_0) \times 4$ mm (D_0) , and 3 mm $(L_0) \times 4$ mm (D_0) . Those dimensions were chosen to meet the condition, $0.5 < L_0/D_0 < 1$ [24]. Re-machining was completed using CNC lathe, and the tolerances specified for the length and diameter was ± 0.25 mm.

3.1.3 300M Steel

300M steel cylindrical samples were provided in longitudinal and transverse machined directions by the Heroux Devtek company. The chemical composition of the alloy is presented in Table 3.3.

Element	С	Mn	Si	P	S	Cr	Ni	Mo	V	Cu
Min (wt%)	0.4	0.65	1.45			0.7	1.65	0.35	0.05	
Max (wt%)	0.44	0.90	1.80	0.010	0.008	0.95	2.00	0.45	0.10	

Table 3.3. 300M Steel composition based on manufacturing specification AMS 6257E.

Initial sample dimensions 8.9 mm $(L_0) \times 6.1$ mm (D_0) were re-machined to 3 mm $(D_0) \times 4$ mm (L_0) by CNC lathe. The machining tolerances specified for the length and diameter were ± -0.01 inch. Following machining, heat treatment steps based on AMS 6257E was applied to Hopkinson samples as follows:

- 1. Austenitization at 827°C for 30 minutes followed by oil quenching.
- 2. Tempering at 302°C for 30 minutes followed by air cooling.

Heat treatment was performed using a laboratory scale box furnace without a protective atmosphere. To limit de-carburization, a heat-treatment steel foil was used to cover the samples during heat treatment. Heat treated samples were polished with a 600 grit sand paper to remove decarburized layers on both surface ends for Rockwell macro-indentation hardness tests.

A value of 53 HRC obtained after tempering confirmed the expected mechanical properties of the samples based on the AMS standard 6257E.

3.2. SHPB Experiments Summary

The test conditions and number of tests completed using the Split-Hopkinson bar method are presented in Table 3.4 for Aluminum 7050-T7451, and Table 3.5 for IN718 and 300M Steel. The initial sample dimensions and strain rates measured for each test are further detailed in the results section in Chapter 4. The gas pressures are those applied using the SHPB gas gun.

Table 3.4. Summary	v of AA7050-T7451	experiments for	or three machined orientations.
Tuoic 5. 1. Duillilliui	, 01 111 1/050 1/151	experiments to	ince machinea orientations.

Sample Dimensions $L_0 \times D_0$ (mm)	Gas Pressure (PSI)	Temperature (°C)	Strain Rate (s ⁻¹)	Short Transverse	Transverse	Longitudinal
6.09 ×6.45	280	25	2.8×10^{3}	-	-	1
	150	-110		3	-	-
6.09×6.45	140	25	2×10^{3}	3	3	3
	120	100		1	-	1
	90	200		3	3	3
5×5	85	25	850	1	-	-

Table 3.5. Inconel 718 and 300M steel experiments summary.

Sample Dimensions $L_0 \times D_0$ (mm)	Gas Pressure (PSI)	Temperature (°C)	Strain Rate (s ⁻¹)	IN718 – Longitudinal	IN718- Transverse	300M - Longitudinal
3×4	280	25	6.7×10^3	1	-	
3×4	200 190 120	-110 25 500	4×10 ³	3 3 1	2	-
3×4	200	25	3×10^{3}	-	-	3
4×4	180	25	2.7×10^{3}	-	1	-
3×4	190 180 110 80	-70 25 200 500	2.4×10^3	- - -	- - -	1 1 1 1

3.3 Compressive Split-Hopkinson Pressure Bar Setup

The SHPB compression setup located in the McGill Materials Engineering Department is shown in Figure 3.1. The Hopkinson setup loading bars were C-350 Maraging steel, supplied by REL Inc. in heat treated, straightened and ground condition. C-350 Maraging steel bars was utilized for their high strength and resistance to elastic indentation of the end-surfaces when testing IN718 and 300M steel alloys. The elastic modulus and density of the bars is 200 GPa and 8.0 (kg/m³), respectively [107].

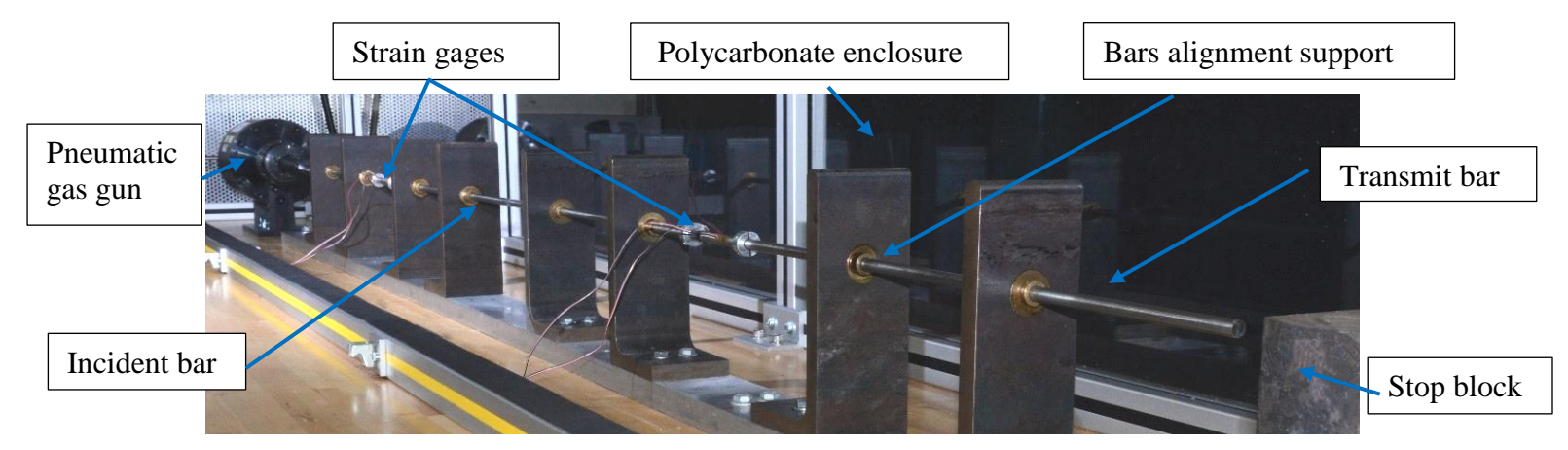


Figure 3.1. Compressive Hopkinson-bar setup: Loading bars with steel bracket supports and polycarbonate safety enclosure.

The incident and transmit bars were 9.52 mm in diameter and 1.14 m in length. The aspect ratio of the bars, $(L_b/D_b > 20)$, follows general recommendations to ensure one dimensional wave propagation. The striker bar was of the same material and diameter as the loading bars, and was 40 mm in length. The length of incident to striker bar ratio was greater than two, and meets the transient time criteria that no overlap occurs between the incident and reflected signals. The loading bars were aligned by vertical bracket supports with brass bearings. Horizontal alignment of the bars was checked by adjusting each of the vertical support until resistance to sliding motion became as minimal as possible, and visually inspected by placing together the bar-end surfaces. The SHPB gas gun was controlled manually via a pneumatic circuit indicated in Figure 3.2. A controller was used to adjusted the gas gun pressure level, that was indicated by a pressure gauge, and to launch the striker bar. As part of the system was a safety circuit that allows for

pressurisation of the gas gun only when the polycarbonate cover is completed closed over the Hopkinson bars. The operation range of the gas gun was from 50 to 250 PSI.



Figure 3.2. Pneumatic control panel and gas gun pressurisation controller.

For data acquisition, impact-wave signals were measured by foil-type gages (EA-06-062AQ-350) from Vishay Micro-Measurements group with a gage factor of 2.13. The strain gages and wiring terminals were bonded to the bar using M-Bond 610 epoxy adhesive, and further secured by polyester thread as shown in Figure 3.3.

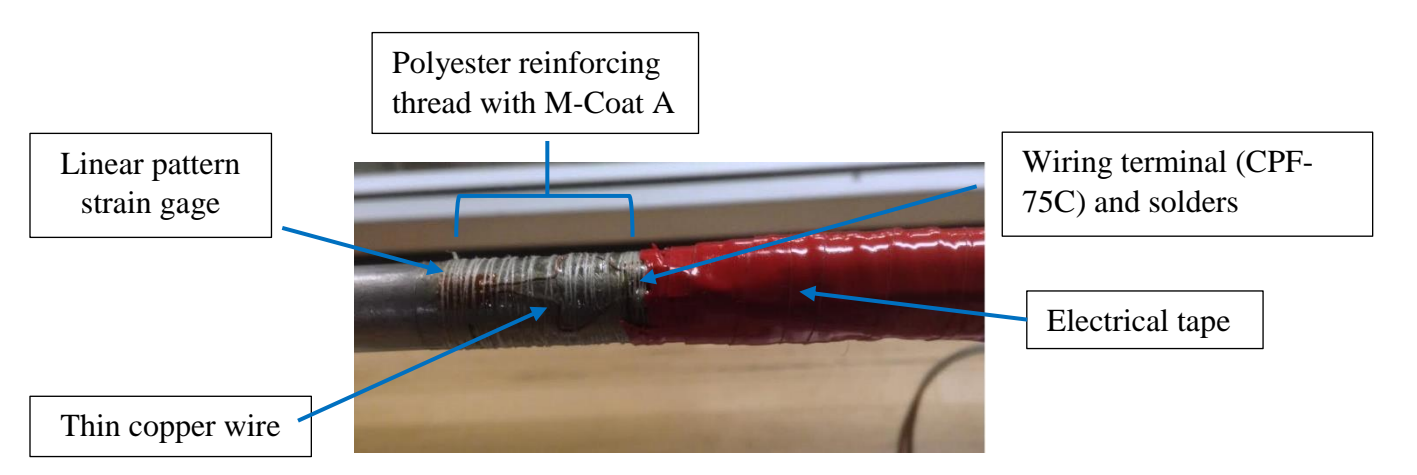


Figure 3.3. Foil type strain gage attachment on incident bar.

A pair of gages were positioned at the center of each bar. The gages were bonded diametrically to form a half Wheatstone bridge configuration, as shown in Figure 3.4, to cancel minor bending effects. In the configuration, strain gages attached to opposite legs are balanced by two 350 Ohm resistors, labeled R. An external power supply provides 10 V input voltage to the bridge. The strain gage connections to an oscilloscope (Nicolet Pro 40) for recording voltage signals is shown in Figure 3.5. A circuit box houses the resistors and 4 lead wires connections from each pair of strain gages. A potentiometer installed in each box enables manual balancing or zeroing of the circuit voltage prior to setting the scope trigger function. The circuit boxes are connected to the oscilloscope via BNC cables. The oscilloscope has 10 MHZ frequency response and 4 BNC cable input ports. The positive and negative BNC cable terminals from each circuit box are located on the same vertical panel. Channels 2 and 3 each measures the incident / reflected wave, and the transmitted waves, respectively.

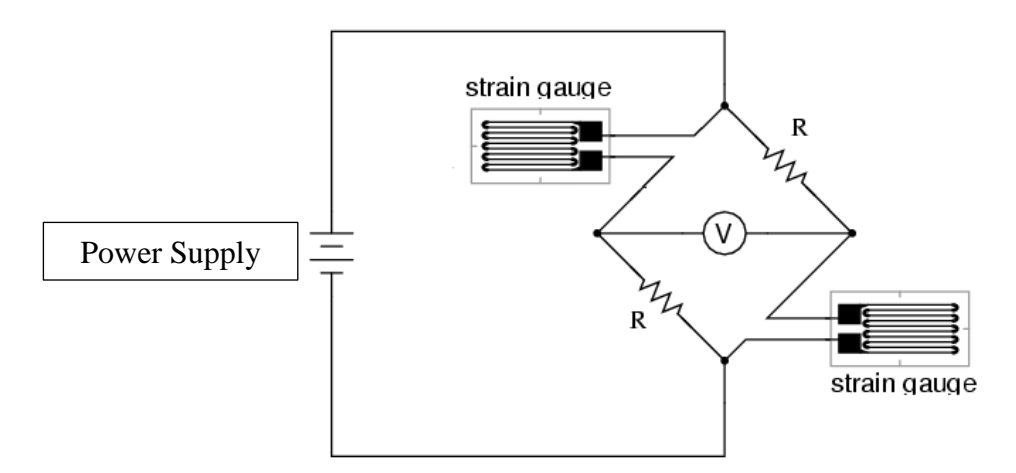


Figure 3.4. Illustration of a half Wheatstone bridge circuit adapted from a handbook on Split Hopkinson bar design and applications [108].

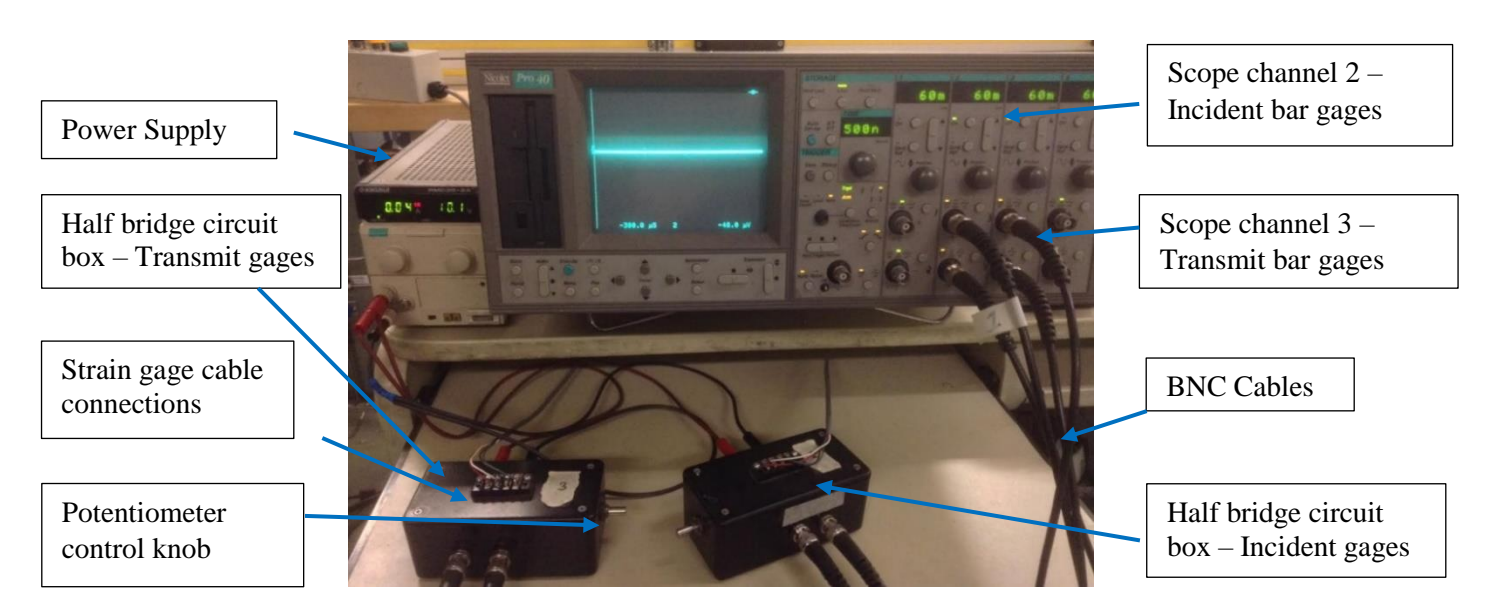


Figure 3.5. SHPB data acquisition setup.

3.3.1 SHPB Heating and Cooling Setup

High temperature apparatus for elevated temperature Hopkinson tests involved a radiative furnace using quartz tube lamps shown in Figure 3.6. The furnace consists of side openings for manually placing the loading bars and sample into the furnace enclosure. Within the enclosure lies of a water circulation line for cooling the furnace components during operation. A manual temperature controller varies the power supplied to the halogen lamps that controls the heating rate. A K-type thermocouple (0.020''diameter) wire placed in contact with the surface of the incident bar and around 1 cm from the bar-sample interface, was used to represent the sample temperature. The maximum temperature attainable using the furnace is 500°C measured at the position of the thermocouple. At this temperature, the bar temperature at the strain gage position (57 cm away) was maintained at 25°C with the bar supports acting as heat sinks. The maximum test temperature used is also below the critical value that requires correction for effects of thermal gradients on elastic modulus, which is around 600°C for steel bars [109]. Using the bar surface temperature is reasonable given the small sample volume relative to the bars, and the high thermal conductivity of the metallic bars and samples.



Figure 3.6. Radiative furnace placement at bars-sample interface.

For sub-room temperature tests, liquid nitrogen was used as the coolant. A Styrofoam box was used as an insulating container located between the two bars as shown in Figure 3.7. Circular openings cut-out on the sides of the box for the bars to be placed within the container. To enable cooling, liquid nitrogen was poured directly into the container with sample and loading bars pre-placed in the center. The bar and the sample temperatures were lowered by the contact with the cold gas. The container wall thickness is 2.54 cm (one inch) and the total internal volume is ~0.8 liters (54 cubic inches). A T-type thermocouple placed on the surface of the incident bar, as in the case of heating experiments, outputs the temperature to a digital reader. Varying cooling temperatures were obtained by adjusting the initial volume of liquid nitrogen in the container. The lowest temperature attainable at steady state, over a minimum time of 10 minutes was -110°C. The lowest temperature corresponds to an initial liquid nitrogen surface level slightly below (not contacting) the bars, that amounted to approximately ~0.65 liters (40 cubic inches) of liquid nitrogen.

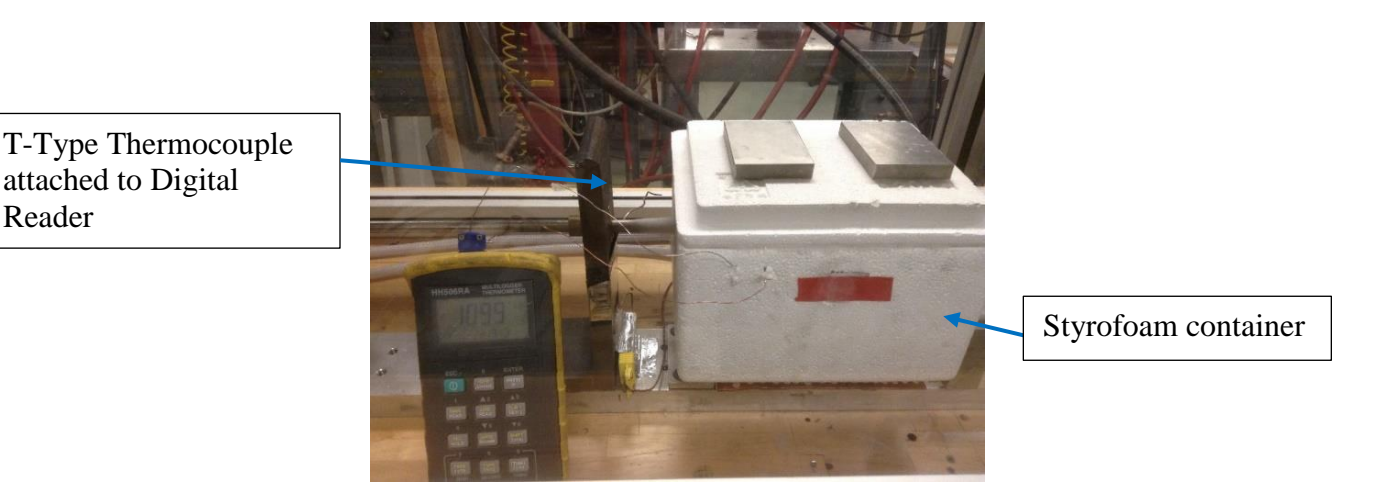


Figure 3.7. Styrofoam insulation container at bars-sample interface.

3.4 Pulse Shaping

Reader

Aluminum 6061 and multi-purpose Copper 110 sheets (from McMaster Carr) were used to produce circular pulse shaper pieces using a hand-held punch tool. The shaper thickness (0.2-2 mm) and diameter (smaller than the bar diameter), were based on commonly applied ductile metal shapers discussed in the literature review. An example of a test for an Aluminum 7050-T7451 sample (6.40 mm L_0 and 6.09 mm D_0) using an Aluminum 6061 shaper is shown in Figure 3.8. The pulse shaper used was AA6061, with a thickness of 0.5 mm and diameter of 4 mm. The recorded signal without the use of pulse shaper shows dispersion effects in the form of oscillations in the incident and reflected pulses. With a pulse shaper, the rise time, or the time from zero voltage to peak voltage value, increases in the incident pulse. Dispersion effects in the incident and reflected signals are also removed. The transmitted signal, in the case without a pulse shaper, is relatively free of dispersion effects because oscillations are dampened by the plastic strain of the sample. The pulsed shaper materials and dimensions used for each material are summarized in Table 3.6.

3.96

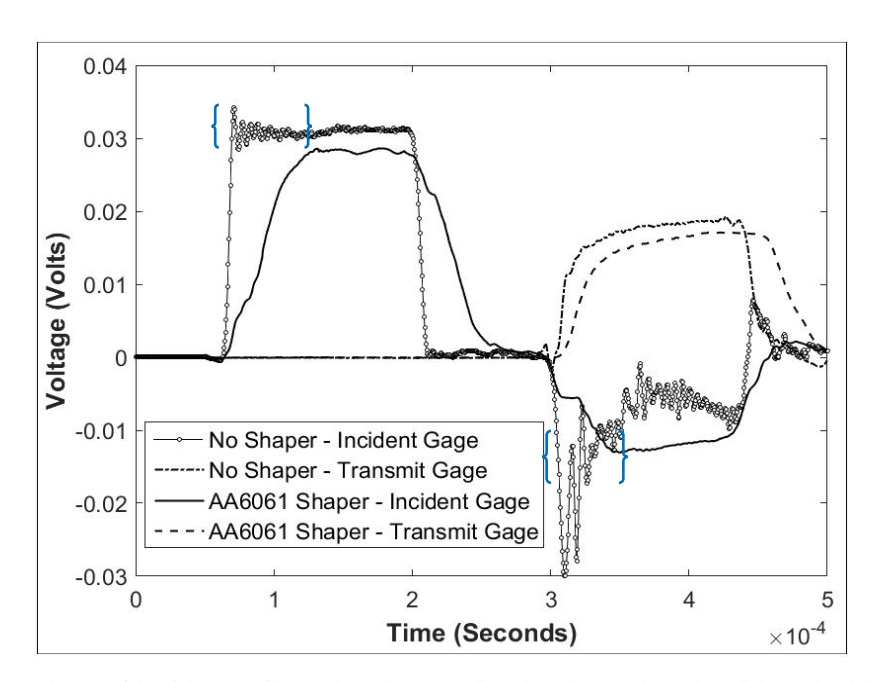


Figure 3.8. Comparison of incident/reflected and transmitted voltage signals with and without using a pulse shaper for AA7050-T7451. Test conditions were 140 PSI and 25°C. Dispersion effects in the incident and reflected pulses are indicated in brackets.

 Sample
 Pulse Shaper
 Thickness (mm)
 Diameter (mm)

 Aluminum 7050-T7
 Aluminum 6061
 0.41
 3.96

 IN718
 Aluminum 6061
 0.64
 3.96

0.64

Copper 110 (Annealed)

Table 3.6. Pulse shapers applied for each Hopkinson-bar test sample.

3.5 Data Processing and Evaluation

300M

The stress-wave voltage signals used for equilibrium stress-strain calculations are processed manually by visual inspection as shown in Figure 3.9 for an Aluminum 7050-T7451 sample. With the use of a pulse shaper, the start of each signal marked by the zero-voltage point was relatively straightforward to identify.

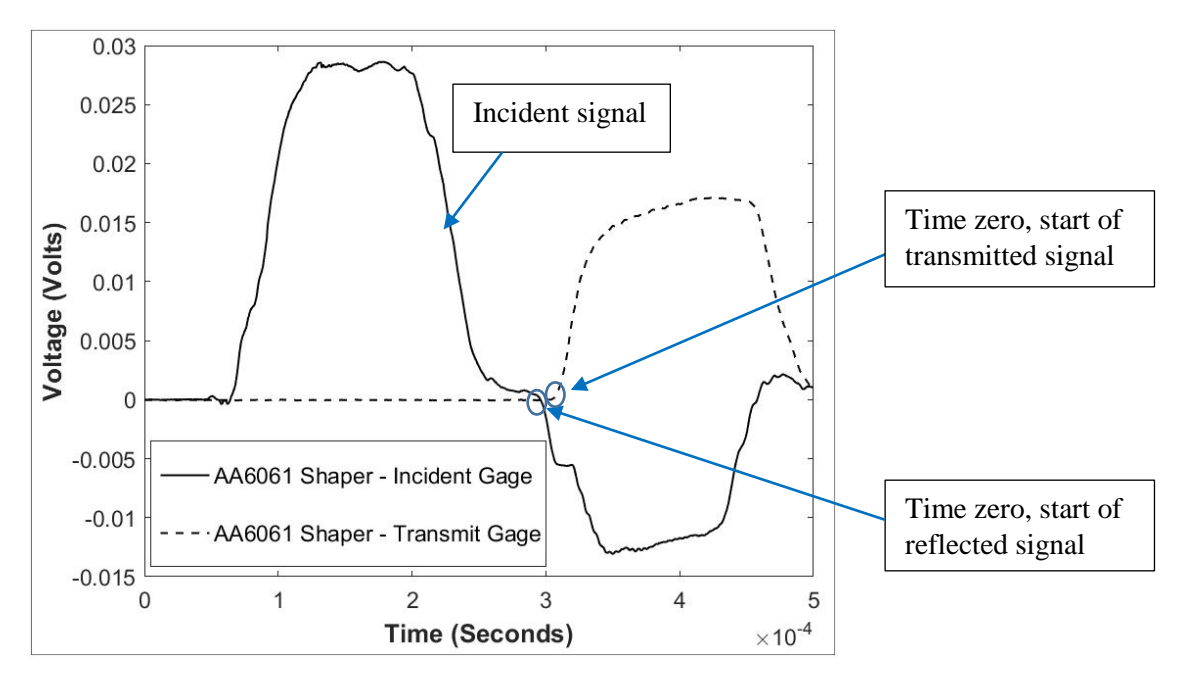


Figure 3.9. Oscilloscope voltage signals for a AA7050–T7451 sample using AA6061 pulse shaper. Identification of the starting point of the reflected and transmitted wave.

In the example, data points between the zero voltage and end of the signal plateau are initially converted to strain gage micro-strains. In some cases, shear failure occurs to the sample during compression, and the plateau of the signal consist of intermittent peaks within the signal plateau region. In such cases, the steady-state voltage interval prior to indication of sample failure may still be applied to evaluate the micro-strain values. The strain gage micro-strain (ε) is related to the voltage measured (V_0) and input voltage (V_1) by [108].

$$\varepsilon = \frac{2}{G_{\rm F}} \frac{V_{\rm o}}{V_{\rm I}} \tag{3.1}$$

The strain gage factor (G_F) was 2.13 and the input voltage (V_I) was 10 V for the setup. The micro-strain data evaluated for the reflected and transmitted signal voltages of AA7050-T7451 data presented in Figure 3.9 are shown in Figure 3.10.

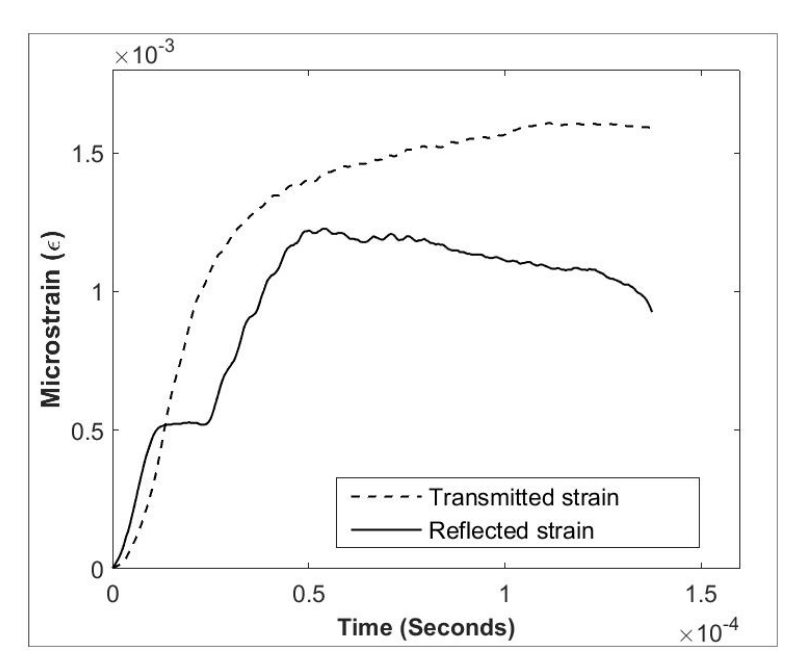


Figure 3.10. Strain gage micro-strains evaluated from reflected and transmitted signals for AA7050-T7451.

The reflected micro-strain values $\varepsilon_R(t)$ are used to evaluate the engineering strain $\varepsilon(t)$ and strain rate $\dot{\varepsilon}(t)$ with equations 2.2 and 2.3 shown in the literature review. The transmitted micro-strains $\varepsilon_T(t)$ were applied to evaluate engineering stress (σ) using equation 2.1. The true stress, strain, and strain rates were then computed as,

$$\sigma_{\text{true}} = \sigma \left[1 - \varepsilon(t) \right]$$
 (3.2)

$$\varepsilon_{\text{true}}(t) = -\ln[1 - \varepsilon(t)]$$
 (3.3)

$$\dot{\varepsilon}_{\text{true}}(t) = \frac{\dot{\varepsilon}(t)}{1 - \varepsilon(t)} \tag{3.4}$$

The true stress-strain result evaluated for the data in Figure 3.10 using equations 3.2 and 3.3 is shown in Figure 3.11. A finite strain or duration is taken for the stress to reach a plateau due to

wave propagation effects as discussed in the literature review. To estimate the start of plastic strain from the stress-strain curve, the intersection between the dashed lines tangent to the slope of the initial loading phase and the plastic stress was used as the initial strain value. The method was presented by Curtze et al. [110] for estimating the yield strength of high-strength steel from compressive Split-Hopkinson bar test results. The estimated value, around 2% true strain in this example, is comparable to the early yield strain of ductile metals subjected to dynamic compression with pulse shapers applied [43].

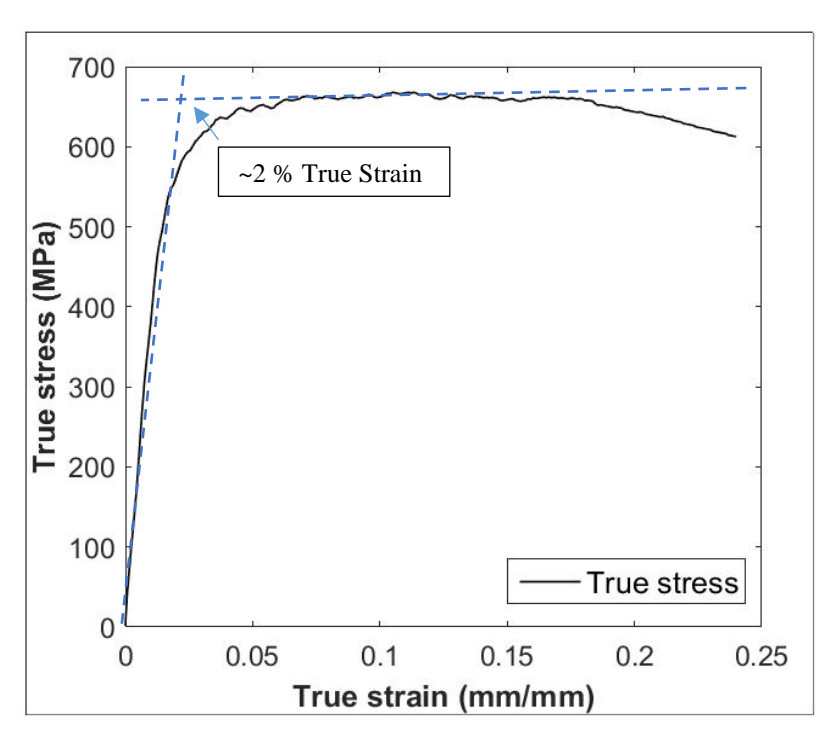


Figure 3.11. True stress vs true strain for AA7050-T7451 at 25°C. Estimation of initial strain value.

3.5.1 Average Strain Rate

The true strain rate evaluated for the AA7050-T7451 data in Figure 3.11, overlapping the true stress, is presented in Figure 3.12. The true strain values at each strain were evaluated using equation 3.4. For defining a strain interval to estimate an average true strain rate, the initial strain was taken as 2% based on the intersection method shown in Figure 3.11. The final strain value was estimated using the measured length of the post-strained sample using a digital micrometer. In the example, the initial and final sample length was 6.40 mm and 5.09 mm, respectively.

The deformed sample strain, evaluated as $(L_0 - L_{\rm f}) / L_{\rm f}$, was around 20%. The average strain rate $(\varepsilon_{\rm avg})$ between 2 % and 20 % true strain was $1950 {\rm s}^{-1}$ as shown in Figure 3.12. The standard deviation of the average strain rate (s) was determined as,

$$s = \sqrt{\frac{1}{n(n-1)} \sum_{i=1}^{n} (\dot{\epsilon}_i - \overline{\dot{\epsilon}})^2}$$
 (3.5)

where (n) is the number of data points. The average strain rate in Figure 3.12 was $1950 \pm 14s^{-1}$.

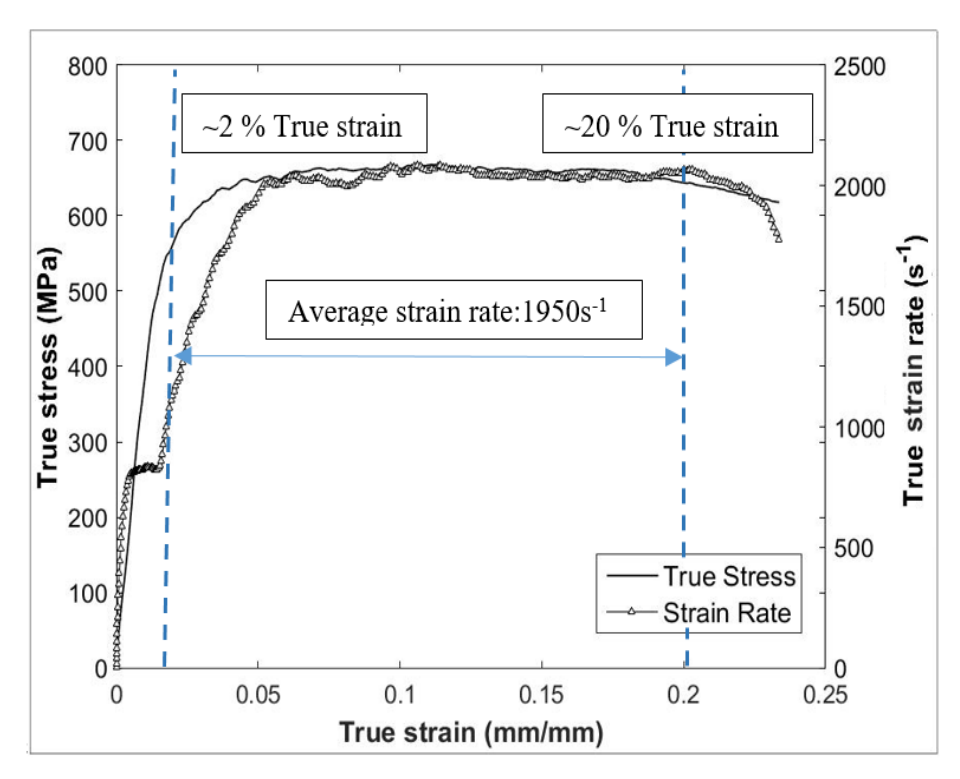


Figure 3.12. True stress and strain rate vs true strain for AA7050-T7451 at 25°C. Illustration of the true strain interval used to estimate the average strain rate of the result.

The method of estimating the initial, final strain, and average strain rate was applied for all materials and test conditions. For specific tests where the sample exhibited shear during compression, the final strain corresponds to the end of the steady-state reflected and transmitted signals intervals used for the stress-strain plot.

3.5.2 Strain Hardening Rate and Thermal Softening

From a SHPB true stress-strain test result, the strain hardening rate at a specific test temperature was defined as the change in stress (MPa) over the change in strain as,

$$\frac{\partial \sigma}{\partial \varepsilon} = \frac{\sigma_{i} - \sigma_{i-1}}{\varepsilon_{i} - \varepsilon_{i-1}} \quad i \ge 1$$
(3.6)

where (σ_i) and (ε_i) are the true stress and true strain at point (i), respectively. For evaluating the strain hardening rate at a specific strain (ε) , the increments (ε_i) and (ε_{i-1}) (and the corresponding stress at each strain value) were defined as $\varepsilon \pm 0.01$. For evaluating the effect temperature between two tests of comparable strain rate, the difference of stress (MPa) at a specific strain due to the difference in temperature was defined as thermal softening. The definition is shown in equation 3.7 as,

$$\frac{\partial \sigma}{\partial T} = \frac{-[\sigma_1 - \sigma_2]}{T_1 - T_2} , \qquad T_1 > T_2$$
 (3.7)

The negative sign was applied to make the thermal softening value a positive one, given the stress decreases with increasing test temperature. The strain hardening and thermal softening definitions were adapted from the study by Chen et al. [67]

3.6 SHPB Compression Testing Summary

For each experiment, the initial sample length, diameter and final length were measured using a digital micrometer (Mitutoyo). In the measuring range of 0-25 mm, the resolution and accuracy of the micrometer are 0.001 mm and 0.002 mm, respectively. The measurements were utilized to estimate the final strain and the range of strain used to average the strain rate of the sample. A piece of circular metallic sheet, attached to the impact-end of the incident bar, was used as a pulse shaper. The sample was manually placed between the two bars, and alignment of the bars and sample was checked visually. Boron nitride powder was applied on both ends of bar-sample interfaces to minimize friction for room and temperature variation tests. For heating and cooling tests, the sample was held at a specific target temperature for about 5 minutes prior to testing.

3.7 Quasi-Static Tensile Tests

Quasi-static tensile results at 25°C for AA7050-T7451 ([111] C. Bianchetti, private communication, October, 2, 2015), IN718 ([112] T.Koltz, private communication, October 2, 2015) and 300M Steel ([113] A.Bag, private communication, September, 23, 2015), were completed in separate work as part of the shot peening, fatigue life analysis project. The data were measured using a 100KN MTS servo-hydraulic machine, with cylindrical round-bar sample and dimensions based on ASTM E8 standard. LVDT longitudinal and axial extensometers were applied. The sample gage length was 50 mm for AA7050-T7451, and 25 mm for IN718 and 300M steel. The strain rates were 10^{-4} s⁻¹ for all tests and three tests were performed for each sample and orientation presented in Figure 3.13.

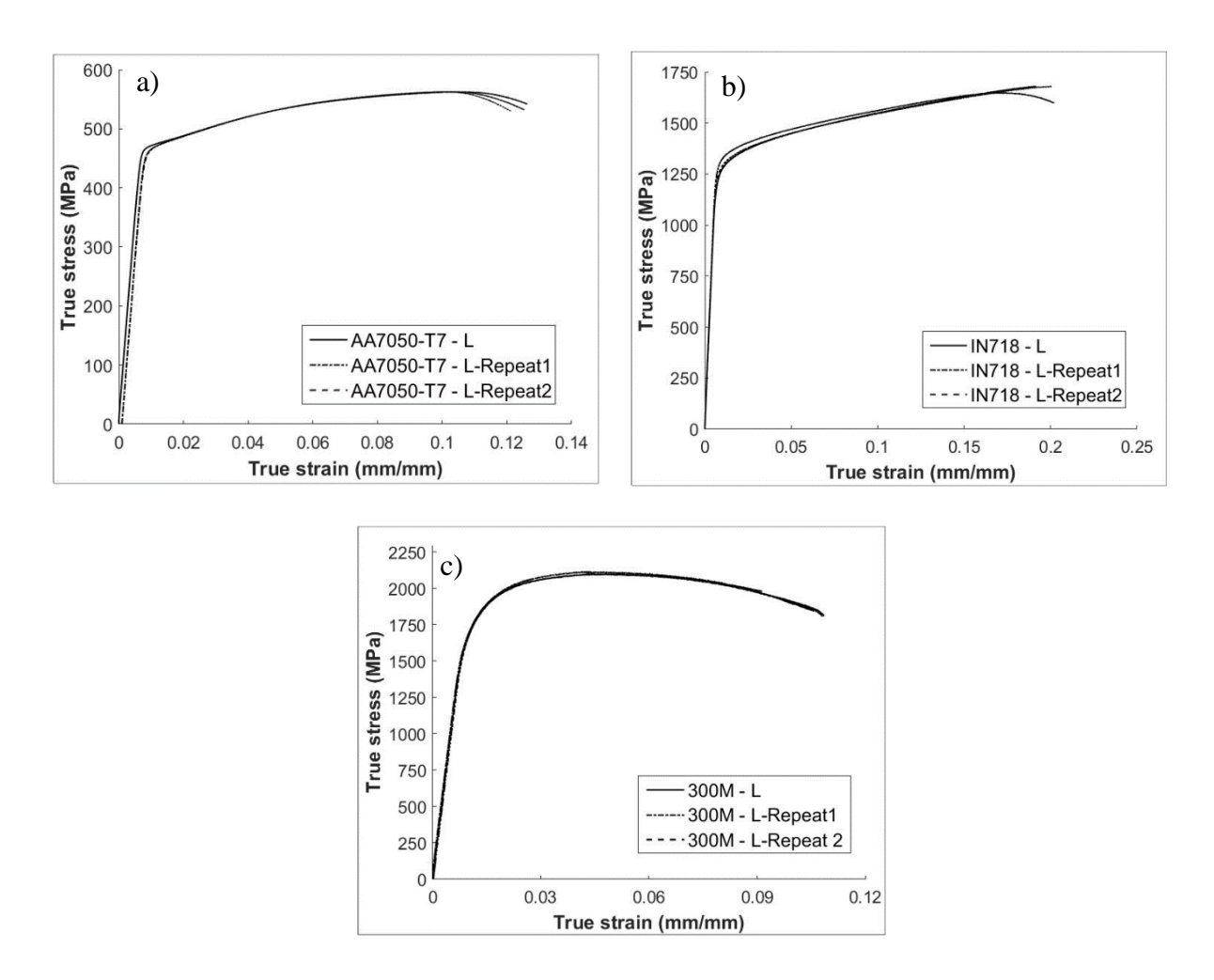


Figure 3.13. Quasi-static tensile test results at 25°C, true stress vs true strain. a) Aluminum 7050-T7451. b) IN718. c) 300M Steel.

3.8 Constitutive Model Fitting

In evaluating constitutive models investigated in this work, a Matlab routine, *Lsqnonlin*, was used for fitting to the experimental data by the least squares method. The varying strain rate and temperature stress-strain results were fitted altogether to evaluate the model parameters, based on the method used by Johansson and Persson [114]. The elastic region of each stress-strain result was subtracted from the plastic stress-strain region: $\varepsilon_p = \varepsilon_T - E/\sigma$, where (ε_T) is the true strain and (E) is the elastic modulus. The function (F) to be minimized is the difference between the material model and the measured stress. In using the Johnson Cook model for example, F was the following,

$$F = \left[\left[A + B\epsilon_{p}^{n} \right] \left[1 + C \ln \left(\frac{\dot{\epsilon}}{\dot{\epsilon}_{ref}} \right) \right] \left[1 - \left(\frac{T - T_{r}}{T_{m} - T_{r}} \right)^{m} \right] - \sigma_{exp} \right] \times w$$
 (3.8)

A weight factor (w) is defined as $1/\sqrt{n}$ for (n) data points in each experimental condition. The square root is applied for the weights as the *Lsqnonlin* routine takes the residuals instead of the squared residuals. To evaluate the function, lower and upper boundary values were defined for each parameter. Boundary values were needed to prevent optimized parameters from attaining unreasonably high or low values. The goodness of fit was evaluated by using the mean square error (MSE) and R^2 values (defined in Matlab as NRMSE) shown in equations 3.9 and 3.10.

$$\frac{\sum (y_{\text{fit}} - y_{\text{data}})^2}{N} \quad , N = \text{number of data points}$$
 (3.9)

$$R^2 = 1 - \frac{RSS}{TSS} \tag{3.10}$$

The MSE and R² values were evaluated for each test condition of an experimental data for each alloy. The values were also evaluated for all experiments together for an overall comparison between different constitutive models for each alloy. The Matlab code for the fitting evaluation is detailed in Appendix A.

Chapter 4 Results and Analysis

4.1 Aluminum 7050-T7451

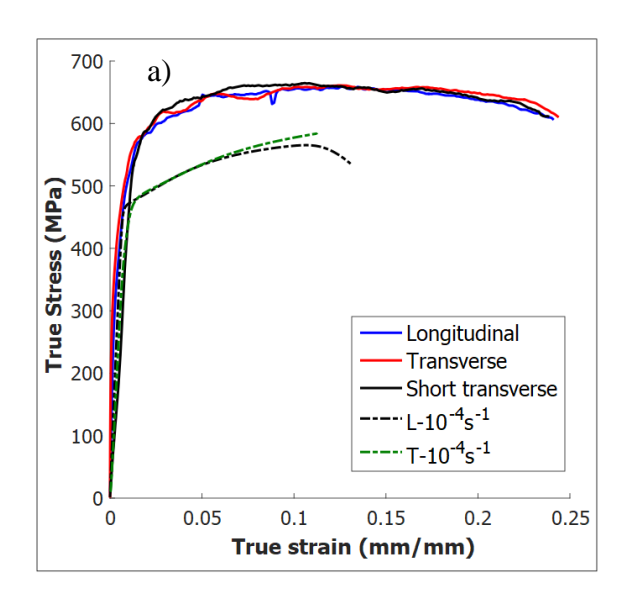
4.1.1 Strain Rate Sensitivity at 25°C

Dynamic compression tests for evaluating the strain rate sensitivity of AA7050-T7451 at 25°C are summarized in Table 4.1. The sample dimensions used for most tests are as received. Using the as-received sample dimensions, a gas-gun pressure of 140 PSI enabled a dynamic strain rate of $2000s^{-1}$ and a true strain of around 20%. Gas pressure of the pneumatic launcher was adjusted to enable different strain rates. A smaller sample of 5 mm (L_0) × 5 mm (D_0) was used to obtain a lower strain rate of $850s^{-1}$. A reduced dimension sample served to lower the sample inertia and enable sufficient strain when a low gas pressure is used. The deformed sample strain was evaluated based on initial (L_0) and final (L_1) sample length measured by the digital micrometer.

Table 4.1. Hopkinson test conditions for AA7050-T7451 at 25°C.

Figure	Sample Orientation	Gas Pressure (PSI)	Avg. Strain Rate (s ⁻¹)	L_{o} (mm)	$L_{\rm f}$ (mm)	Deformed Sample Strain (%)
4.1	L	140	2040 ± 15	6.45	5.07	21.4
	T	140	2140 ± 12	6.45	5.04	21.9
	ST	140	2140 ± 18	6.54	5.10	22
	L	200	2750 ± 48	6.35	N/A - Shear	NA
4.2	ST	140	1950 ± 13	6.45	5.04	21.4
	ST	110	1020 ± 9	6.43	5.75	10.6
	ST	85	850 ± 8	5.01	4.61	8.0

True stress-strain results of AA7050-T7451 for the three machined orientations are presented in Figure 4.1 a). The stress-strain results for the different orientations measured at an approximate strain rate of 2000s⁻¹ were relatively close. The dynamic strain rates measured, shown in Figure 4.1 b), were also similar. The SHPB results are compared to quasi-static tensile tests at 10^{-4} s⁻¹ for longitudinal (L) and transverse (T) orientation samples. Strain rate sensitivity between 10^{-4} s⁻¹ and 2000s⁻¹ for longitudinal and transverse samples are essentially identical. Although quasi-static tests were not performed for the short transverse (ST) direction sample, mechanical anisotropy is not evident for AA7050-T7451 at 25°C.



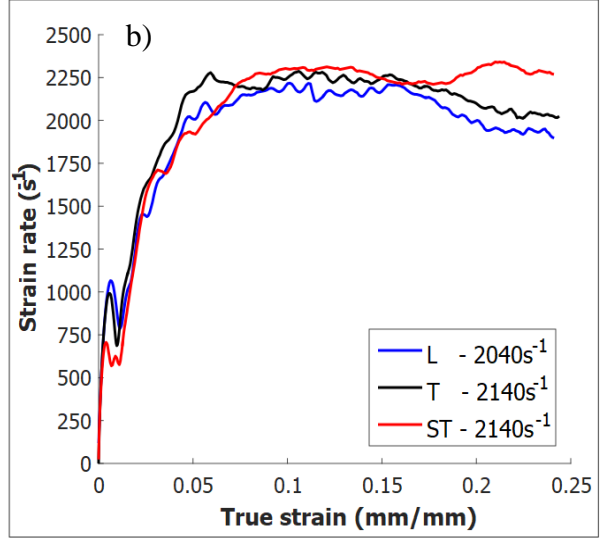


Figure 4.1. Comparison of AA7050-T7451 sample orientations for strain rates of 2000s⁻¹ and 10⁻⁴s⁻¹ at 25°C. a) True stress vs true strain. b) Strain rate vs true strain for dynamic strain rate results.

Varying strain rate tests at 25°C are presented in Figure 4.2. The stress-strain curve displays initial positive work hardening up to 10% true strain, after which the stress saturates and softening occurs. The strain hardening behavior is comparable to literature results reviewed for AA7050-T7451 shown in Figures 2.7 and 2.8. The highest strain rate attained is 2750s⁻¹, where sample failure occurred by shearing likely due to adiabatic heating, strain localisation effects. The peak stress attained is about 650 MPa. The strain rate sensitivity, shown in Figure 4.3 a), displays an increase in strength above 10^3 s⁻¹. In Figure 4.3 b), the strain hardening rate at 5% true strain are greater for stress-strain results at strain rate of 850s⁻¹ and 1020s⁻¹ than the result at 1950s⁻¹. The trend maybe due to lower adiabatic heating effects at lower dynamic strain rates. A higher strain hardening was evaluated for the result of 2750s⁻¹, due to an oscillation in the stress-strain data between 4% and 6% true strain. At 10% true strain, strain hardening rates are similar for most conditions. The strain rate result at 2750s⁻¹ displays a negative strain hardening rate that indicates thermal softening effect is more pronounced. The degree of strain softening at 15% true strain is similar between the stress-strain results measured at 1950s⁻¹ and 2750s⁻¹.

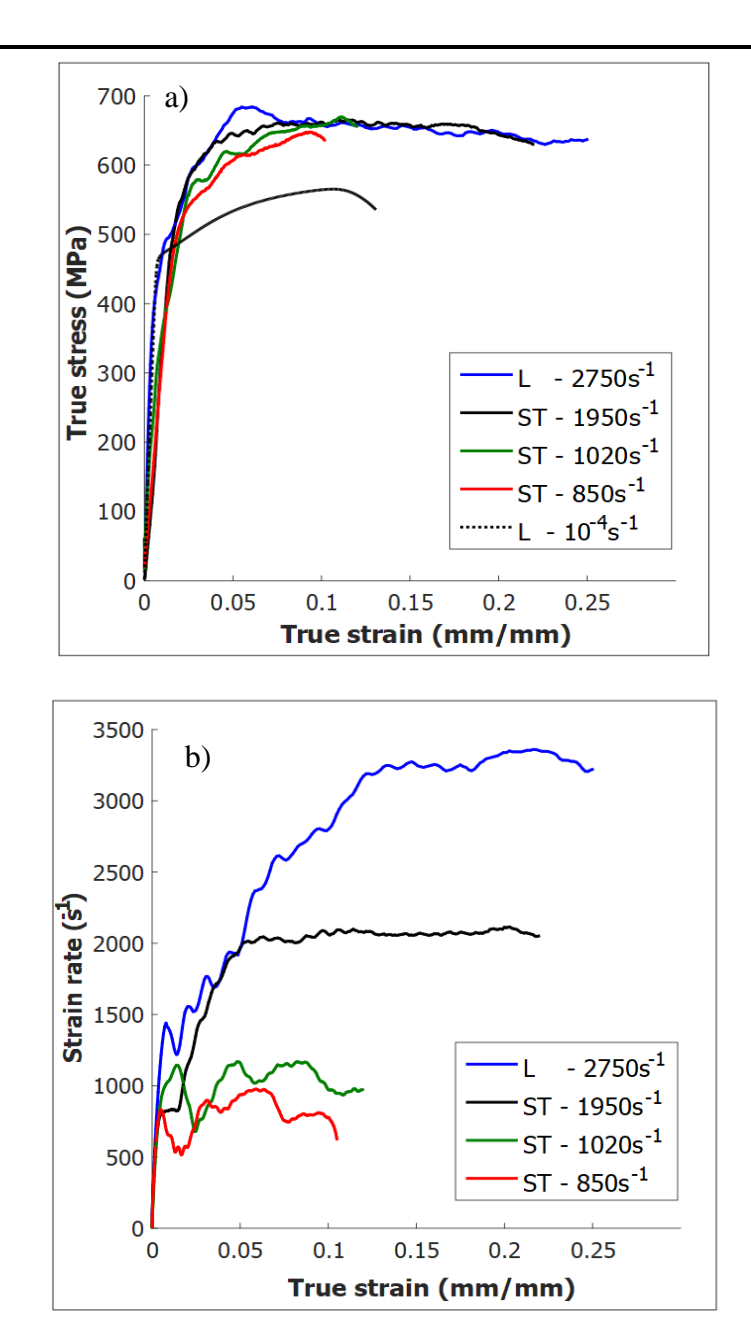




Figure 4.2. Strain rate sensitivity results of AA7050-T7451 at 25°C. a) True stress vs true strain. b) True strain vs strain rate. c) Deformed sample from varying strain rate tests.

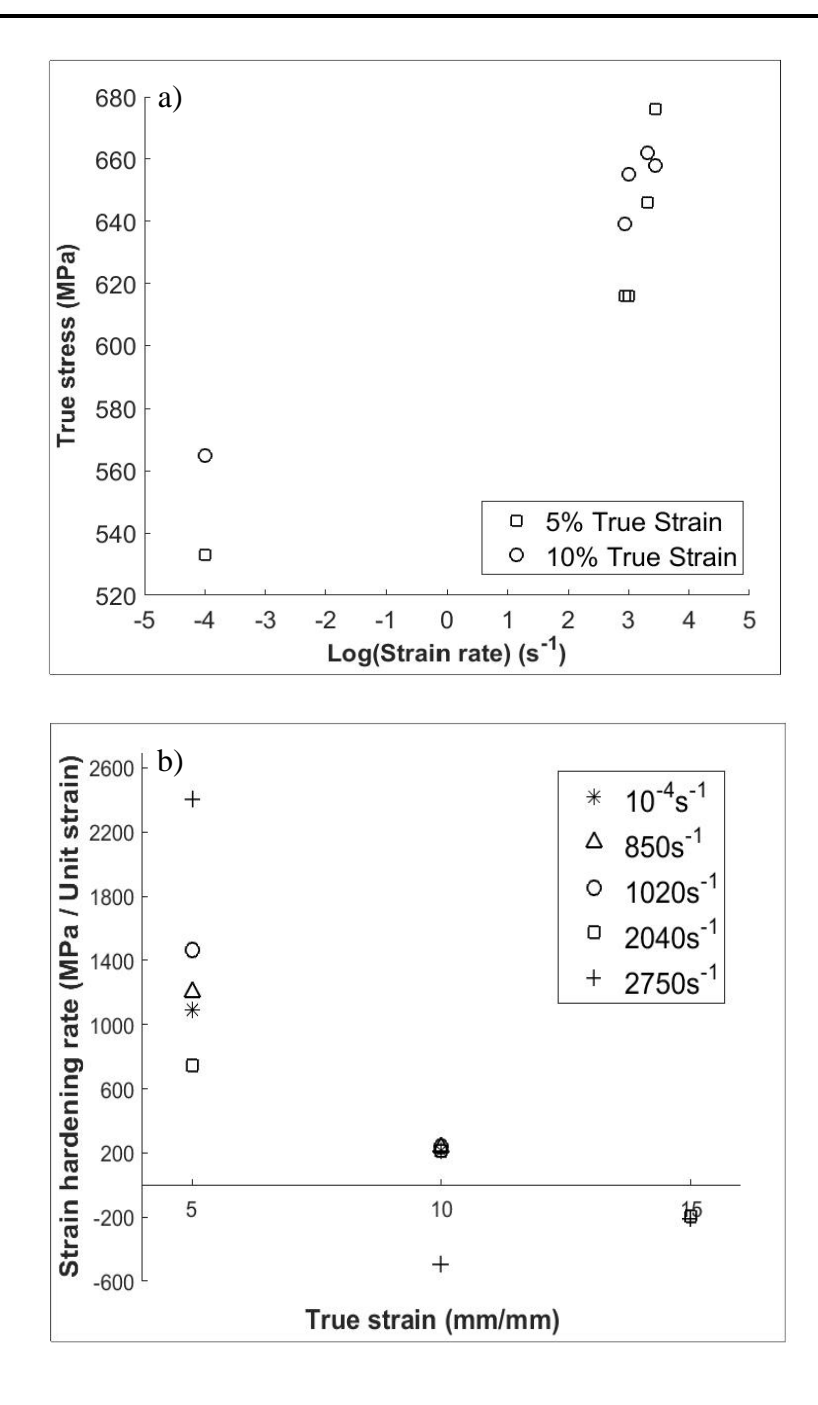


Figure 4.3. Strain rate sensitivity of AA7050-T7451 at 25°C. a) True stress vs strain rate. b) Strain rate hardening rate at varying strain rates.

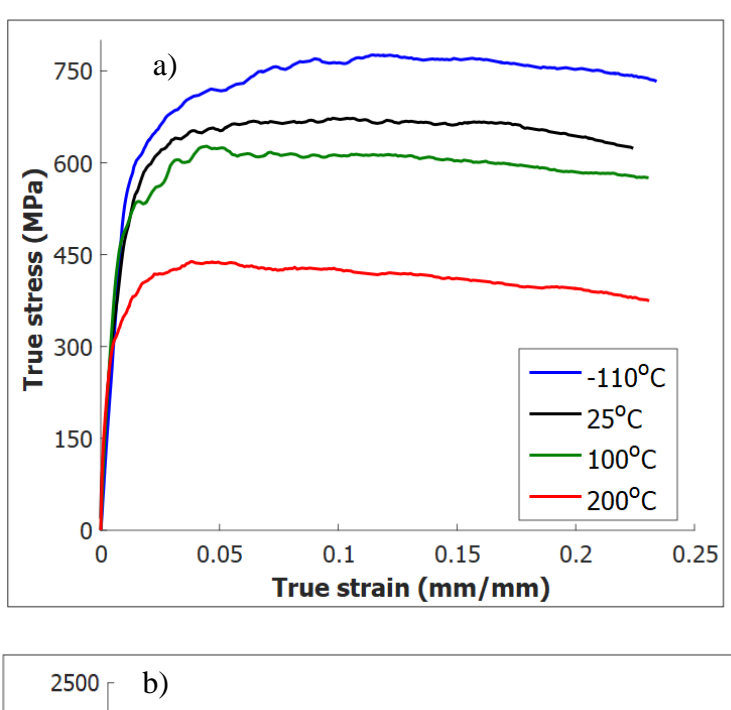
4.1.2 Temperature Dependence

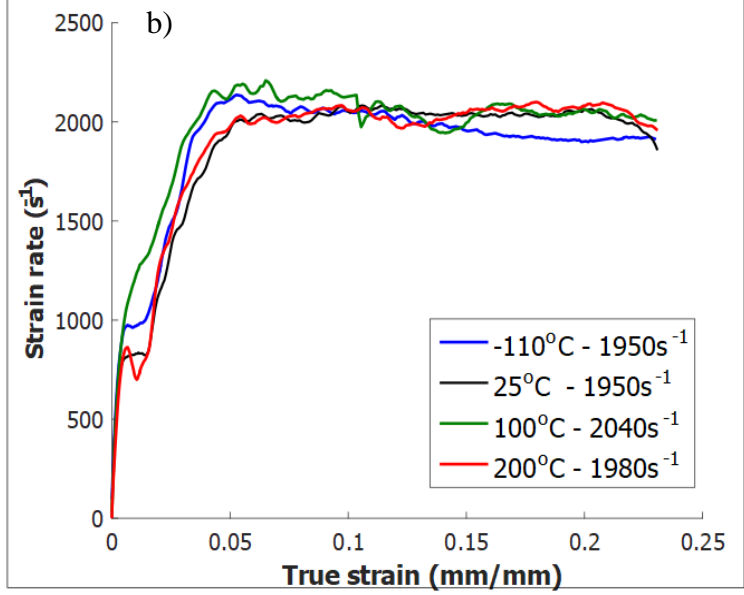
Experimental conditions for temperature sensitivity tests of AA7050-T7451 are summarized in Table 4.2. The target average strain rate was about 2000s⁻¹, where steady-state dynamic strain rate was attained at 25°C without shear failure occurring in the sample. To attain approximately the same average strain rate at different temperatures, the gas pressure was lowered for higher temperature tests to account for lower strength. The sample dimensions for all conditions were the same and samples used were in the short transverse orientation.

Table 4.2. Temperature dependent tests of AA7050-T7451 at a target strain rate of 2000s⁻¹.

Figure	Temperature (°C)	Gas Pressure (PSI)	Avg. Strain Rate (s ⁻¹)	L _o (mm)	L _f (mm)	Deformed Sample Strain (%)
4.4	-110	150	1950 ± 8	6.43	5.08	21.0
	25	140	1950 ± 13	6.45	5.04	21.4
	100	120	2040 ± 11	6.45	5.15	20.2
	200	90	1980 ± 12	6.42	5.05	21.3

The true stress-strain results are presented in Figure 4.4 a). The stress-strain result obtained at -110°C shows an increase in strength as expected with a lower degree of thermal activation. Similar to the result 25°C, the test at -110°C showed stress saturation between 10% to 15% true strain and softening from 15% true strain until the end of measurement. At 100°C and 200°C, strength is reduced and negative strain softening occurs over the majority the measured strain in both tests. The strain rate history shown in Figure 4.4 b) also consisted of similar trends and magnitude for all results. The strain of the deformed samples at varying test temperatures, by visual inspection, were relatively uniform and did not exhibit shearing on the outer surface.





Non-tested sample



Figure 4.4. Temperature sensitivity results of AA7050-T7451 at a nominal strain rate of 2000s⁻¹. a) True stress vs true strain. b) Strain rate vs true strain. c) Deformed samples from varying temperature tests.

The degree of thermal softening, shown in Figure 4.5 a), were close between the lower temperature intervals and increases at 200°C. The specific softening mechanism at 200°C thus maybe more pronounced or different than at 100°C. From the strain hardening rates shown in Figure 4.5 b), the trend at 200°C is comparable to the reference study discussed in Figure 2.10, where strain softening was attributed to dynamic recrystallization and phase transition. Similarly, stress saturation where strain hardening rate is close to zero maybe attributed to dynamic recovery.

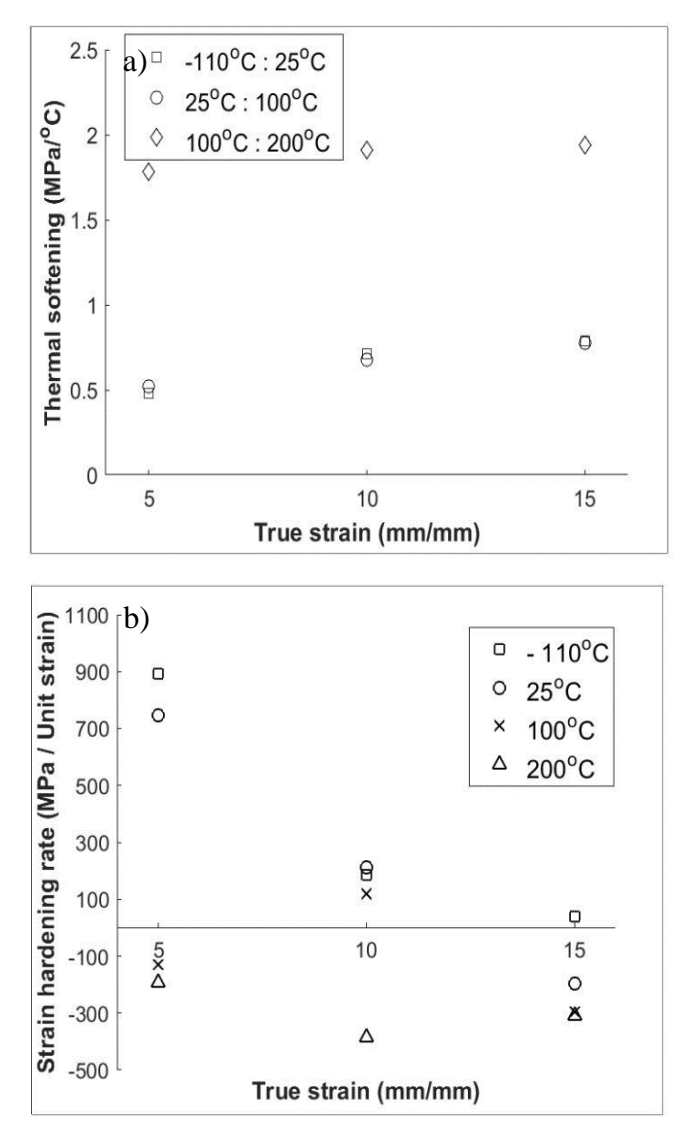


Figure 4.5. Temperature sensitivity of AA7050-T7451 at 5, 10 and 15% true strain. a) Thermal softening. b) Strain hardening rate.

4.2 Inconel 718

4.2.1 Strain Rate Sensitivity at 25°C

SHPB test conditions at 25°C for IN718 are summarized in Table 4.3. Given the high yield strength and density of the material, an initial sample dimension of approximately 4 mm (D_0) × 3mm (L_0) was used to enable a range of strain rates obtained by varying the gas pressure. A sample with initial length of about 4 mm was also used to enable a lower dynamic strain rate.

Figure	Orientation	Gas Pressure (PSI)	Avg. Strain Rate (s ⁻¹)	D _o (mm)	L _o (mm)	L _f (mm)	Deformed Sample Strain (%)
	L	280	6760±100	4.08	3.04	N/A- Shear	N/A
4.6	L	190	4000 ± 48	4.07	3.05	2.09	31.4
	T	190	3900±55	4.10	3.08	2.10	31.8
	Т	180	2770±53	4.03	4.02	3.14	21.9

Table 4.3. Dynamic strain rate tests of IN718 at 25°C.

The comparison of SHPB tests and quasi-static tensile results are shown in Figure 4.6 a). The dynamic stress-strain results in general maintained a positive strain hardening up to 30% true strain and stress saturation occurs gradually until the end of measurement. For the result at strain rate of $6760s^{-1}$, an initial oscillation peak was measured between true strains of 5 to 20%. Strain softening is evident starting at around 33% true strain and the sample sustained significant shearing. The results for the longitudinal and transverse orientation samples obtained at $3900s^{-1}$ and $4000s^{-1}$ overlap closely together, indicating machining orientation has a negligible effect on strain hardening for the material. The dynamic strain rate measured, shown in Figure 4.6 b), reaches a peak level after around 5% true strain. The measured rate however did not maintain a constant level after for several of the tests. A steady strain rate level was attained for the result at $6760s^{-1}$, although the loading phase to reach the plateau was relatively longer in comparison to the results at lower strain rates.

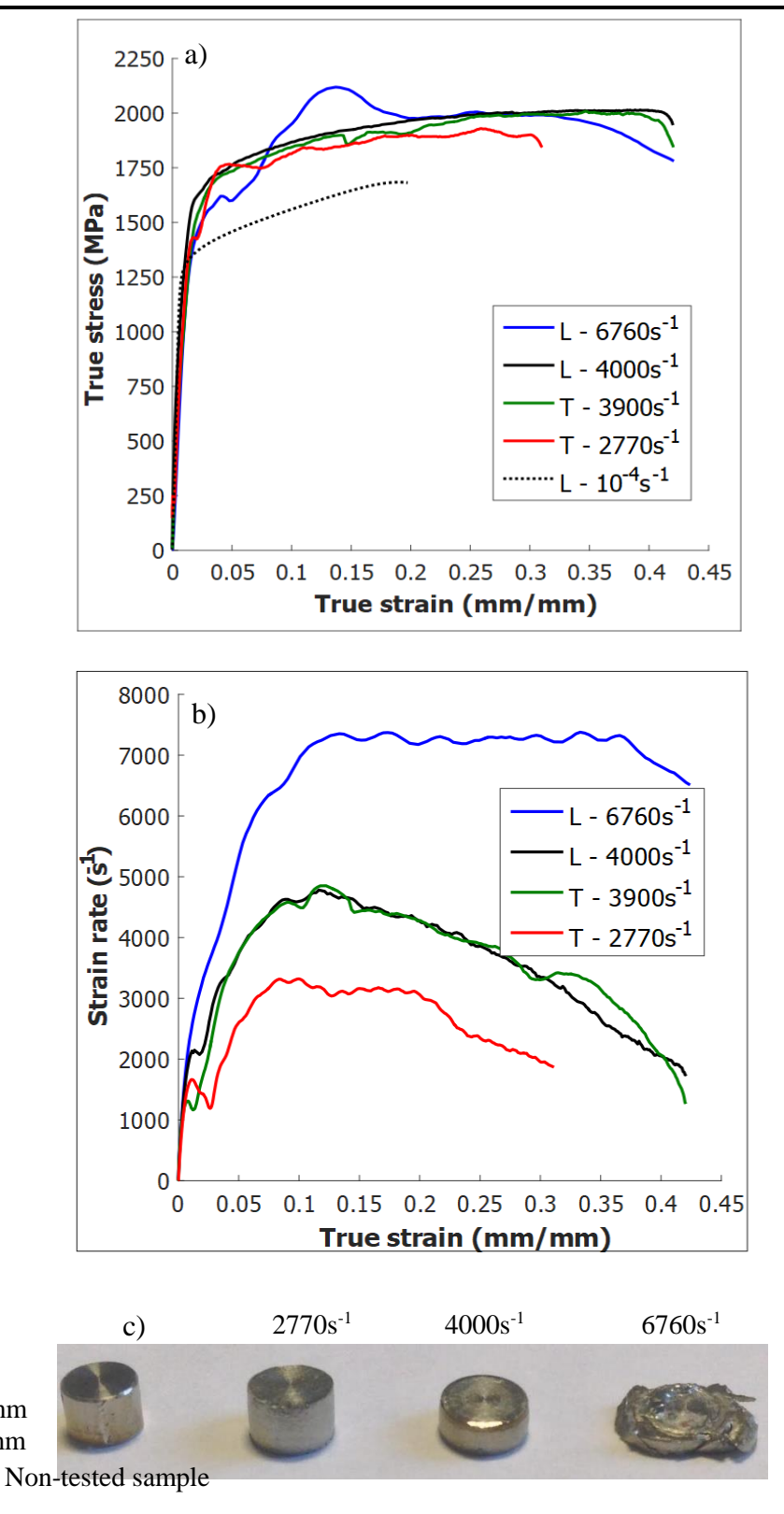


Figure 4.6. Dynamic stress-strain and quasi-static tensile results of IN718 at 25°C. a) True stress vs true strain. b) Dynamic strain rate vs true strain. c) Deformed Hopkinson test samples at varying strain rates.

 $\begin{array}{l} L_o = 3.1 \ mm \\ D_o = 4.1 \ mm \end{array}$

The strain rate sensitivity of the results, shown in Figure 4.7 a), increases above 10^3s^{-1} similar to literature data for IN718 shown in Figure 2.10. In Figure 4.7 b), the strain hardening rate for the 2770s^{-1} stress-strain at 10% and 15% true strain are slightly greater than the result at $4 \times 10^3 \text{s}^{-1}$. The difference may indicate a greater adiabatic heating effect at 4000s^{-1} . Given the uncertainty in the cause of the oscillation in the data at 6760s^{-1} , the stress-strain result was only shown as a reference and was excluded from evaluation of strain rate sensitivity and constitutive models correlation.

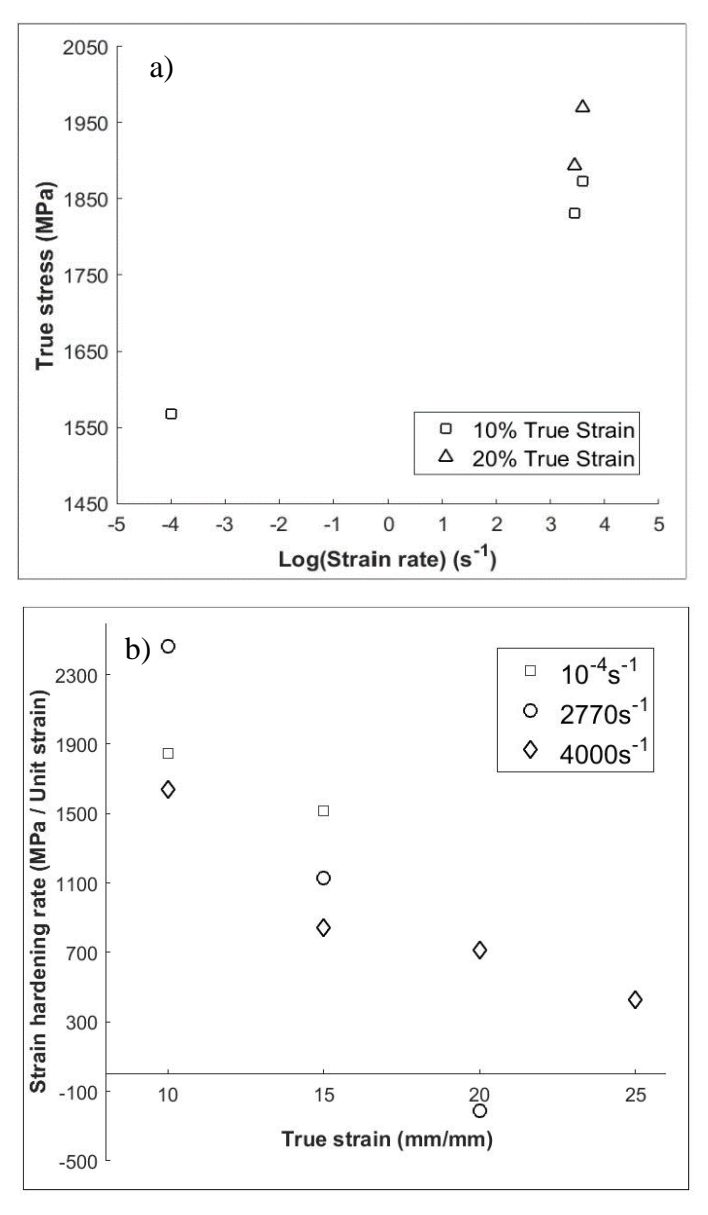


Figure 4.7. Strain rate sensitivity of IN718 at 25°C. a) True stress vs strain rate. b) Strain rate hardening vs true strain.

4.2.2 Temperature Dependence

Specifications for temperature variation SHPB tests for IN718 are summarized in Table 4.4. The target average strain rate was approximately 4000s⁻¹, based on the highest rate attained at 25°C without shear failure. The same initial sample dimension was used for all tests and impact pressure was adjusted accordingly to control the target strain rate. Longitudinal orientated samples were used for the tests.

Table 4.4. Temperature dependent tests of IN718 at a target strain rate of 4000s⁻¹.

Figure	Temperature (°C)	Gas Pressure (PSI)	Avg. Strain Rate (s ⁻¹)	D _o (mm)	L _o (mm)	L _f (mm)	Deformed Sample Strain (%)
	-110	200	4130±70	4.08	3.08	2.12	31.6
4.8	25	190	4000 ± 48	4.07	3.05	2.09	31.4
	500	120	3980±90	4.05	3.04	2.32	24.7

The true stress-strain results are shown in Figure 4.8 a). In the -110°C result, slight variations in the slope of the curve are observed, for example at 10% and 25% true strain, which corresponds to minor oscillations in the transmitted signal. At 500°C, the strain hardening is relatively constant over course of strain and did not exhibit negative strain hardening. The strain rates for the different test temperatures, as shown in Figure 4.8 b), also attain a peak value at 10% true strain and decreases with strain. From the post-deformed samples shown in Figure 4.8 c), strain was generally uniform and barrelling was minimal for the different tests. Also, no shearing effects were observed from the sample surface. The degree of thermal softening, presented in Figure 4.9 a), was relatively constant between the two temperature intervals. The stress-strain results at -110°C and 25°C exhibited similar strain hardening rates as presented in Figure 4.9 b). At 500°C, the strain hardening rate was relatively positive at 10% true strain and became close to zero with increasing strain.

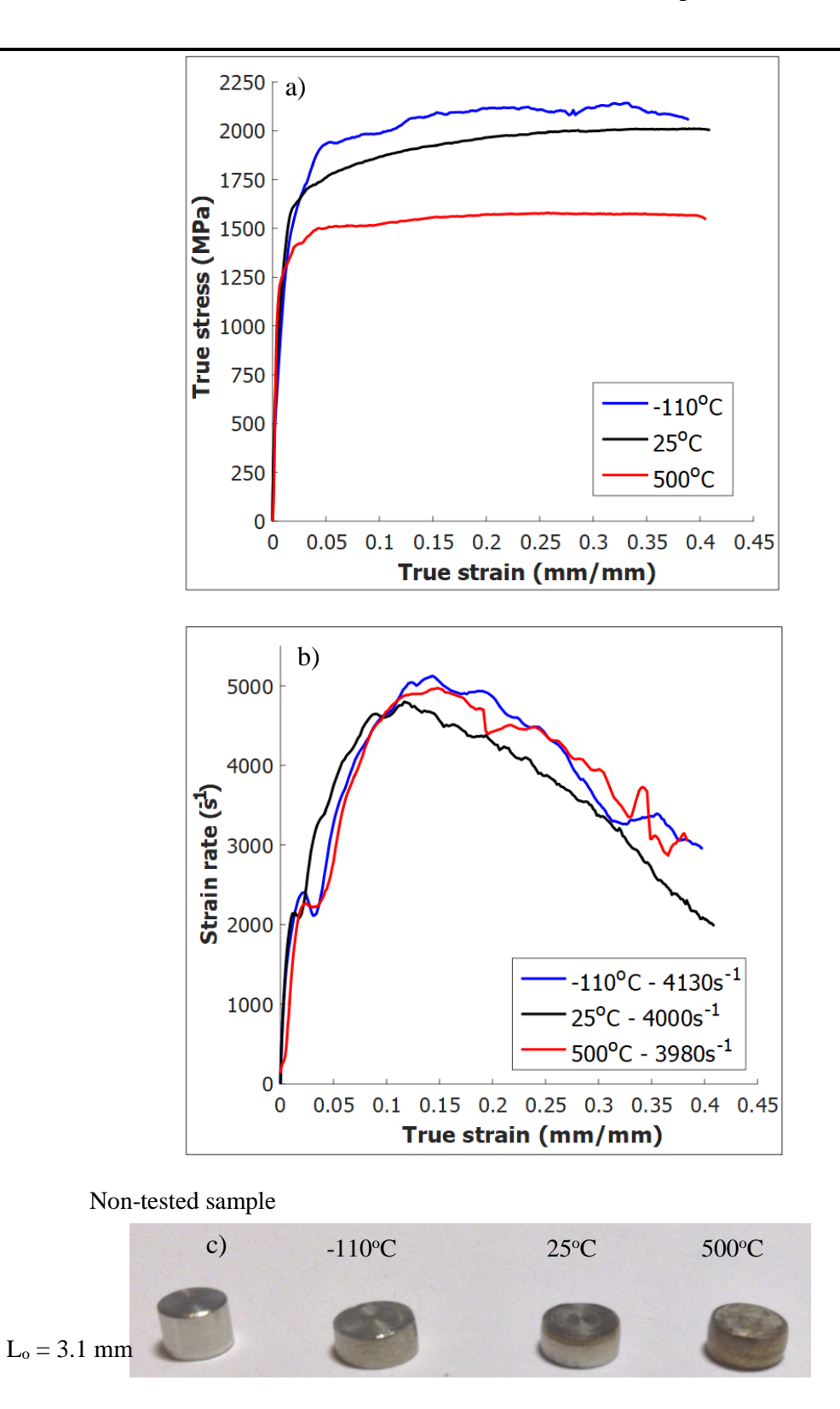
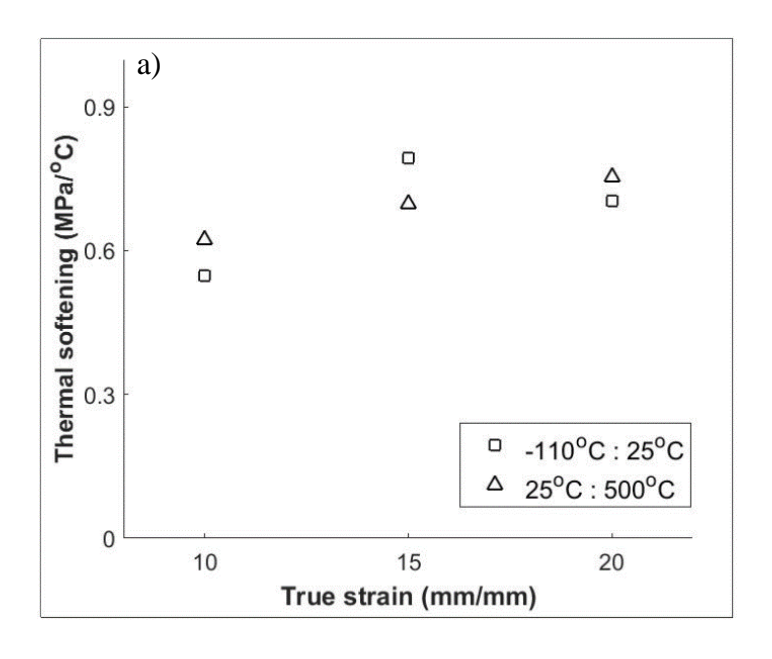


Figure 4.8. Temperature sensitivity results of IN718 at an average strain rate of 4000s⁻¹. a) True stress vs true strain. b) Strain rate vs true strain. c) Deformed samples from varying temperature tests.



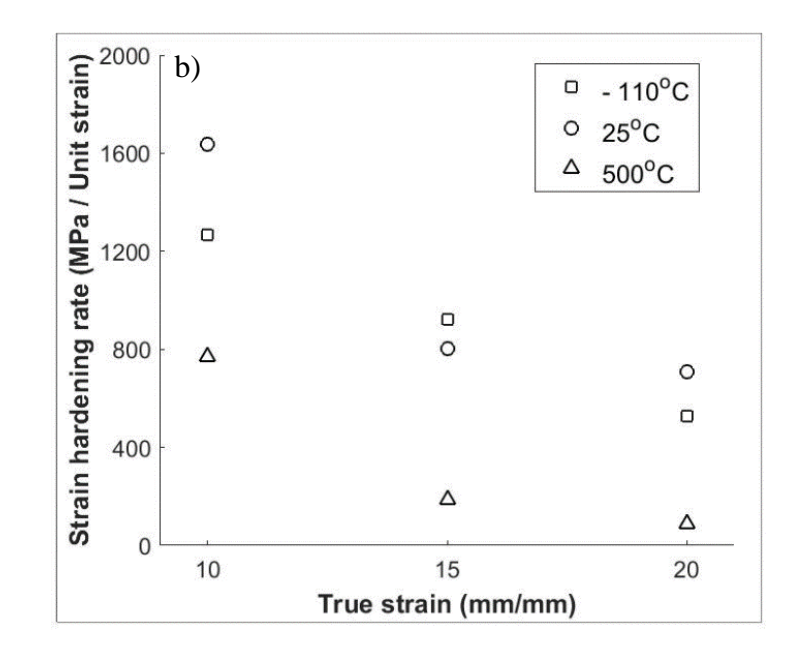


Figure 4.9. Temperature sensitivity of IN718 at an approximate average strain rate of 4000s⁻¹. a) Thermal softening. b) Strain hardening.

4.3 300M Steel

4.3.1 Strain Rate Sensitivity at 25°C

Experimental conditions of dynamic compression tests for 300M steel, longitudinal orientation samples are summarized in Table 4.5. All tests involved sample of reduced dimensions for greater ease of attaining measurable dynamic stress-strain response.

Figure	Gas Pressure (PSI)	Avg. Strain Rate (s ⁻¹)	D _o (mm)	L _o (mm)	L _f (mm)	Deformed Sample Strain (%)
	200	3350±43	4.07	2.94	N/A-Fracture	N/A
4.10		3130±28	4.08	2.86	2.15	24.8
		2960±29	4.08	2.90	2.19	24.5
	180	2450±30	4.08	2.86	N/A-Fracture	N/A

Table 4.5. Dynamic strain rate tests of 300M steel at 25°C.

From the stress-strain results shown in Figure 4.10 a), stress saturation occurs relatively soon past the yield around 5% true strain, followed by softening with increasing strain. The strain hardening trend at dynamic strain rates is comparable to BCC-type microstructure such as Tungsten and Aermet 100 steel, where stress saturation occurs soon after yield [115]. The test measured at an average strain rate of 3350s⁻¹ consisted of a lower final strain than tests at 2960s⁻¹ and 3130s⁻¹ due to shear failure in the sample. The lower strain rate test of 2450s⁻¹ also resulted in shear failure of the sample. For the quasi-static result, the negative strain hardening is likely due to the mode of loading being in tension rather than compression. Quasi-static compression stress-strain results, for example in 4340 steel shown in Figures 2.13 and 2.15, display positive strain hardening comparable to the results obtained by Hopkinson compression. The measured strain rate profiles, shown in Figure 4.10 b), attained a peak value around 10% true strain and did not maintain a constant plateau. In the strain rate sensitivity plot in Figure 4.11 a), the stress levels closely overlap for all dynamic strain rate results. In Figure 4.11 b), the data at 2450s⁻¹ exhibits a high positive strain hardening value at 10% true strain. The value maybe an outlier due to oscillations between 5% and 10% true strain in the stress-strain result. The quasi-static result was not used for comparison given the mode of loading being in tension.

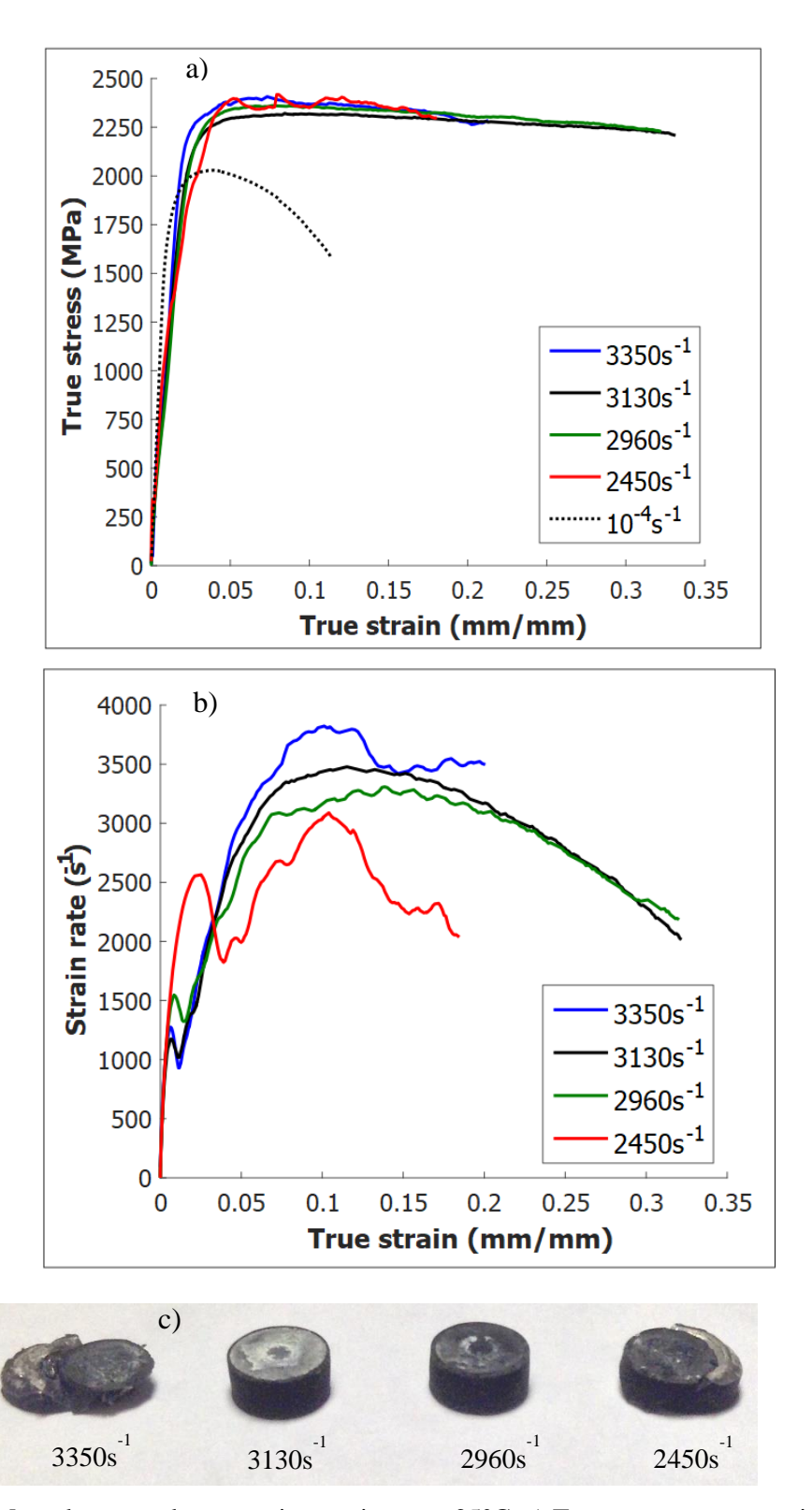


Figure 4.10. 300M steel test results at varying strain rates, 25° C. a) True stress vs true strain. b) True strain vs strain rate. c) Deformed samples from tests at 25° C.

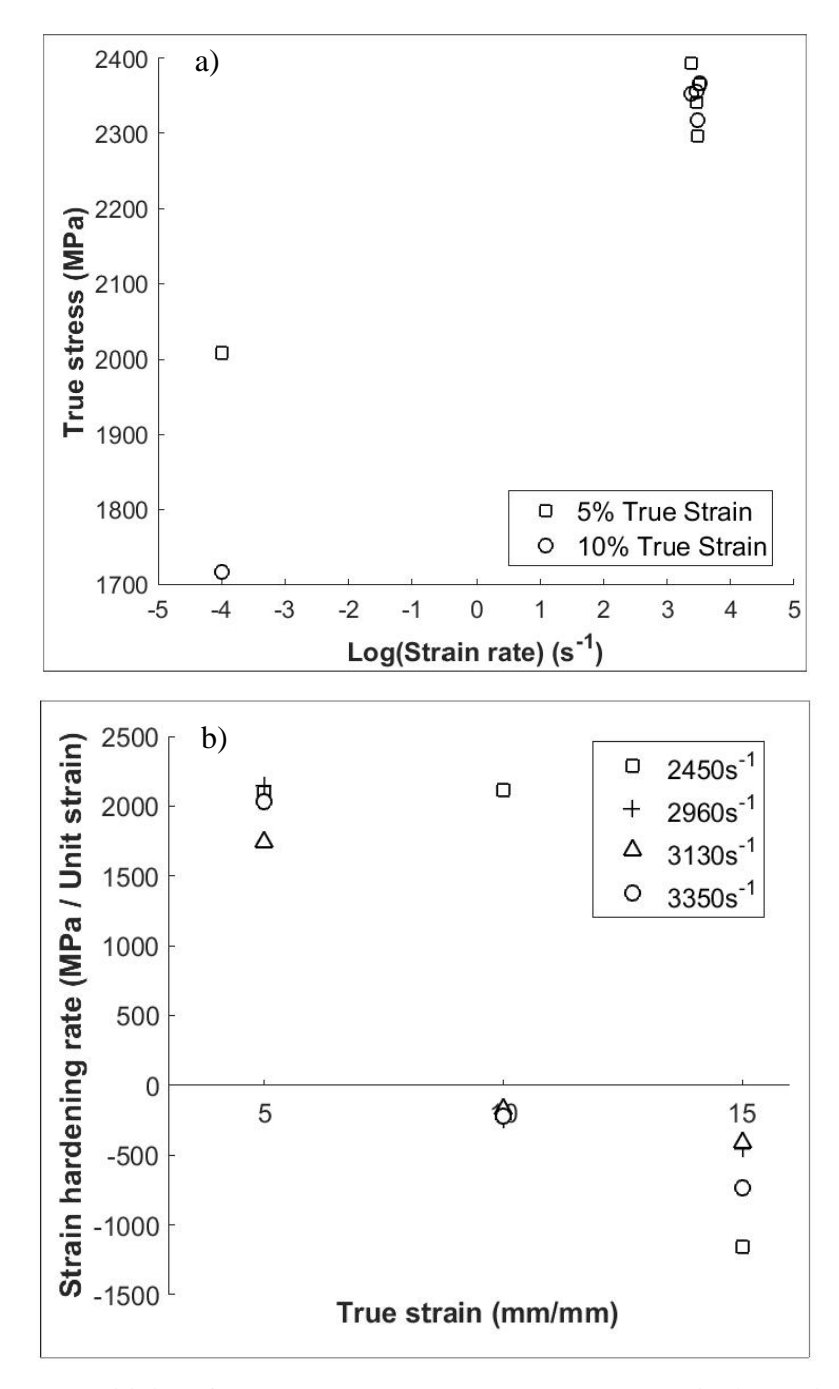


Figure 4.11. Strain rate sensitivity of 300M at 25°C. a) True stress vs true strain. b) Strain rate hardening vs true strain.

4.3.2 Temperature Dependence

Temperature sensitivity tests for 300M steel, as summarized in Table 4.6, involved the same initial sample dimensions as tests at 25°C. The target average strain rate was about 2400s⁻¹, the lower range where shear failure was exhibited at 25°C.

Table 4.6. Temperature	dependent tests	s of 300M steel at a	target strain ra	te of 2400s ⁻¹ .

Figure	Temperature (°C)	Gas pressure (PSI)	Avg. Strain Rate (s ⁻¹)	D _o (mm)	L_{o} (mm)	$L_{f}\left(mm\right)$
	-70	190	2350±11	4.06	3.06	
4.10	25	180	2450±30	4.08	2.86	N/A- Fracture
4.12	200	110	2300±20	4.08	3.04	
	500	80	2550±35	4.06	3.02	

True strain-strain results of longitudinal orientated samples are presented in Figure 4.12. The stress-strain result at -70°C appears to attain more positive strain hardening than the test at 25°C, and the increase in stress occurred by a parallel shift. The stress-strain results at 200°C and 500°C by comparison, do not decrease by a shift with the same strain hardening slope as expected. Instead, the stress-strain curves show an initial positive rise to peak level after which saturation occurs. Due in part to the strain hardening variation at 200°C, the temperature dependence of thermal softening and strain hardening rate, presented in Figure 4.13, do not exhibit a clear correlation. Although the target strain rate was lowered, shear and fracture failure occurred in each test at the different impact pressures. Sample failures may have contributed in an unsteady strain rate evaluated from the recorded reflected signal. From the temperature variation results and tests at 25°C, 300M steel appears to have a low tolerance to shear failure. The low strain levels may reflect a low capacity for defect accumulation, leading to saturation of strain hardening response and shear localization effects [116].

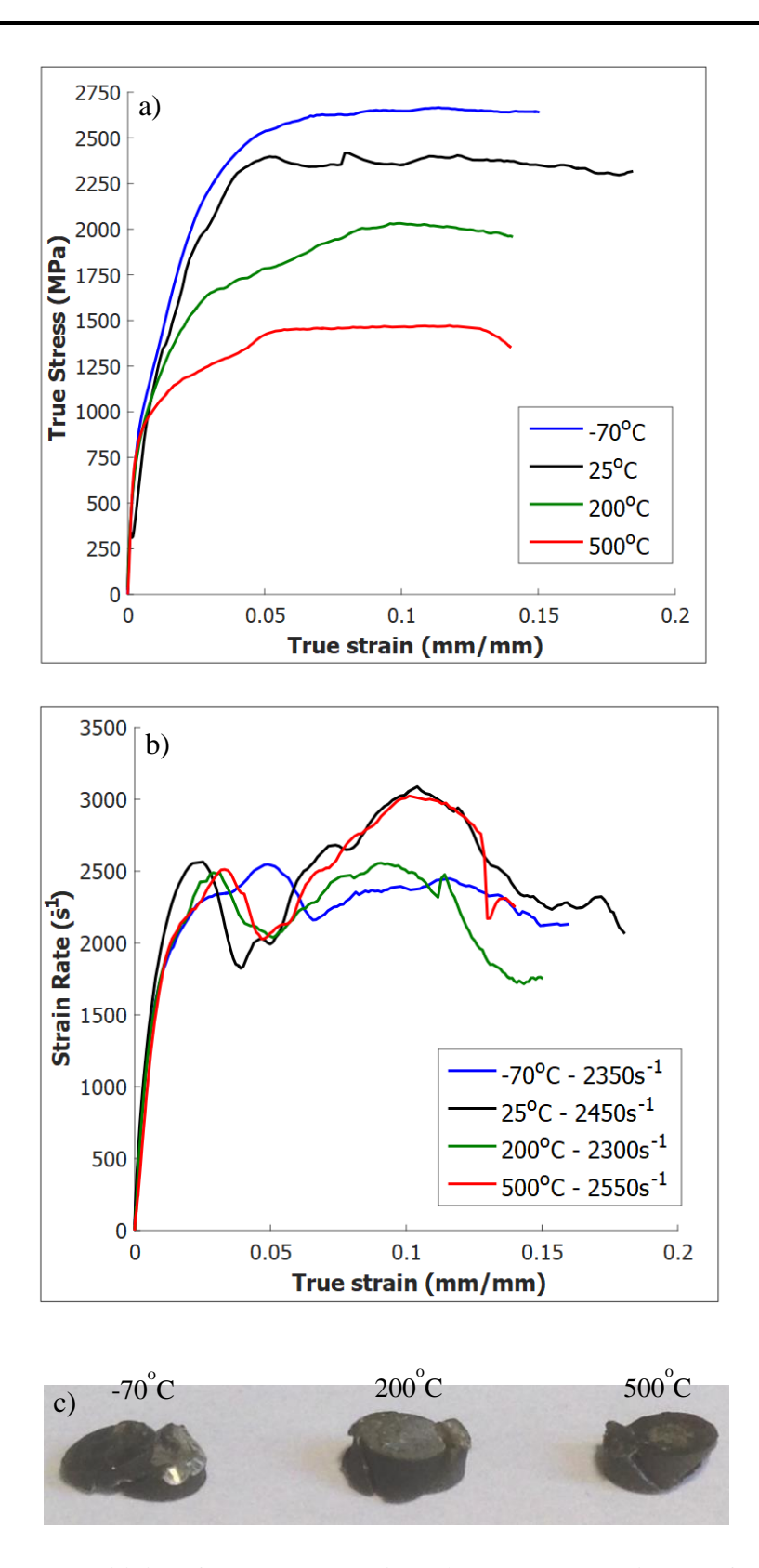


Figure 4.12. Temperature sensitivity of 300M at approximately an average strain rate of 2450s⁻¹. a) True stress vs true strain. b) Strain rate vs true strain. c) Deformed samples from varying temperature tests.

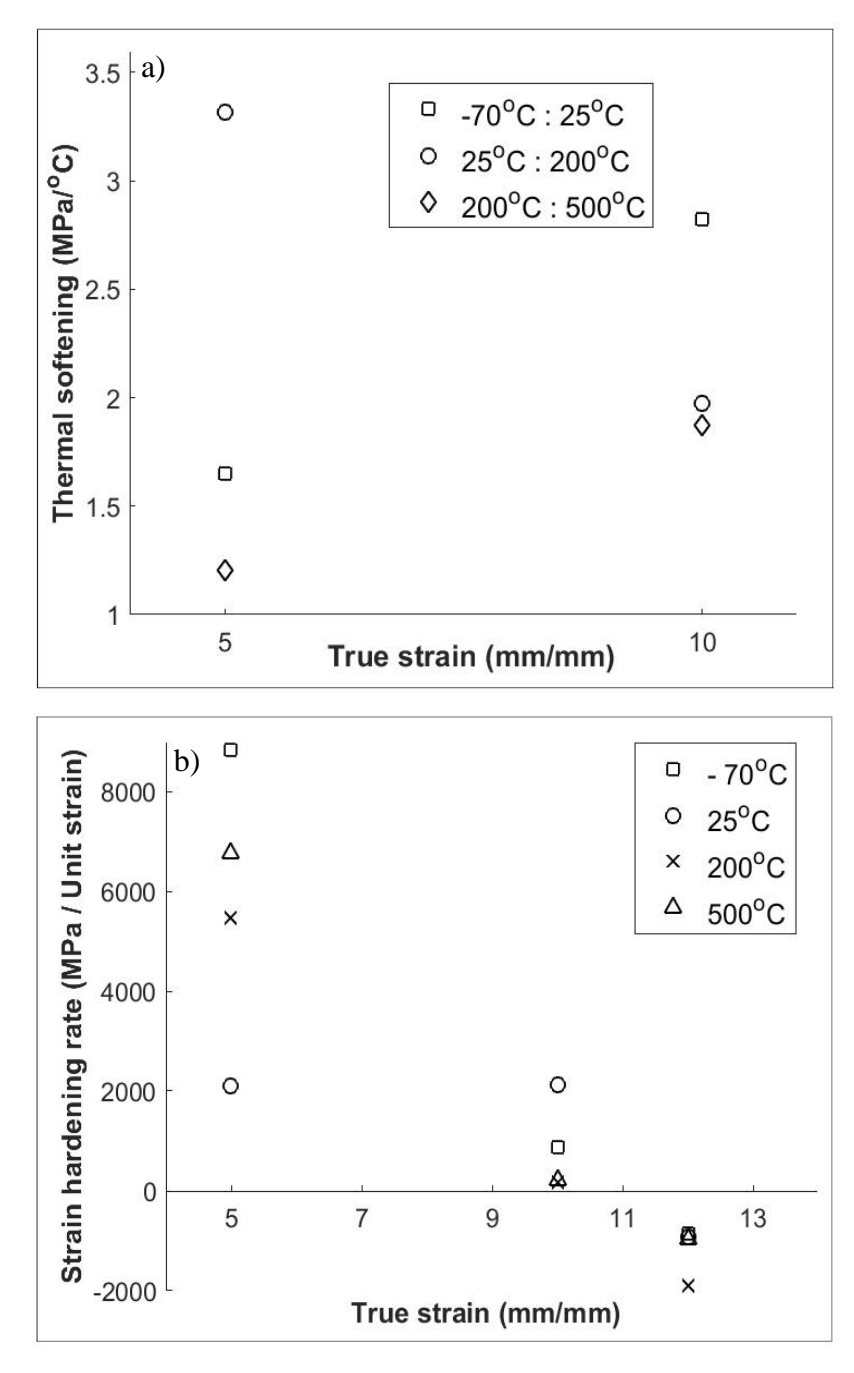


Figure 4.13. Temperature sensitivity of 300M steel at an average strain rate of 2400s⁻¹. a) Thermal softening vs true strain. b) Strain rate hardening vs true strain.

Chapter 5 Constitutive Model Evaluation

5.1 AA7050-T7451

5.1.1 Johnson Cook Model

In applying the least square fitting method, the elastic region of each stress-strain data was subtracted from the plastic stress-strain region. The temperature-dependent elastic modulus (E) values used are listed in Table 5.1. Elastic modulus at -110°C was extrapolated using a second order polynomial fitting of the reference data presented. The boundary values for the initial guess are shown in Table 5.2. To account for the cooling test result as the reference condition, the reference temperature and strain rate are -110°C and 1950s⁻¹, respectively. The fitted stress in comparison with experiments are presented in Figure 5.1.

Table 5.1. Elastic modulus value of AA7050-T7451 at different temperatures [63].

	-110°C	25°C	100°C	200°C
Elastic	80	70.7	63	57
Modulus (GPa)				

Table 5.2. Boundary values for the least squares evaluation of Johnson Cook model correlation to AA7050-T7451 experiments.

Parameters	A	В	n	С	m
Lower bound	430	380	0.1	0.005	1
Upper bound	470	480	0.5	0.01	1.5

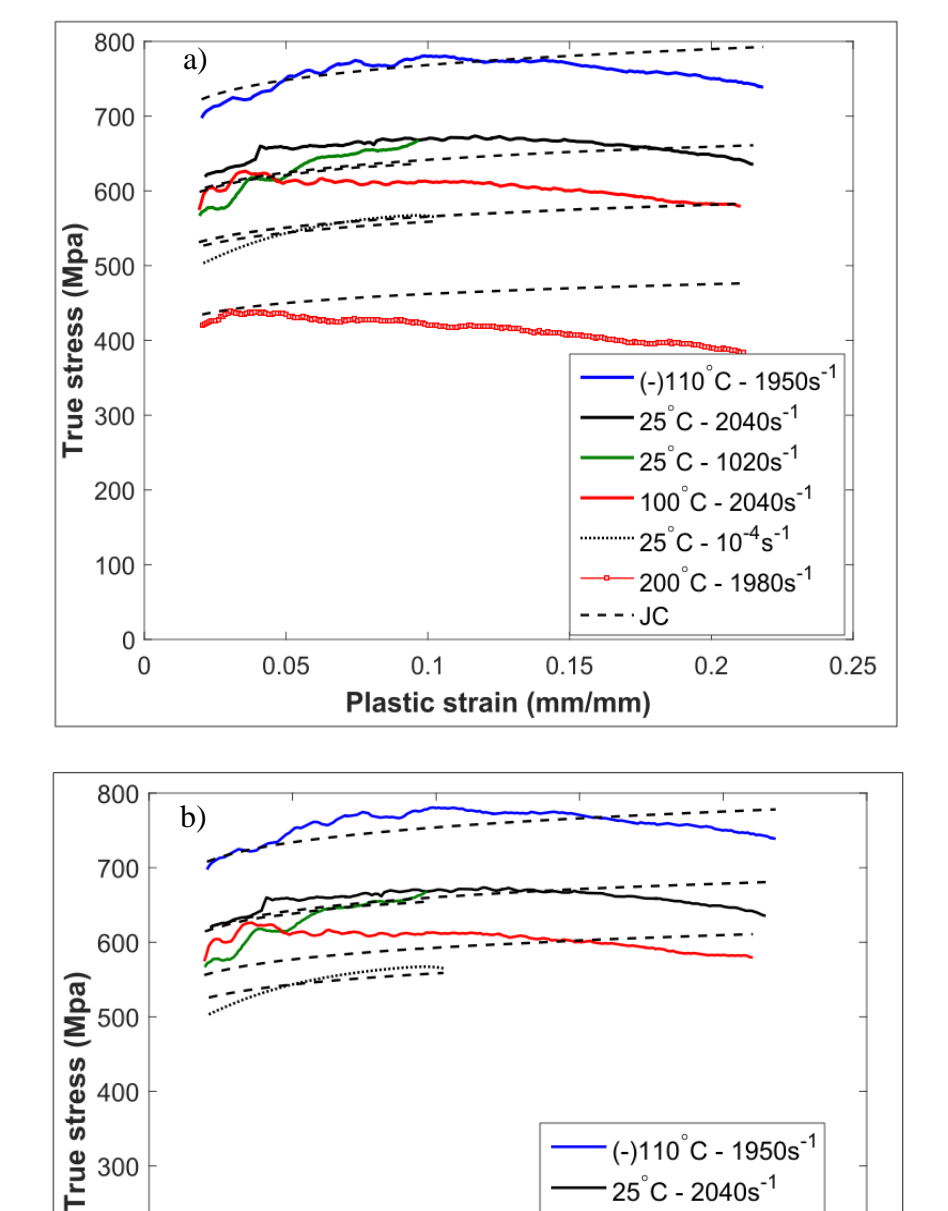


Figure 5.1. Comparison of AA7050-T7451 experiment data to Johnson Cook model fitting. a) Including data at 200°C. b) Excluding data at 200°C.

0.1

Plastic strain (mm/mm)

25°C - 2040s⁻¹ 25°C - 1020s⁻¹

100°C - 2040s⁻¹ "25°C - 10⁻⁴s⁻¹

0.2

0.25

- - JC

0.15

300

200

100

0

0

0.05

The closeness of fit values of the comparisons in Figure 5.1 are summarized in Tables 5.3 and 5.4. A negative R² value indicate poor correlation, which is the lowest for the elevated temperature data given that the experimental and predicted stress have the opposite trend. Correlations for experiments at -110°C, and 25°C, 2040s⁻¹ also have low R² values because of the fitting over regions of softening. A positive R² value closer to 1 and a lower mean square error indicates a better correlation. An evaluation without the result at 200°C was also performed given that thermal softening increased non-linearly at the temperature due to possible microstructural changes. The aim of the study was to set experimental conditions such that no significant microstructural changes due to recrystallization, or phase dissolution arises, which could render stress-strain responses complex, and difficult to correlate using the empirical constitutive models. The Johnson Cook correlations for most experimental conditions improved by excluding the 200°C data. For comparability, the evaluation of other empirical models also uses the least squares method and excludes the results at 200°C.

Table 5.3. Closeness-of-fit values for Johnson Cook model correlation to AA7050-T7451 experiments.

Data set	-110°C – 1950s ⁻¹	25°C – 2040s ⁻¹	25°C – 1020s ⁻¹	100°C – 2040s ⁻¹	25°C – 10 ⁻⁴ s ⁻¹	200°C – 1980s ⁻¹
Mean square	441	506	381	1954	99	2767
error						
\mathbb{R}^2	-0.32	-2.04	0.56	-13.2	0.72	-11.4

Table 5.4. Closeness-of-fit values for Johnson Cook model correlation to AA7050-T7451 experiments excluding 200°C data.

Data set	-110°C– 1950s ⁻¹	$25^{\circ}\text{C} - 2040\text{s}^{-1}$	25°C – 1020s ⁻¹	$100^{\circ}\text{C} - 2040\text{s}^{-1}$	$25^{\circ}\text{C} - 10^{-4}\text{s}^{-1}$
Mean square	329	268	473	665	96
error					
\mathbb{R}^2	0.01	-0.61	0.45	-3.82	0.73

A comparison of constitutive parameters determined from the least squares procedure and literature reference values are shown in Table 5.5. The least squares fitting in this work results in a lower strain hardening parameter (*n*). The main reason is that the fitting procedure accounts for a wider range of strain where stress saturation and strain softening occurs. In the study presented by Tan et al. [96], the experimental data applied in evaluation of Johnson Cook parameters consisted of positive strain hardening over the measured strain. Also, the study did not involve varying temperature tests. Reference values reported by Wang et al. [117] were obtained using an inverse analysis method, and thus the results are not directly comparable to the conventional procedure of evaluating constitutive models from high strain rate experiments.

Table 5.5. Johnson Cook model parameters obtained and literature values for Aluminum 7050- T7451.

Parameters	A	В	n	С	m
This work	467	380	0.1	0.0077	1.06
This Work (excluding 200°C data)	451	380	0.1	0.0092	1.22
Tan et al. [96]	490	530	0.58	0.0051	-
Wang et al. [117]	489	167	0.32	0.0032	2.32

5.1.2 Johnson Cook - Adiabatic Heating Model

The correlation between experimental data and the Johnson Cook and adiabatic temperature rise model (equation 2.11) evaluated by least squares fitting is presented in Figure 5.2. The temperature rise term is evaluated based on 90% conversion of rate of plastic work to heat. The density value is 2830 (kg/m³) and temperature-dependent heat capacities are shown in Table 5.6. By accounting for temperature rise in each dynamic strain rate result, the fitted stress improved correlations to the stress saturation and strain softening trends in the -110°C and 25°C results. The fit was also improved for the 100°C results when compared to that obtained using the Johnson Cook model, as indicated by lower mean square error and R² values. Fitted result for the stress-strain data at 1020s⁻¹ remains the same.

Table 5.6. Heat capacity of AA7050-T7451 at different temperatures [63].

	-110°C	25°C	100°C	200°C
Heat capacity	710	856	904	1004
$(J \cdot kg^{-1} \cdot {}^{\circ}C^{-1})$				

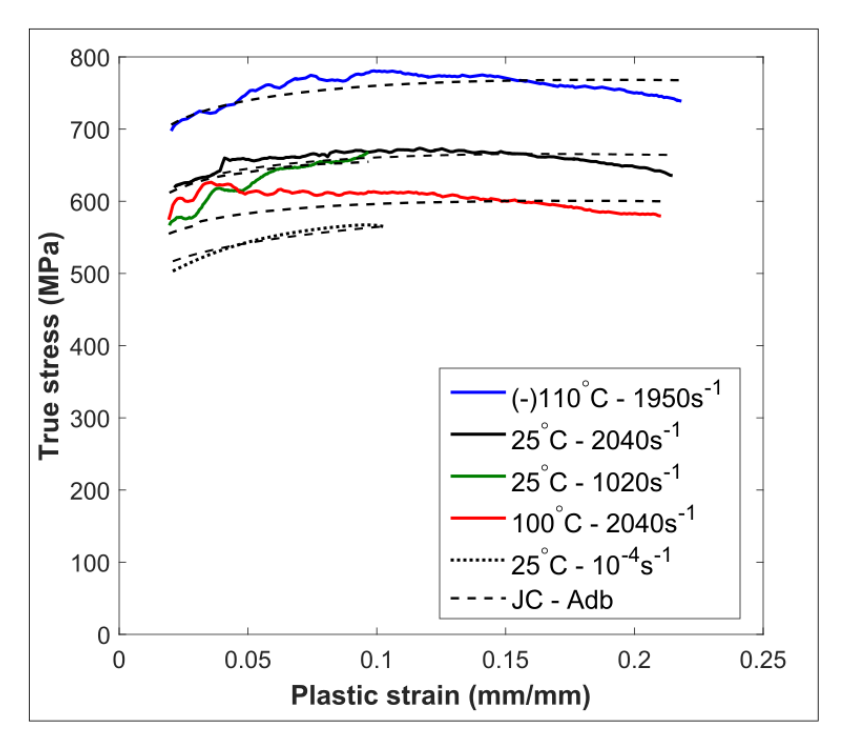


Figure 5.2 Comparison of fitted stress using Johnson Cook – Adiabatic heating model to experiments for AA7050-T7451.

Table 5.7. Boundary value and parameters obtained for Johnson Cook – Adiabatic heating model correlation to AA7050-T7451 experiments.

Parameters	A	В	n	С	m
Lower bound	430	400	0.1	0.005	1
Upper bound	470	480	0.57	0.02	1.5
Solution	430	468	0.13	0.01	1.23

Table 5.8. Closeness-of-fit values for Johnson Cook – Adiabatic heating model correlation to AA7050-T7451 experiments.

Data set	-110°C- 1950s ⁻¹	$25^{\circ}C - 2040s^{-1}$	$25^{\circ}C - 1020s^{-1}$	$100^{\circ}\text{C} - 2040\text{s}^{-1}$	$25^{\circ}C - 10^{-4}s^{-1}$
Mean square	171	110	476	470	33
error					
\mathbb{R}^2	0.48	0.34	0.45	-2.40	0.91

5.1.3 Johnson Cook - Voce Strain Hardening Model

The comparison of experimental data and fitting with the Johnson Cook - Voce strain hardening model (equation 2.10) is shown in Figure 5.3. The reference temperature and strain rate are -110°C and 1950s⁻¹, as in the previous least squares procedure. The Voce strain hardening law, as in the case of the adiabatic heating model, enabled a closer prediction of stress saturation. In comparison to the Johnson Cook models, correlations are improved for stress-strain results attained at 1020s⁻¹, -110°C and 25°C. Correlations for tests at 25°C and 100°C, 2000s⁻¹ are the same.

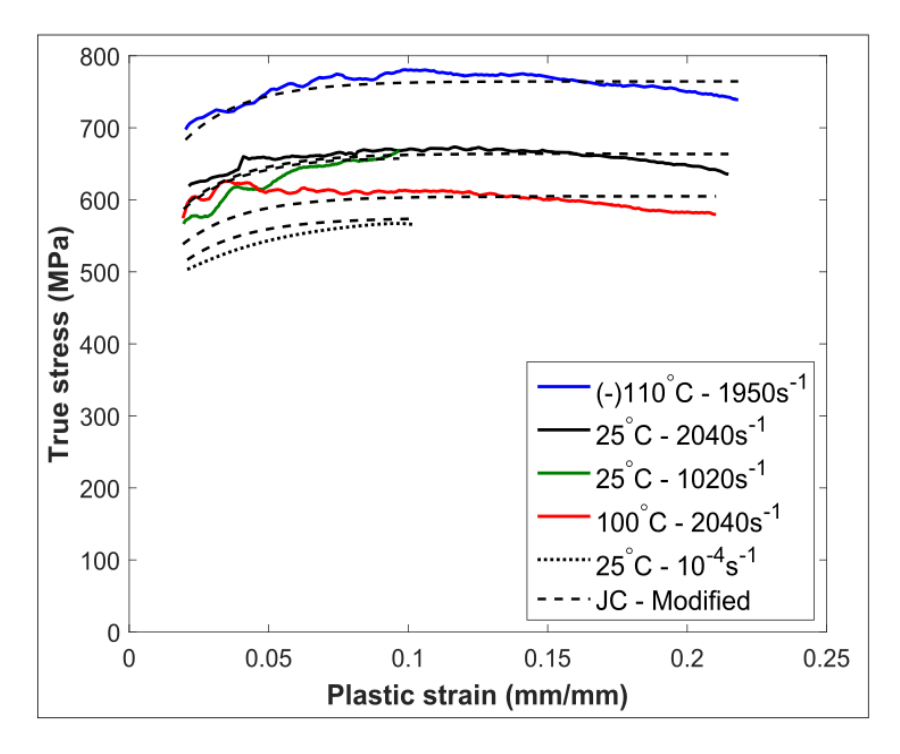


Figure 5.3. Comparison of fitted stress using Johnson Cook – Voce strain hardening model to experiments for AA7050-T7451.

Table 5.9. Boundary values and parameters obtained for Johnson Cook – Voce strain hardening model correlation to AA7050-T7451 experiments.

Parameters	A	В	С	D	Е	m
Lower bound	400	100	20	0.005	5*10-4	0.5
Upper bound	600	400	45	0.01	10-3	1
Solution	565	200	45	0.008	10-3	0.7

Table 5.10. Closeness-of-fit values for Johnson Cook – Voce strain hardening model correlation to AA7050-T7451 experiments.

Data set	-110°C- 1950s ⁻¹	$25^{\circ}C - 2040s^{-1}$	$25^{\circ}\text{C} - 1020\text{s}^{-1}$	100°C – 2040s ⁻¹	$25^{\circ}\text{C} - 10^{-4}\text{s}^{-1}$
Mean square	123	116	257	470	178
error					
\mathbb{R}^2	0.63	0.31	0.70	-2.40	0.5

5.1.4 Modified KHL Model

The comparison of fitted stress with modified KHL model and experimental data is shown in Figure 5.4. The modified KHL model improves the correlations to the reference result at -110°C, and conditions at 2040s⁻¹, 25°C and 100°C compared to the Johnson Cook model.

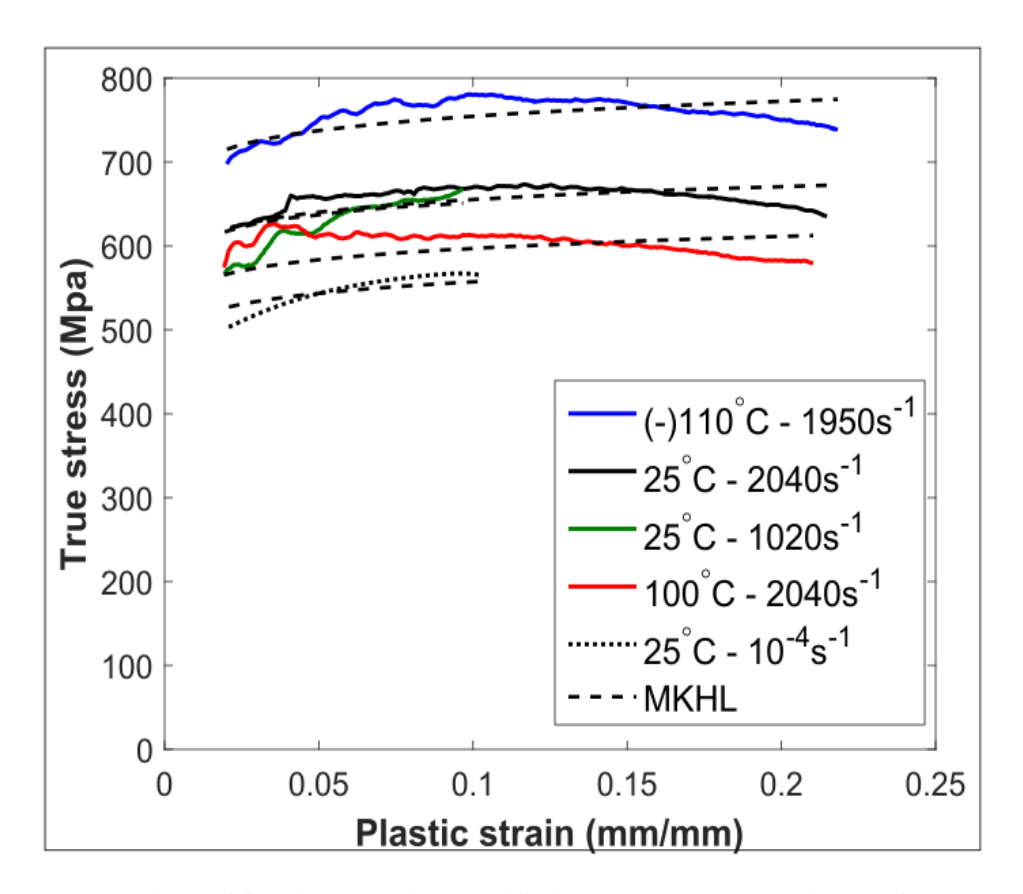


Figure 5.4. Comparison of fitted stress using modified KHL model to experiments for AA7050-T7451.

Table 5.11. Boundary values and parameters obtained for modified KHL model correlation to AA7050-T7451 experiments.

Parameters	A	В	С	D	E	m
Lower bound	400	400	0.1	0.05	0.01	0.5
Upper bound	440	420	0.2	0.1	0.03	1.3
Solution	440	411	0.1	0.08	0.013	0.70

Table 5.12. Closeness-of-fit values for modified KHL model correlation to AA7050-T7451 experiments.

Data set	-110°C– 1950s ⁻¹	$25^{\circ}\text{C} - 2040\text{s}^{-1}$	$25^{\circ}\text{C} - 1020\text{s}^{-1}$	$100^{\circ}\text{C} - 2040\text{s}^{-1}$	$25^{\circ}\text{C} - 10^{-4}\text{s}^{-1}$
Mean square	285	217	501	503	111
error					
\mathbb{R}^2	0.14	-0.30	0.42	-2.64	0.69

A comparison of the overall mean square error and R² values of each model correlation to all experimental data is presented in Table 5.13. The Johnson Cook modified strain hardening model provides a relatively better fit overall based on the mean square error values compared. For the R² value of the entire data set, the total sum of squares (TSS) is the same in all cases. The ratio of the residual sum of squares (RSS) to the TSS are of relatively low values. The R² values thus do not vary significantly and provides less indication of the overall closeness of fit between the models and experiment.

Table 5.13. Summary of mean square error and R^2 values for model correlations to AA7050-T7451 experiments.

Constitutive Model	Johnson Cook	JC – Adiabatic Heating	JC – Voce Strain Hardening	Modified KHL model
Mean square error	393	264	235	343
R ²	0.93	0.95	0.96	0.94

5.2 IN718

For least square evaluations, the temperature-dependent modulus values used to subtract the elastic region from the plastic stress are listed in Table 5.14. The value at -110°C was extrapolated from the higher temperature trends.

Table 5.14. Elastic modulus of IN718 at different temperatures [118].

	-110°C	25°C	500°C
Elastic Modulus (GPa)	210	200	175

5.2.1 Johnson Cook Model

The Johnson Cook model fitting for the IN718 experimental results is presented in Figure 5.5. The melting temperature was defined as 1300°C [104], with reference temperature and strain rate as -110°C and 4130s⁻¹, respectively. The fitted model stress is comparable to experiments at 4000s⁻¹, -110°C and 25°C in terms of the strain hardening rate, although do not correlate well to the magnitude of the stress. The fitted stress between tests at 25°C, 2770s⁻¹ and 4000s⁻¹ were close together, as the difference between the experimental strain rates is small.

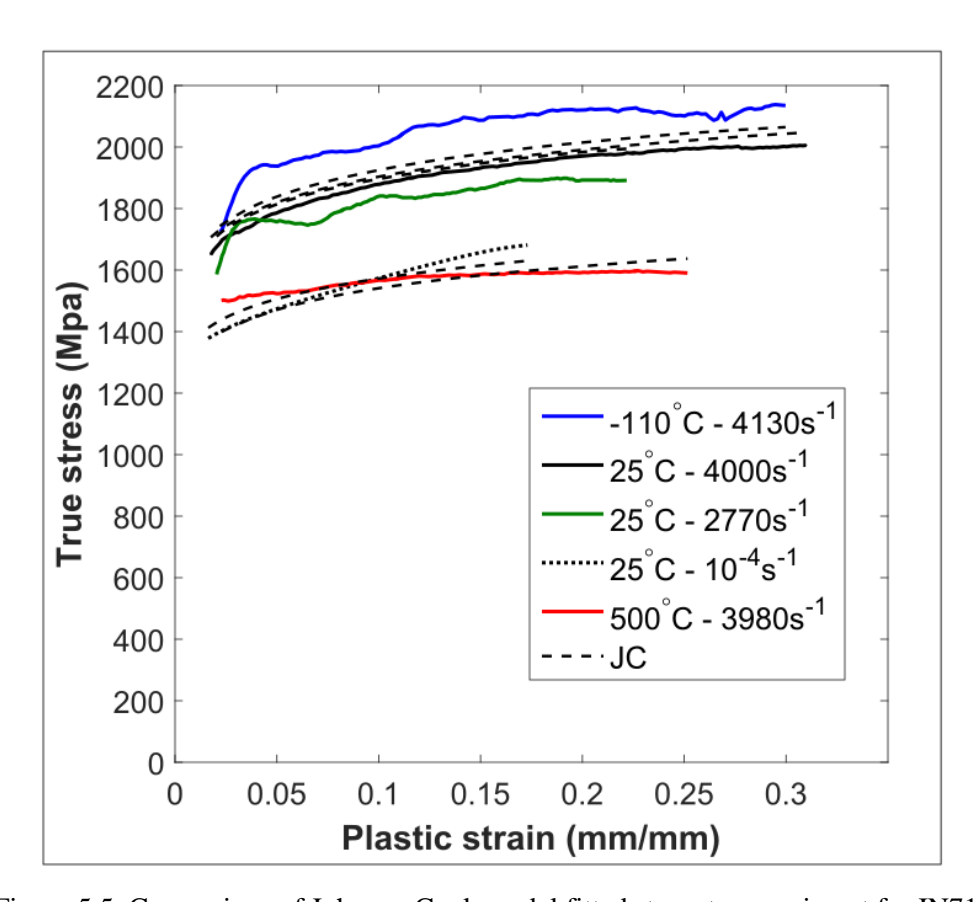


Figure 5.5. Comparison of Johnson Cook model fitted stress to experiment for IN718.

Table 5.15. Boundary values and parameters obtained for Johnson Cook model correlation to IN718 experiments.

Parameters	A	В	n	С	m
Lower bound	1100	1000	0.1	0.01	1
Upper bound	1300	1300	0.5	0.02	2
Solution	1100	1162	0.15	0.001	1.92

Table 5.16. Closeness-of-fit values for Johnson Cook model correlation to IN718 experiments.

Data set	-110°C – 4130s ⁻¹	$25^{\circ}\text{C} - 4000\text{s}^{-1}$	$25^{\circ}C - 2770s^{-1}$	25°C -10 ⁻⁴ s ⁻¹	$500^{\circ}\text{C} - 3980\text{s}^{-1}$
Mean square	8453	936	5870	930	1831
error					
\mathbb{R}^2	0.32	0.89	-0.152	0.875	-0.80

In comparison to literature values on aging treated and precipitation hardened IN718 alloys presented in Table 5.17, the strain hardening parameters (A, B) are within comparable ranges, whereas parameters (n), (m) are notably different. The differences among the reported studies include the experimental procedures and conditions used to evaluate the model constants. Several studies for example use a quasi-static test result at 25°C as the reference strain rate and temperature conditions. In this study, the varying temperature tests were obtained at an average strain rate of $4000s^{-1}$. The thermal softening parameter (m) evaluated for instance, maybe different depending on the strain rate of the temperature sensitivity tests, as strain rate and temperature effects are coupled.

Kobayashi et al. [104] for example in evaluating Johnson Cook model parameters from results shown in Figure 2.20, included temperature rise to account for adiabatic heating and strain softening effects. A handbook value for the softening parameter (m = 1.03) was used to match the fitted model to the stress-strain curve. The strain hardening value reported (n = 0.164), however, was close to the value obtained in this study, possibly due to accounting for experimental stress saturation and softening effects. Pereira et al. [119] reported strain hardening

value (n = 0.652) from quasi-static tensile results. The Johnson Cook model, however, was unable to predict the Hopkinson result at $2000s^{-1}$ and 25° C, due to a decrease in the experimental strain hardening rate under dynamic compression. The same issues were discussed by Demange et al. [49] for experiments shown in Figure 2.11. Johansson and Persson [114] applied least squares fitting to experimental data directly, although did not discuss the closeness of fit to the different strain rate and temperature results. In addition to differences in evaluation procedures, experimental condition, intrinsic material behavior differences due to processing conditions, and final microstructural properties influence the data for model calibration.

Table 5.17. Johnson Cook model parameters obtained and literature values for IN718.

Parameters	A	В	n	С	m
This work	1100	1162	0.15	0.001	1.92
Liuktus [69]	1142	1329	0.396	0.0038	N/A
Demange et al. [49]	1290	895	0.53	0.016	1.55
Pereira et al. [119]	1350	1139	0.652	0.0134	N/A
Kobayashi et al. [104]	980	1370	0.164	0.02	1.03
Wang et al. [70]	963	967	0.33	Variable	1.3
Johansson and Persson [114]	1350	1375	0.58	0.0074	1.20
Canaveral [120]	1067	1129	0.416	0.014	1.71

5.2.2 Modified KHL Model

The modified KHL model (equation 2.12) correlation to IN718 data is shown in Figure 5.6. Input boundary values for parameters (*A*) and (*B*) are initially estimated as the same as in the Johnson Cook model, as they denote yield strength and strain hardening. An estimation for other value parameters are based on reference data and parameters for Titanium 6-4 alloys [121], the closest material comparison to IN718 in literature for which the model was applied. When compared to Johnson Cook model fitting results, the modified KHL model mainly improved correlations to the magnitude of peak stress for experiments at 25°C and -110°C at 4130s⁻¹, as indicated by the lower residual errors and higher R² values. The predicted strain hardening trends are qualitatively similar for both models. The modified KHL model stress also overestimates the strength at 2770s⁻¹, and the fitted stress between 2770s⁻¹ and 4000s⁻¹ at 25°C are not distinguishable.

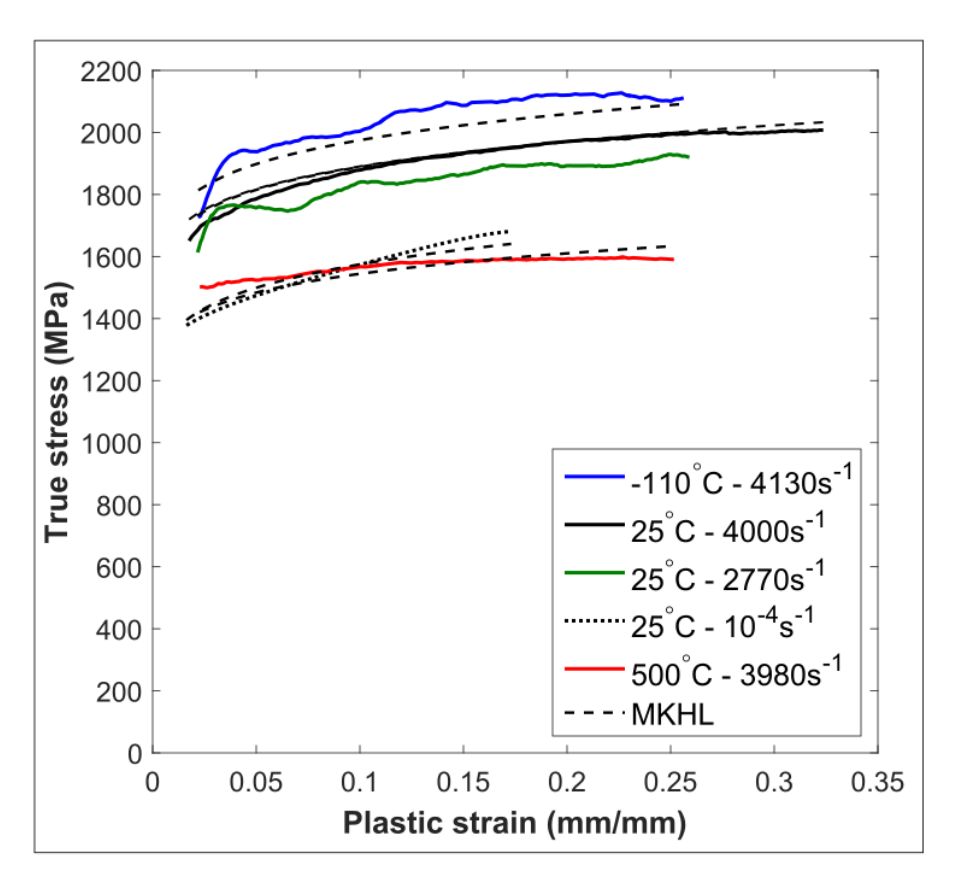


Figure 5.6. Comparison of modified KHL model fitting to experiment for IN718.

Table 5.18. Boundary values and parameters obtained for modified KHL model correlation to IN718 experiments.

Parameters	A	В	\mathbf{n}_1	n _o	С	m
Lower bound	1100	1000	0.15	0.1	0.01	0.4
Upper bound	1300	1300	0.5	0.5	0.03	0.8
Solution	1300	1219	0.19	0.18	0.016	0.42

Table 5.19. Closeness-of-fit values for modified KHL model correlation to IN718 experiments.

Data set	-110°C - 4130s ⁻¹	25°C – 4000s ⁻¹	$25^{\circ}\text{C} - 2770\text{s}^{-1}$	25°C -10 ⁻⁴ s ⁻¹	$500^{\circ}\text{C} - 3980\text{s}^{-1}$
Mean square	3229	175	3526	491	1526
error					
\mathbb{R}^2	0.66	0.98	0.31	0.93	-0.50

The modified KHL model results provided a lower mean square error value for all data sets as shown in Table 5.20. The main feature of the modified KHL model is accounting for a decreasing strain hardening rate with increasing strain rate. The experimental stress-strain of IN718 shown in Figure 4.7 consist of a slight decrease in strain hardening rate under dynamic compression at 25°C, however, not to the same extent as reported for Titanium 6-4 shown in Figure 2.21. Also, the modified KHL model consists of a power law strain rate form instead of the logarithm form, and a modified temperature term that differs from the Johnson Cook model. The main improvement of model correlations was for experimental results at -110°C and 25°C at 4000s⁻¹ rate of strain, which possibly indicate that the temperature definition in the model better accounts for temperature sensitivity compared to the Johnson Cook model.

Table 5.20. Mean square error and R² values for model correlations to IN718 experiments.

Constitutive Model	Johnson Cook	Modified KHL model
Mean square error	3366	1651
\mathbb{R}^2	0.92	0.96

5.3 300M Steel

For constitutive model correlation, the experimental data obtained at 2960s⁻¹ and 25°C is applied for fitting instead of the test at 2450s⁻¹ due to the stress-strain response being steadier as shown in Figure 4.10. The estimates of the modulus at -70°C and 500°C are based on low temperature data reported for a 300 Maraging steel [122] with a similar modulus value to 300M of about 205 GPa at 25°C [123]. Correlations were evaluated by using the least squares method.

-70°C 25°C 500°C

Elastic Modulus 200 197 160

Table 5.21. Elastic modulus of 300M steel at various temperatures.

5.3.1 Johnson Cook Model

(GPa)

Constitutive fitting of 300M steel data with Johnson Cook model is shown in Figure 5.7. For the evaluation, the melting temperature was defined as 1500°C [124], and the reference temperature and strain rate were -70°C and 2350s⁻¹, respectively. Most parameters were obtained between the boundary values defined. Changing the upper boundary value (*B*) did not further lower the overall mean square error for all correlations. The R² value was moderately positive for the result at 200°C, although the mean squares error is the highest since the model does not account for the change in strain hardening. A lower mean square error provides a better indicator of closeness of fit to each experimental data set.

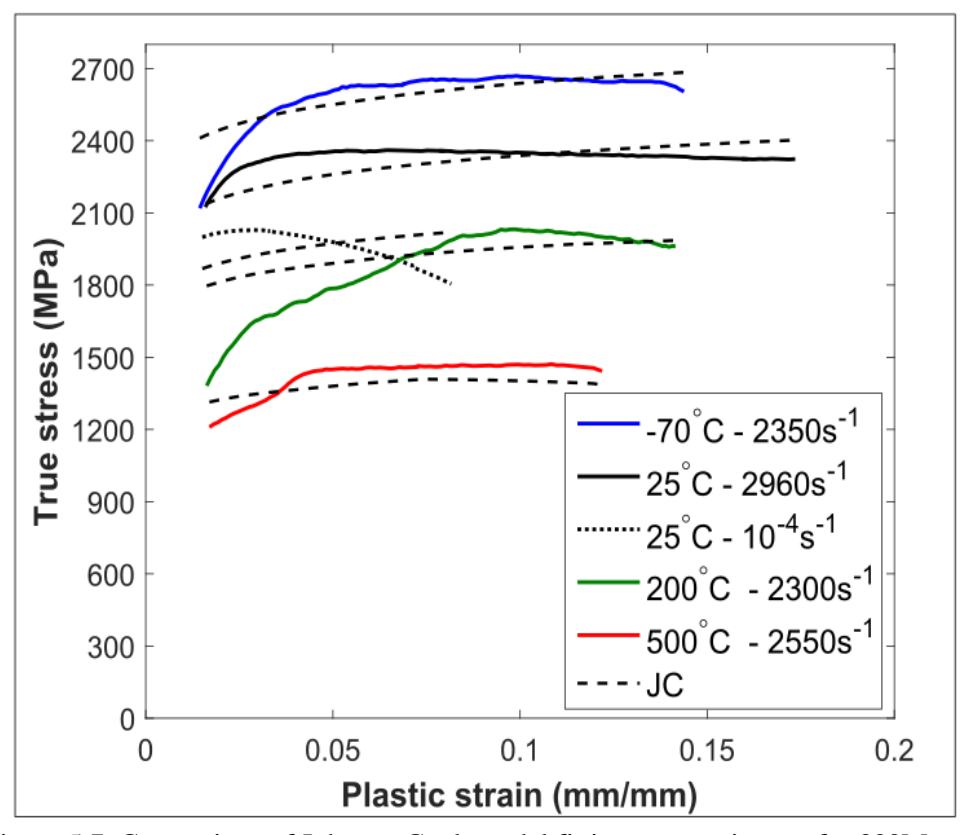


Figure 5.7. Comparison of Johnson Cook model fitting to experiments for 300M steel.

Table 5.22. Boundary values and parameters obtained for Johnson Cook model correlation to 300M experiments.

Parameters	A	В	n	С	m
Lower bound	1200	1100	0.05	0.005	0.5
Upper bound	1400	1600	0.2	0.01	1
Solution	1373	1600	0.10	0.007	0.77

Table 5.23. Closeness-of-fit values for Johnson Cook model correlation to 300M experiments.

Data set	$-70^{\circ}\text{C} - 2350\text{s}^{-1}$	25°C – 2960s ⁻¹	25°C -10 ⁻⁴ s ⁻¹	200°C – 2300s ⁻¹	500°C - 2550s ⁻¹
Mean square	4732	4726	11012	14623	3127
error					
\mathbb{R}^2	0.67	-1.46	-1.57	0.44	0.42

The Johnson Cook parameters are compared with similar reference results and materials are shown in Table 5.24. The Johnson Cook parameters reported by Lin et al. [125] involved a 300M steel of a similar composition and Rockwell hardness to the alloy in this work. The Hopkinson bar tests conditions in the study also consisted of similar strain rates and elevated temperatures as in this work. However, the experimental stress-strain results and data utilized for fitting to the Johnson Cook model were not presented. Only the Johnson Cook parameters were provided. The study by Lach et al. [126] involved a 300 Maraging grade steel that has a different composition than 300M steel. The stress-strain response presented, however, had comparable stress values and strain hardening properties at 25°C as the 300M in this work. The stress-strain curves exhibited a relatively constant plateau without dynamic recovery effects, and thermal softening at higher temperatures occurred by parallel shift of the plastic stress. Thus, the strain hardening (n) and thermal softening (m) parameters are relatively close in magnitude as the values obtained in this work.

Table 5.24. Johnson Cook model parameters obtained and literature values for 300M and 300 Maraging steel.

Parameters	A	В	n	С	m
This work	1373	1600	0.10	0.007	0.77
Lin et al. [125]	1293	1008	0.04	0.014	1.73
Lach et al. [126]	850	1300	0.09	0.022	0.87
Canaveral [120]	1542	1531	0.33	0.0036	1.19

5.3.2 Johnson Cook – Cowper Symonds Model

The correlation to experiments using the Johnson Cook – Cowper Symonds model (equation 2.9) is shown in Figure 5.8. Qualitatively, the predicted strain hardening and strength levels are close to the Johnson Cook model. The degree of model correlation to the dynamic compression data results however, were lower compared to the Johnson Cook model.

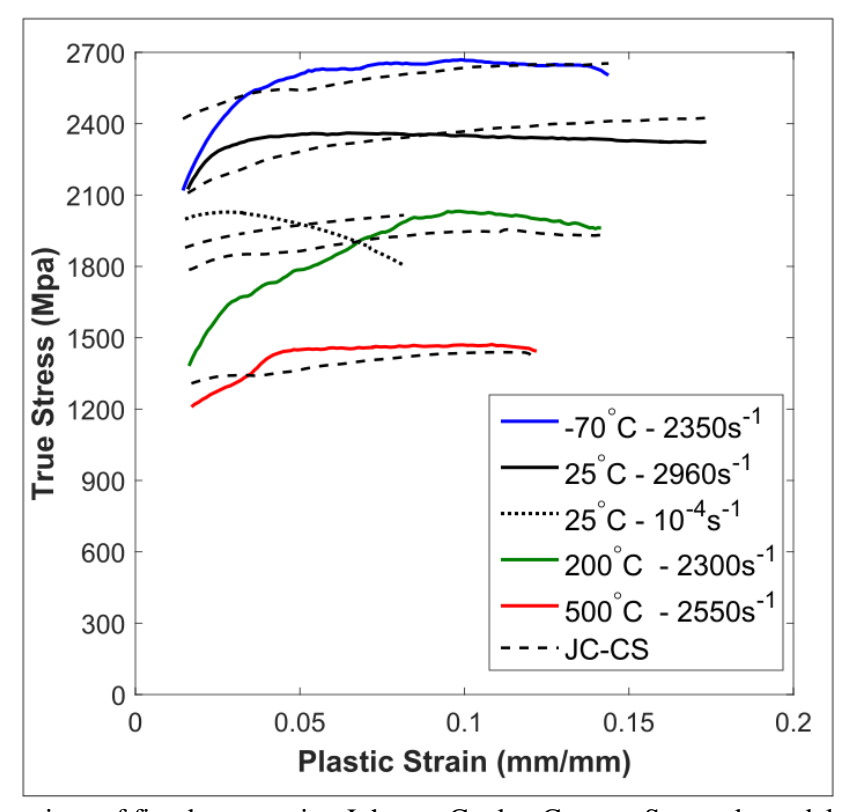


Figure 5.8. Comparison of fitted stress using Johnson Cook – Cowper-Symonds model to experiments for 300M steel.

Table 5.25. Boundary values and parameters obtained for the Johnson Cook – Cowper Symonds model correlation to 300M experiments.

Parameters	A	В	n	D	p	m
Lower bound	1200	1100	0.05	60000	1	0.5
Upper bound	1500	1500	0.2	90000	2.5	1
Solution	1200	1365	0.09	90000	1.85	0.76

Table 5.26. Closeness-of-fit values for Johnson Cook – Cowper Symonds model correlations to 300M experiments.

Data set	$-70^{\circ}\text{C} - 2350\text{s}^{-1}$	25°C – 2960s ⁻¹	25°C -10 ⁻⁴ s ⁻¹	200°C - 2300s ⁻¹	500°C - 2550s ⁻¹
Mean square	5195	4930	10044	14864	3168
error					
\mathbb{R}^2	0.63	-1.57	-1.34	0.44	0.41

5.3.3 Johnson Cook – Voce Strain Hardening Model

The fitted stress using the Johnson Cook -Voce strain hardening model and experimental results is presented in Figure 5.9. In comparison to the Johnson Cook model, the modified model mainly improved correlations for the data at 25°C, 2960s⁻¹ strain rate. The correlation to the result at -70°C was better as well. However, the closeness of fit was of a lower degree than the Johnson Cook and J-C Cowper Symond models for the elevated temperature stress-strain results.

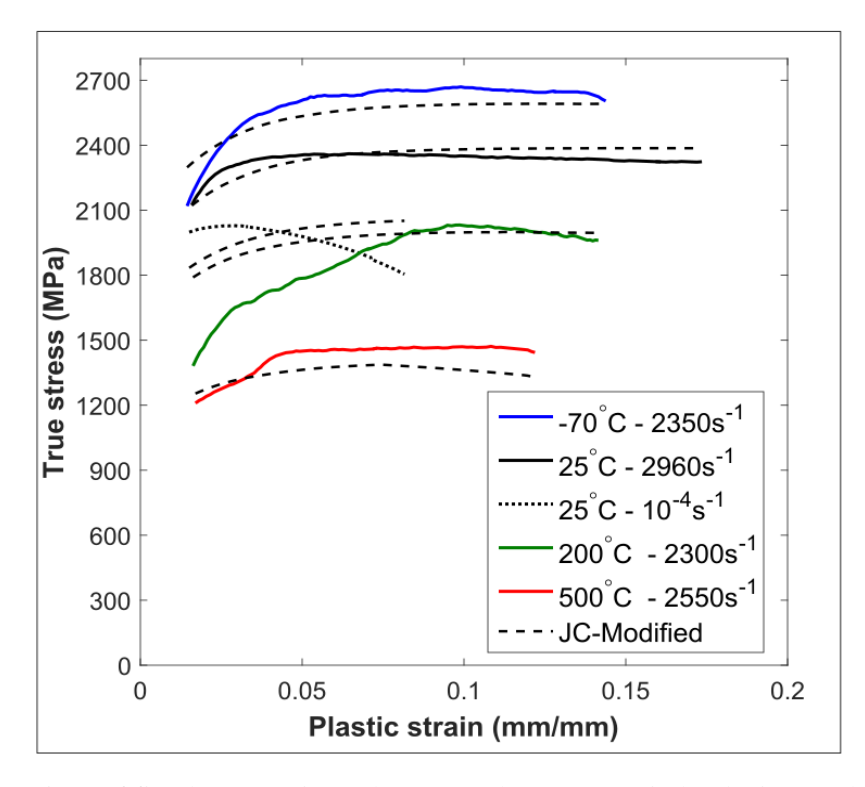


Figure 5.9. Comparison of fitted stress using Johnson Cook - Voce strain hardening model to experiments for 300M steel.

Table 5.27. Boundary values and parameters obtained for Johnson Cook – Voce strain hardening model correlations to 300M experiments.

Parameters	A	В	С	D	Е	m
Lower bound	1600	400	40	0.001	10-4	1
Upper bound	2200	600	60	0.01	10-3	2
Solution	2000	594	48	0.0079	10-4	1.37

Table 5.28. Closeness-of-fit values for Johnson Cook – Voce strain hardening model correlations to 300M experiments.

Data set	$-70^{\circ}\text{C} - 2350\text{s}^{-1}$	$25^{\circ}\text{C} - 2960\text{s}^{-1}$	$25^{\circ}\text{C} - 10^{-4}\text{s}^{-1}$	$200^{\circ}\text{C} - 2300\text{s}^{-1}$	$500^{\circ}\text{C} - 2550\text{s}^{-1}$
Mean square	4158	2257	8227	19661	4824
error					
\mathbb{R}^2	0.69	0.065	-2.35	0.23	-0.05

The overall correlation to all experiments were relatively close for the three models as presented in Table 5.29. The J-C Cowper Symonds model consists of the lowest mean square error overall although essentially provides the same correlation results as the Johnson Cook model. The Johnson Cook Voce strain hardening model, even though accounting for stress saturation, consisted of a lower degree of correlation to the experiments by comparison.

Table 5.29. Summary of mean square error and R² values for model correlations to 300M experiments.

Constitutive Model	Johnson Cook	Johnson Cook – Cowper Symonds	JC – Voce Strain Hardening
Mean square error	8047	8023	9655
\mathbb{R}^2	0.95	0.95	0.94

5.4 Constitutive Model Stress-Strain at 25°C

The constitutive models and parameters determined from the sections above are applied to estimate the stress-strain at strain rates higher than experimentally attainable values. For each material, the extrapolated strain rate is up to $10^5 \mathrm{s}^{-1}$, within the typical estimated range for peening-induced plastic strain response [1]. The representative measured temperature in the predicted stress is defined as $25^{\circ}\mathrm{C}$, the condition at which shot peening is conventionally carried out. The reference temperature in the model is the sub-zero temperature applied in the experiments. Although adiabatic heating arises at high strain rates, the temperature change is excluded from the extrapolation given the stress-strain values used to calculate temperature is also an estimation itself. The predicted constitutive stress-strain at several lower strain rates are plotted for reference. In addition, the equivalent strain rate of the cooling temperature result at $25^{\circ}\mathrm{C}$ determined using the constitutive model fitting are presented.

5.4.1 AA7050-T7451

In using the Johnson Cook model in Figure 5.10 a), the extrapolated stress-strain increases by constant intervals, as the Johnson Cook model has a linear function to the logarithm of the normalized strain rate. Also, the predicted strain hardening is positive with increasing strain, which deviates from experimental observations. The extrapolated stress-strain with the Johnson Cook - Voce hardening model is presented in Figure 5.10 b). The model provided a better overall correlation to SHPB experiments compared to the J-C model as presented in the summary Table 5.13. The predicted stress consists of a higher initial strain hardening rate and stress saturation due to the Voce strain hardening form. The predicted stress increases non-linearly above 10^4s^{-1} due to contributions from the strain rate term, $\exp(\text{E} \times \frac{\hat{\epsilon}}{\hat{\epsilon}_{\text{ref}}})$, in addition to the initial strain rate factor D × $\ln(\frac{\hat{\epsilon}}{\hat{\epsilon}_{\text{ref}}})$. The dependence of increase in strain rate sensitivity on values of constants (*D*) and (*E*) has been shown in the study by Shin and Kim [101].

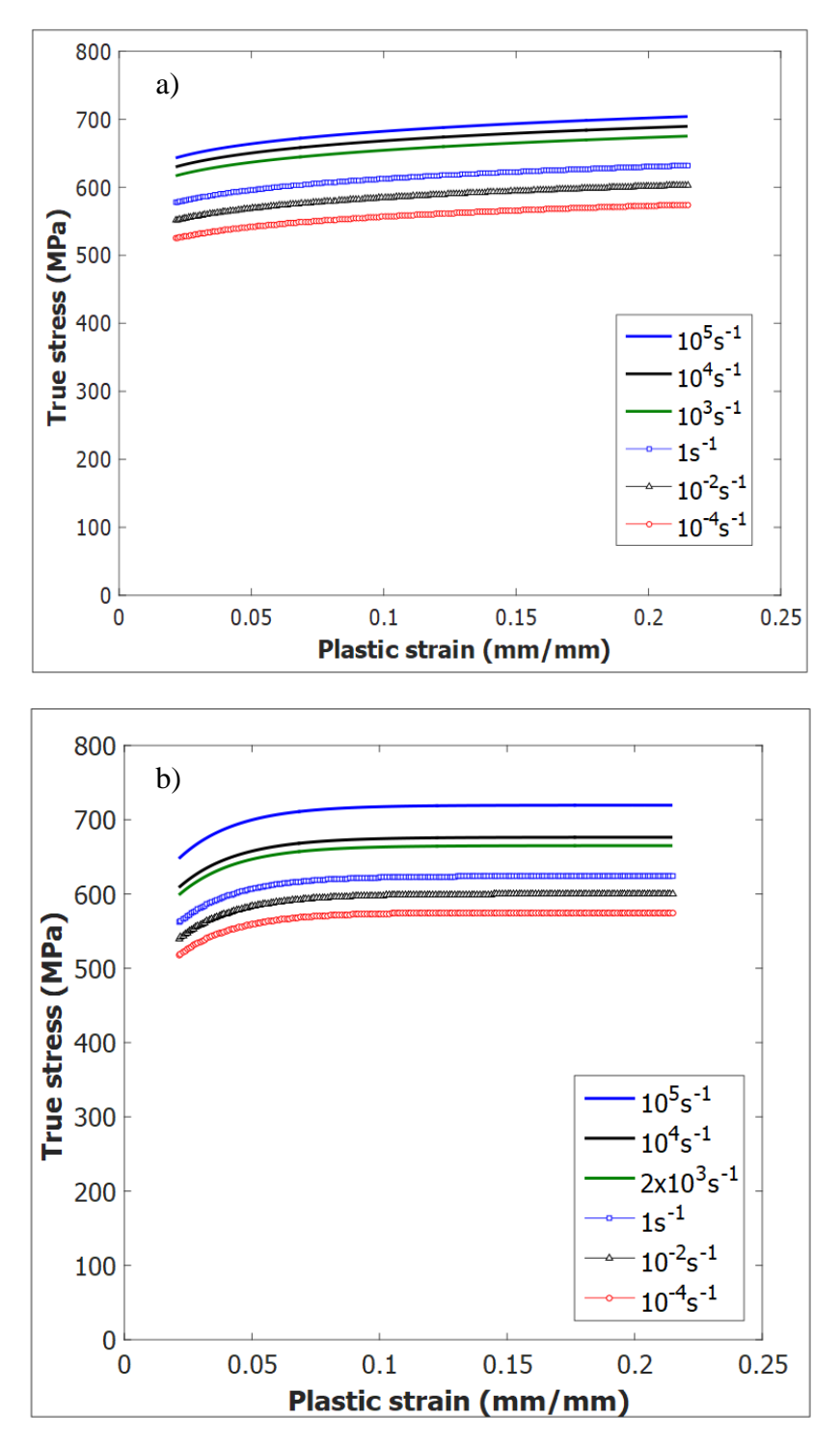


Figure 5.10. Constitutive model stress-strain extrapolated at varying strain rates and 25°C for Aluminum 7050-T7451. a) Johnson Cook model. b) Johnson Cook—Voce strain hardening model.

The average measured true stress and extrapolated stress between 0.02 to 0.2 strain are presented in Table 5.30. The measured average stress between $2\times10^3\text{s}^{-1}$ and $2.75\times10^3\text{s}^{-1}$ at 25°C were relatively close. In the work presented by Chen et al. [67] for Aluminum 7050-T7451, the peak stress at 0.1 true strain, $2\times10^3\text{s}^{-1}$ and 10^4s^{-1} was 610 MPa and 633 MPa, respectively. Similarly, in the reference shown in Figure 2.7, the strain rate sensitivity at 25°C was not apparent between 10^3s^{-1} to $6.2\times10^3\text{s}^{-1}$. The extrapolated stress with the Johnson Cook or modified Johnson Cook models could be a reasonable estimate up to 10^4s^{-1} .

From literature results on compressive high strain rate tests of other 7000 series Aluminum alloys, Mocko et al. [127] reported an average stress of 1300 MPa for Aluminum 7075-T6 measured at $3\times10^4 \mathrm{s}^{-1}$ using a modified SHPB, direct impact bar test. The average stress using conventional SHPB measured at $2\times10^3 \mathrm{s}^{-1}$ and $4.5\times10^3 \mathrm{s}^{-1}$ was about 700 MPa and 750 MPa, respectively. Labeas et al. [128] presented SHPB stress-strain results for Aluminum alloy 7449-T7651, that exhibited an increase in strength from approximately 650 MPa to 800 MPa at strain rates of $2.5\times10^3 \mathrm{s}^{-1}$ and $8\times10^3 \mathrm{s}^{-1}$, respectively. The 7075-T6 and 7449-T7651 alloys from the reference results are comparatively more rate sensitive than AA7050-T7451 from $10^3 \mathrm{s}^{-1}$ to $10^4 \mathrm{s}^{-1}$. Given an increase in strength of the similar alloys can occur across a wide range of dynamic strain rates, AA7050-T7451 may also exhibit an increase in strength from $10^4 \mathrm{s}^{-1}$ and above. The predicted stress using the Johnson Cook Voce strain hardening model may be representative of a transition in rate sensitivity at higher strain rates.

Table 5.30. Average measured stress and extrapolated stress at 25°C for AA7050-T7451.

Avg. Stress (MPa)	$10^3 s^{-1}$	$2 \times 10^{3} \text{s}^{-1}$	$2.75 \times 10^{3} \text{s}^{-1}$	$10^4 s^{-1}$	$10^{5} s^{-1}$
Experiment – 25°C	617±2.9	641±1.9	647±2.1	-	-
Extrapolated Stress – J-C Model	-	659±1.1	-	668±1.2	683±1.2
Extrapolated Stress – J-C Voce Model	-	656±1.1	-	667±1.1	710±1.2

The Johnson Cook - Voce strain hardening model was used to estimate the equivalent strain rate at 25°C for the experimental stress-strain at -110°C and 1980s⁻¹. In the evaluation, the temperature value of the model was set to 25°C, and the strain rate variable was the equivalent strain rate. Model parameters were the same values as shown in row 2 in Table 5.5. The fitting was evaluated using least squares fitting in Matlab and a comparison is shown in Figure 5.11. The strain rate obtained and closeness-of-fit values are summarized in Table 5.31. Between about 0.02 to 0.2 plastic strain, the average stress of the test at -110°C was 759 \pm 1.3 MPa and the average extrapolated stress was 760 \pm 1.3 MPa. The equivalent strain rate of the cooling test at 25°C, evaluated using the J-C Voce strain hardening model, is within the typical strain rate range observed in peening.

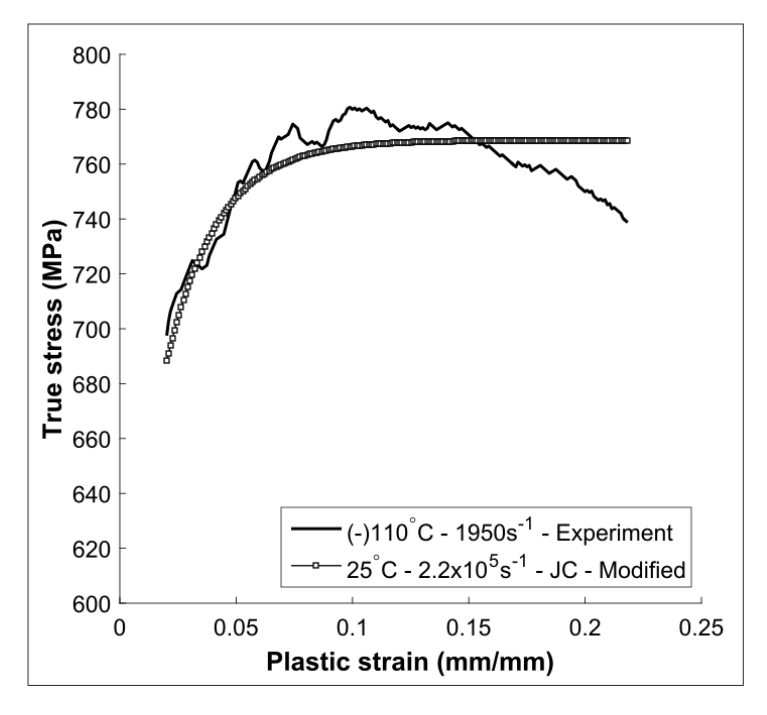


Figure 5.11. Measured stress-strain at -110°C and 1950s⁻¹ compared to the fitted stress at 25°C and a higher strain rate using the J-C– Voce strain hardening model for Aluminum 7050-T7451.

Table 5.31. Equivalent strain rate of cooling test at 25°C and closeness of fit values for AA7050-T7451.

Upper Bound	Lower Bound	Solution	Mean square error	\mathbb{R}^2
$10^4 s^{-1}$	$10^{5} \mathrm{s}^{-1}$	2.2×10 ⁵ s ⁻¹	117	0.65

5.4.2 IN718

The extrapolated stress-strain using the Johnson Cook model for IN718 is shown in Figure 5.12 a). The moderate increase in strain hardening with the strain shown in the Johnson Cook Model is comparable to the measured response. The Johnson Cook model stress over-estimates the lower strain rate stress response and are closer with experiments at higher strain rates. As the stress measured at approximately 6760s⁻¹ did not show a notable increase in stress, the J-C model extrapolation may be representative of the stress-strain and strain hardening trend for IN718 up to 10^4s^{-1} and above. A summary of average measured stress and extrapolated stress is presented in Table 5.32. The measured stress at 2770s^{-1} , estimated as $2.8 \times 10^3 \text{s}^{-1}$, was averaged from about 0.02 to 0.22 strain. For higher strain rates, the strain interval was between 0.02 to 0.3.

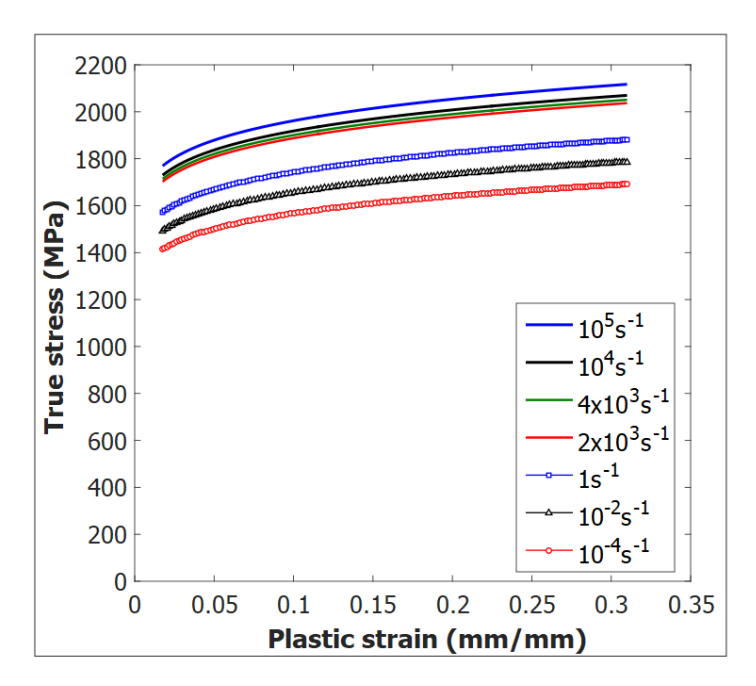


Figure 5.12. Johnson Cook model stress-strain extrapolated at varying strain rates and 25°C for IN718.

Table 5.32. Average measured stress and extrapolated stress at 25°C for IN718.

Avg. Stress (MPa)	$2 \times 10^{3} \text{s}^{-1}$	$2.8 \times 10^{3} \text{s}^{-1}$	$4 \times 10^{3} \text{s}^{-1}$	$10^4 s^{-1}$	$10^{5} \mathrm{s}^{-1}$
Experiment – 25°C	-	1821±6.0	1915±7.6	-	-
Extrapolated Stress – Johnson Cook Model	1929±7.4	-	1943±7.5	1960±7.6	2006±7.7

The extrapolation using the modified KHL model (equation 2.12) is presented in Figure 5.13. The model accounts for a decrease in strain hardening with increasing strain rate in the term, $B\left(1-\frac{\ln\epsilon}{\ln D_0^P}\right)^{n_1}.$ Above a certain strain rate, the decrease in strain hardening outweighs the positive strain rate sensitivity factor $\left(\frac{\epsilon}{\epsilon_{ref}}\right)^C$. The extrapolated stress-strain at from $2\times 10^3 s^{-1}$ to $10^4 s^{-1}$ therefore closely overlap. The predicted stress-strain at $10^5 s^{-1}$ is lower than that at $10^4 s^{-1}$. The model is thus not likely suitable for extrapolating to higher strain rates of $10^4 s^{-1}$ for IN718.

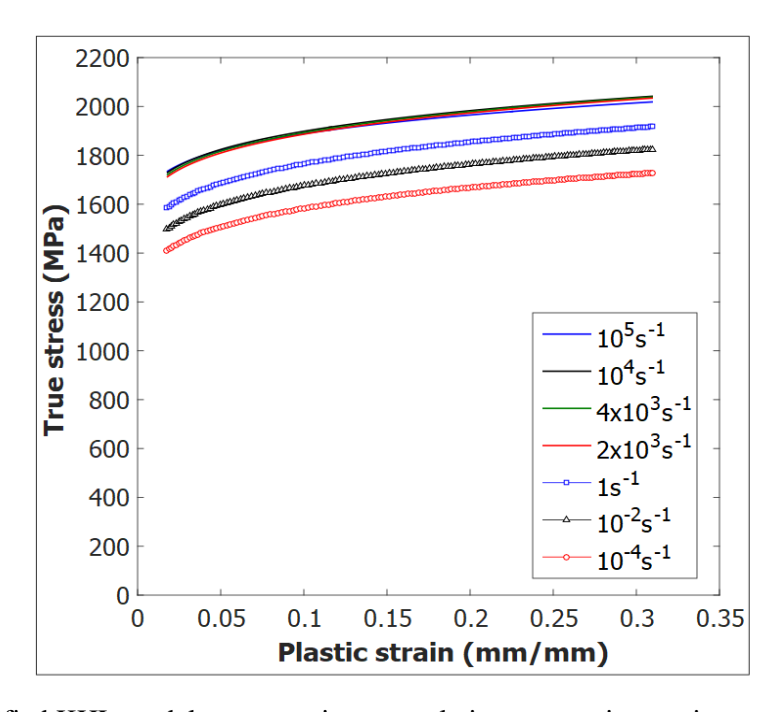


Figure 5.13. Modified KHL model stress-strain extrapolations at varying strain rates and 25°C for IN718.

The equivalent strain rate of the low temperature test result at 25° C, estimated using the Johnson Cook model, is shown in Figure 5.14. The model parameters used were summarized in Table 5.15. The average stress for the experiment at -110°C and $4130s^{-1}$ from about 0.02 to 0.3 strain was 2044 ± 8.4 MPa. The average extrapolated stress using the model was 2044 ± 8.2 MPa. The evaluated strain rate is higher compared to typical strain rate range observed in peening. Given the stress of the Johnson Cook model increases linearly with the logarithm of the strain rate, the strain rate value may be a high value when the model is used to estimate a higher stress-strain response.

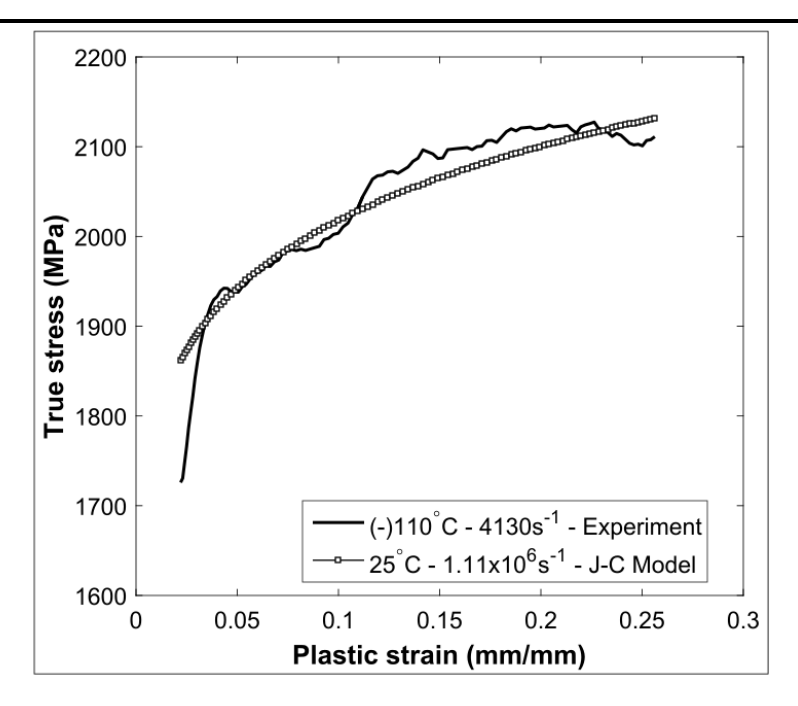


Figure 5.14. Measured stress-strain at -110°C and 4130s⁻¹ compared to the fitted stress at 25°C and a higher strain rate using the Johnson Cook model for IN718.

Table 5.33. Equivalent strain rate of cooling test at 25°C and closeness-of-fit values for IN718.

Upper Bound	Lower Bound	Strain rate at 25°C	Mean square error	\mathbb{R}^2
$10^3 s^{-1}$	$10^{5} \mathrm{s}^{\text{-1}}$	$1.11 \times 10^6 \text{s}^{-1}$	956	0.89

5.4.3 300M

The constitutive model extrapolations for 300M steel at varying strain rates and 25°C is presented in Figure 5.14. In Figure 5.14 a), the Johnson Cook model shows a linear increase in strain rate sensitivity. The extrapolated trend does not correlate well with the measured trend at dynamic strain rates and 25°C. The extrapolated stress using the J-C- Cowper Symonds model, shown in Figure 5.14 b), also consist of a positive strain hardening trend. The model does not show a notable difference in strength at between 10^{-4}s^{-1} and 1s^{-1} . At strain rates of 10^{3}s^{-1} and above, the strength notably increases due to the power law formulation of the strain rate in the model. The extrapolations using J-C Voce strain hardening model, presented in Figure 5.14 c), better represent the measured stress saturation response. The predicted stress does not exhibit a notable increase in strength above 10^{3}s^{-1} , as in the case shown for Aluminum 7050-T7451 in

Figure 5.10 b). From the model constants evaluated for 300M steel, the parameter (*E*) was 10^{-4}s^{-1} , an order of magnitude lower than that for Aluminum. The strain rate sensitivity term $\exp(\text{E} \times \frac{\dot{\epsilon}}{\dot{\epsilon}_{\text{ref}}})$ is therefore of a low value and do not increase the strength significantly above 10^{3}s^{-1} . The strain rate sensitivity of the extrapolated stress from 10^{3}s^{-1} to 10^{4}s^{-1} and above is slightly greater compared to that evaluated using the Johnson Cook model. The average extrapolated stress and experiment stress are summarized in Table 5.34. The average experiment stress was evaluated from 0.02 to 0.148 strain, the lowest value of the measured strain.

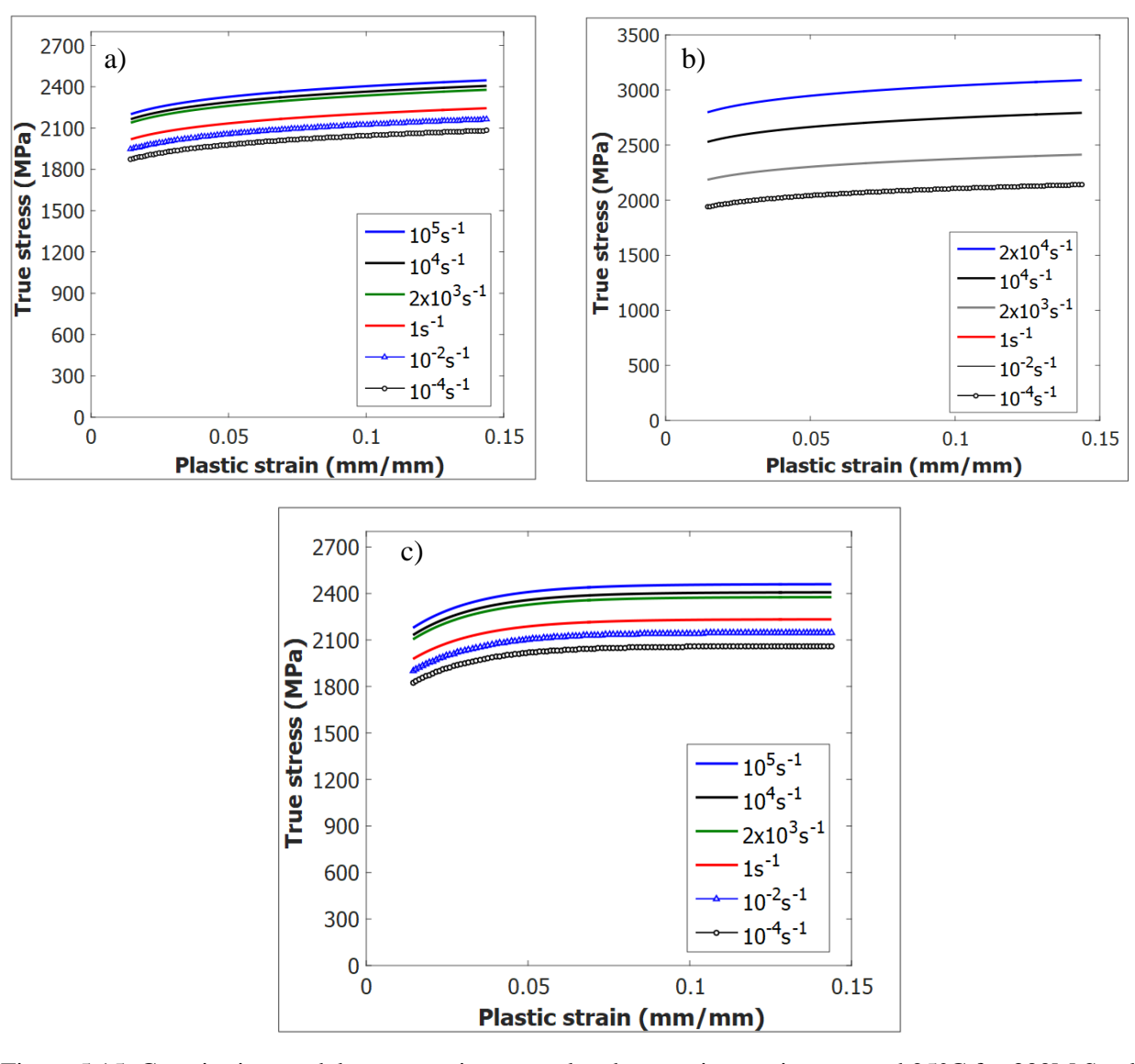


Figure 5.15. Constitutive model stress-strain extrapolated at varying strain rates and 25°C for 300M Steel. a) Johnson Cook model. b) J–C – Cowper Symonds model. c) J–C – Voce strain hardening model.

Table 5.34. Average measured stress and extrapolated stress at 25°C for 300M Steel.

Average Stress (MPa)	$2 \times 10^{3} \text{s}^{-1}$	$2.4 \times 10^{3} \text{s}^{-1}$	$3 \times 10^{3} \text{s}^{-1}$	$10^4 s^{-1}$	$2 \times 10^4 \text{s}^{-1}$	$10^{5} \mathrm{s}^{-1}$
Experiment – 25°C	-	2342±8.6	2335±6.7	-	-	-
Extrapolation – J-C Model	2303±5.4	-	-	2330±5.0	-	2369±5.6
Extrapolation – J-C Cowper Symonds	2342±5.2	-	-	2710±5.9	2997±6.2	-
Extrapolation – J-C Voce strain hardening	2341±4.8	-	-	2372±4.9	-	2424±5.0

From compressive SHPB results reported in literature for steel alloys, the strain rate sensitivity at 25°C is typically most notable from $10^3 s^{-1}$ to $5 \times 10^3 s^{-1}$, and the relative change in stress decreases at higher strain rates for example due to softening. Alkhader and Bodelot [129] presented results for a HSLA-100 alloy, where the average stress between 0.05 to 0.3 true strain increased by about 200 MPa from $2 \times 10^3 \text{s}^{-1}$ and $9 \times 10^3 \text{s}^{-1}$. Stress-strain results at $6.8 \times 10^3 \text{s}^{-1}$ and above displayed negative strain hardening rate, and the strength increased moderately between 9×10^3 s⁻¹ and 1.3×10^4 s⁻¹ by about 50 MPa. Malinowski et al. [130] has shown for a 34GS construction steel, the stress between 10^3 s⁻¹ to 5×10^3 s⁻¹ increased by about 80 MPa. The strain rate sensitivity between the lower rates was greater than that from $5 \times 10^3 \text{s}^{-1}$ to $4 \times 10^4 \text{s}^{-1}$ measured using a direct-impact compression bar. The high strain rate data for 4340 steel, presented in Figure 2.13, similarly shows an increase in rate sensitivity between 10^3s^{-1} to $4 \times 10^3 \text{s}^{-1}$. Based on typical trends for steel alloys which exhibit high strain rate sensitivity at 25°C and the negative strain hardening rate of 300M steel observed in this study, the predicted stress using the Cowper Symonds model at 10⁴s⁻¹ is clearly very high and would not be representative of the material behavior at 10⁴s⁻¹ and above. The Johnson Cook Voce-hardening model by comparison may provide a reasonable estimate of the strength in the strain rate regimes of $10^5 s^{-1}$ to $10^6 s^{-1}$.

The equivalent strain rate of the low temperature result at 25°C, using the Johnson Cook Voce strain hardening model is shown in Figure 5.16. The closeness-of-fit values are summarized in Table 5.35. The average stress of the result obtained at -70°C and $2350s^{-1}$ from about 0.03 to 0.148 strain was 2584 ± 10.6 MPa. The average extrapolated stress was 2591 ± 5.4 MPa. The evaluated strain rate is also at the higher approximated rate value estimated in peening. The model constants of the strain rate sensitivity factor do not indicate a notable increase in strength for 300M Steel.

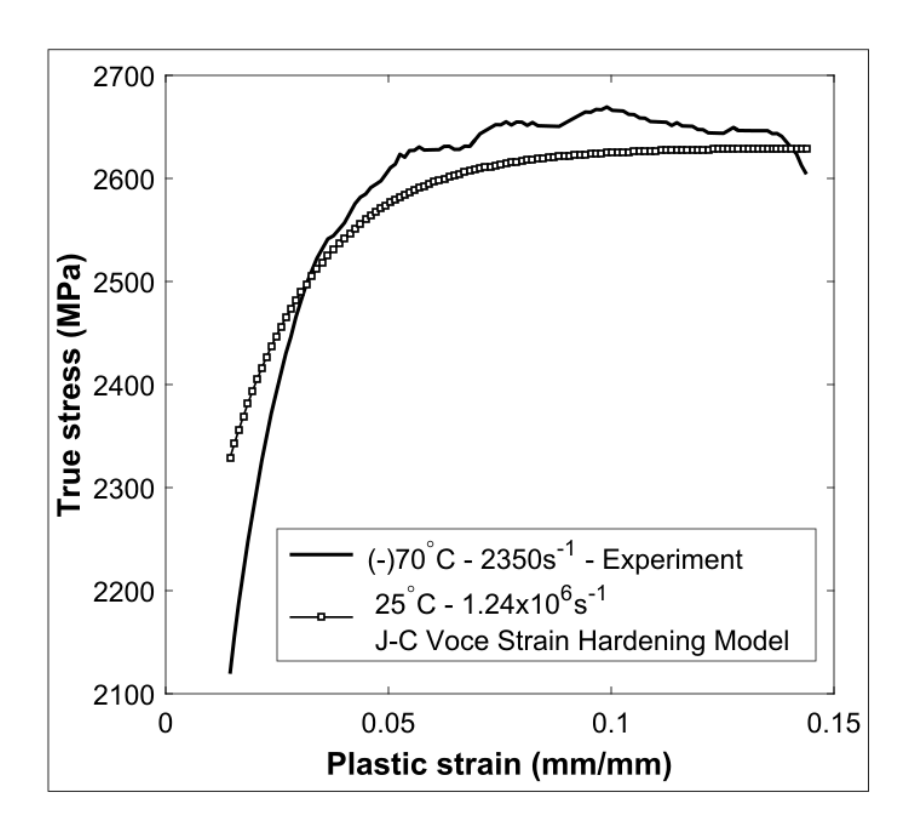


Figure 5.16. Measured stress-strain at -70°C and 2350s⁻¹ compared to the fitted stress at 25°C and a higher strain rate using the J-C Voce strain hardening model for 300M Steel.

Table 5.35. Equivalent strain rate of cooling test at 25°C and closeness-of-fit values for 300M Steel.

Upper Bound	Lower Bound	Solution	Mean square error	\mathbb{R}^2
$10^4 \mathrm{s}^{-1}$	$10^{7} \mathrm{s}^{-1}$	$1.24 \times 10^6 \text{s}^{-1}$	5289	0.63

Chapter 6 Conclusion

6.1 Summary

A Split Hopkinson bar compression method was applied to investigate the stress-strain response of AA7050-T7451, heat treated IN718, and 300M steel alloys under high strain rates and varying temperatures. The experimental results were applied to evaluate the effects of strain rate and temperature on strain hardening, and to obtain representative strain rate sensitivity parameters of the materials by constitutive model correlations. Strain rate conditions were chosen to attain the highest possible level of stress, and the range of temperature considered was to avoid incurring microstructural changes, complex strain hardening trends, and to focus on only the changes in stress due to temperature. The evaluation of constitutive relations focused on empirical based models with relatively simple form and few model constants for ease of identification, comparison, and implementation. The stress-strain response of the alloys was extrapolated at higher strain rates and 25°C to illustrate representative stress-strain response at shot peening conditions.

The main features of stress-strain response of the three alloys obtained from Split Hopkinson compression bars testing are summarized as follows:

At a representative dynamic strain rate of 2000s⁻¹ and 25°C, AA7050-T7451 displays a positive strain hardening up to around 10% true strain, followed by stress saturation and gradual softening which reflect the onset of dynamic recovery. The initial strain hardening rate was slightly greater at 10³s⁻¹ than at 2000s⁻¹ rate of strain that may indicate adiabatic heating effects. At a strain rate of 2770s⁻¹, transverse shear failure occurred to the sample, and the strength was close to the stress-strain result at 2000s⁻¹. From temperature sensitivity tests at an average strain rate of 2000s⁻¹, negative strain hardening of AA7050-T7451 was significant at 100°C and 200°C. In addition, the degree of thermal softening (MPa /°C) increased between 100°C and 200°C, when compared to the intervals at lower temperatures.

Dynamic stress-strain response of IN718 at strain rates of 2770s⁻¹ and 4000s⁻¹, 25°C exhibited positive strain hardening over the measured strain. Strain hardening rate under compression was moderately lower with increasing strain rates, when compared at specific true strains of 10% and 15%, likely due to the increase in adiabatic heating effects. At a strain rate of 6760s⁻¹, the sample exhibited significant failure by shearing, and strain softening is evident by the stress drop in the stress from 25 to 30% true strain. At 500°C and an average strain rate of 4000s⁻¹, the stress-strain exhibited a relatively constant plateau and strain hardening rate during plastic strain.

300M steel tests at an average strain rate of 3000s⁻¹ and 25°C exhibited a constant stress plateau and gradual softening with increasing strain. At 200°C and an average strain rate of 2400s⁻¹, the stress-strain result showed an increase in strain hardening from 5% to 10% true strain such that the peak stress was notably higher than the yield region. The strain hardening trend at 500°C was closer to the trends at -70°C and 25°C, and did not exhibit a transition as the result at 200°C. Despite testing at varying temperatures, sample failure by shear or fracture occurred in all cases, and the steady-state strain measured was relatively low (<15% true strain).

The main conclusions for the constitutive model evaluations and extrapolations are as follows:

For AA7050-T7451, experimental correlation results using the J-C Voce hardening model was improved when compared to the Johnson Cook and J-C adiabatic heating models. The Voce strain hardening law better accounts for stress saturation with increasing strain. Given that thermal softening rate increased between 100°C to 200°C due to possible microstructural changes, the result at 200°C was excluded in the model evaluation. The result at 100°C, however, also exhibited negative strain hardening, and therefore cannot be predicted by a positive strain hardening trend featured in most models.

For IN718 experiments, the modified KHL model provided a better correlation than the Johnson Cook and modified Johnson Cook models. The modified KHL model consists of the same multiplicative form as the Johnson Cook models and considers the coupling of strain rate and strain hardening. The strain rate and temperature terms also consists of different forms, which may have provided improvement of correlating to the SHPB experiment results.

For models fitting to 300M experiments, the Johnson Cook Cowper Symonds and J-C Voce strain hardening models provided similar degree of correlations. Despite the expected shortcomings of the Johnson Cook model form in fitting to BCC structures and the lower degree of consistency in the stress-strain data, the correlations on average approximately represented the peak stress-strain for most of the dynamic test conditions.

The model with a better degree of fitting to experiments may not be better suited to extrapolate the stress at higher strain rates of $10^4 \mathrm{s}^{-1}$ to $10^5 \mathrm{s}^{-1}$. The KHL model stress for IN718 did not predict sufficient strength agreeable with experiments. The J-C Cowper Symonds model for 300M steel overestimates the strain rate sensitivity above $10^4 \mathrm{s}^{-1}$. In addition to the strain rate sensitivity form, the predicted stress depends on parameters obtained from fitting to experiments. The strain rate sensitivity using the J-C Voce strain hardening model from $10^4 \mathrm{s}^{-1}$ to $10^5 \mathrm{s}^{-1}$ was greater for Aluminum 7050-T7451 compared to 300M Steel due to the difference in parameter values in the strain rate sensitivity factor. In addition to strain rate sensitivity, the stress-strain response depends on strain hardening capacity at very high strain rates. For IN718 reported in Figure 2.12 for example, the peak stress level does not correspond to the highest strain rate at 25°C due to excessive softening. For the HSLA-100 steel example discussed, the average peak stress corresponded to the highest strain rate condition despite strain softening observed.

The low temperatures SHPB tests obtained for the alloys in this study may be representative of an increase in strength at a higher strain rate at 25°C. The approximate equivalent strain rate at 25°C was between 10⁵s⁻¹ up to about 10⁶s⁻¹ as evaluated using SHPB test data and empirical based stress-strain models. The very high strain rates ranging from 10⁴s⁻¹ to 10⁶s⁻¹ representative of shot peening conditions are values typically obtained using more specialized experimental methods such as Taylor impact and denotation-driven flyer plates tests [37]. A comparison between the measured stress from plate-driven impact tests and the calculated stress using constitutive models by finite element analysis for example, may be used to examine the suitability of using constitutive models to extrapolate to high strain rates [7]. The equivalent stress-strain response obtained using cooling tests may also be compared in a similar manner.

6.2 Future Work

In terms of experimental methods, the choice of sample geometry, pulse shaper material, and dimensions could be further examined for IN718 and 300M steel samples. The pulse shapers and sample sizes used in the present study were focused on minimizing dispersion effects and to obtain measurable stress-strain responses at representative dynamic strain rates. Different shaper materials with higher strength than AA6061 and Copper could be used for example, with different sample aspect ratios to examine if the dynamic strain rate trend for IN718 and 300M steel could attain a steady plateau as in the case for AA7050-T7451. Different sample geometries could be used also to examine the possibility of attaining higher strain rates than presented in the study at 25°C to examine the limits of stress saturation in the stress-strain response.

For experimental data, quasi-static tests completed under compression instead of tension, that removes tension-compression asymmetry effects, would be more ideal for comparison with Hopkinson compression results. Additional test results at intermediate strain rates (10²s⁻¹ to 10³s⁻¹) would improve quantification of the strain rate sensitivity for the different alloys. Similarly, IN718 results in this work lacked additional elevated temperature data to better determine thermal softening trends. 300M steel could be tested using different sample dimensions and gas-gun pressures to attain different average strain rate, which may possibly minimize shear failure and enable greater strain measured. Improvement in the experimental data enables for more accurate evaluation of the constitutive model fitting and high strain rate extrapolation results.

References

- [1] S. Meguid, G. Shagal, J. Stranart, 3D FE analysis of peening of strain-rate sensitive materials using multiple impingement model, International Journal of Impact Engineering 27(2) (2002) 119-134.
- [2] M. Frija, T. Hassine, R. Fathallah, C. Bouraoui, A. Dogui, Finite element modelling of shot peening process: Prediction of the compressive residual stresses, the plastic deformations and the surface integrity, Materials Science and Engineering: A 426(1-2) (2006) 173-180.
- [3] K. Schiffner, Simulation of residual stresses by shot peening, Computers & structures 72(1) (1999) 329-340.
- [4] G.I. Mylonas, G. Labeas, Numerical modelling of shot peening process and corresponding products: Residual stress, surface roughness and cold work prediction, Surface and Coatings Technology 205(19) (2011) 4480-4494.
- [5] M. Klemenz, V. Schulze, I. Rohr, D. Löhe, Application of the FEM for the prediction of the surface layer characteristics after shot peening, Journal of Materials Processing Technology 209(8) (2009) 4093-4102.
- [6] P. Sanjurjo, C. Rodríguez, I. Peñuelas, T.E. García, F.J. Belzunce, Influence of the target material constitutive model on the numerical simulation of a shot peening process, Surface and Coatings Technology 258 (2014) 822-831.
- [7] K. Langer, S. Olson, R. Brockman, W. Braisted, T. Spradlin, M.E. Fitzpatrick, High strain-rate material model validation for laser peening simulation, Journal of Engineering 1(1) (2015).
- [8] H. Luong, M.R. Hill, The effects of laser peening and shot peening on high cycle fatigue in 7050-T7451 aluminum alloy, Materials Science and Engineering: A 527(3) (2010) 699-707.
- [9] S.A. Barter, Fatigue Crack Growth in Several 7050T7451 Aluminium Alloy Thick Section Plates with Aircraft Manufacturer's and Laboratory Surface Finishes Representing Some Regions of the F/A-18 Structure, DTIC Document, 2003.
- [10] P.R. Bhowal, D. Stolz, A.M. Wusatowska-Sarnek, R. Montero, S. 11th International Symposium on Superalloys, Surface effects on low cycle fatigue behavior in IN718 alloy, Proc Int Symp Superalloys Proceedings of the International Symposium on Superalloys (2008) 417-423.
- [11] J.A. Charles, F.A.A. Crane, Chapter 15 Materials for airframes, Selection and Use of Engineering Materials (Second Edition), Butterworth-Heinemann1989, pp. 233-263.
- [12] S.A. Barter, L. Molent, R.J.H. Wanhill, Typical fatigue-initiating discontinuities in metallic aircraft structures, International Journal of Fatigue 41 (2012) 11-22.

- [13] P.K. Sharp, J.Q. Clayton, G. Clark, The Fatigue Resistance of Peened 7050-T7451 Aluminium Alloy-Repair and Re-treatment of a Component Surface, Fatigue and Fracture of Engineering Materials and Structures 17(3) (1994) 243.
- [14] P. Larour, A. Bäumer, K. Dahmen, W. Bleck, Influence of strain rate, temperature, plastic strain, and microstructure on the strain rate sensitivity of automotive sheet steels, Steel Research International 84(5) (2013) 426-442.
- [15] J.L. Jordan, C.R. Siviour, G. Sunny, C. Bramlette, J.E. Spowart, Strain rate-dependent mechanical properties of OFHC copper, Journal of Materials Science 48(20) (2013) 7134-7141.
- [16] A. Rusinek, J. Rodríguez-Martínez, Thermo-viscoplastic constitutive relation for aluminium alloys, modeling of negative strain rate sensitivity and viscous drag effects, Materials & Design 30(10) (2009) 4377-4390.
- [17] A. Uenishi, C. Teodosiu, Constitutive modelling of the high strain rate behaviour of interstitial-free steel, International Journal of Plasticity 20(4) (2004) 915-936.
- [18] M.A. Meyers, Plastic Deformation at High Strain Rates, Dynamic Behavior of Materials, John Wiley & Sons, Inc.2007, pp. 323-381.
- [19] M.A. Meyers, D.J. Benson, O. Vo, B.K. Kad, Q. Xue, Constitutive description of dynamic deformation: physically-based mechanisms, 322 (2002) 194-216.
- [20] J.A. Rodríguez-Martínez, M. Rodríguez-Millán, A. Rusinek, A. Arias, A dislocation-based constitutive description for modeling the behavior of FCC metals within wide ranges of strain rate and temperature, Mechanics of Materials 43(12) (2011) 901-912.
- [21] S. Nemat-Nasser, Introduction to High Strain Rate Testing, Materials Park, OH: ASM International, 2000. (2000) 427-428.
- [22] W.W. Chen, B. Song, Testing Conditions in Kolsky Bar Experiments, Split Hopkinson (Kolsky) Bar: Design, Testing and Applications, Springer US, Boston, MA, 2011, pp. 37-75.
- [23] G. Gary, Testing With Bars From Dynamic to Quasi-static, in: T. Łodygowski, A. Rusinek (Eds.), Constitutive Relations under Impact Loadings: Experiments, Theoretical and Numerical Aspects, Springer Vienna, Vienna, 2014, pp. 1-58.
- [24] G.T. Gray, Classic Split-Hopkinson Pressure Bar Testing, Materials Park, OH: ASM International, 2000. (2000) 462-476.
- [25] X. Tang, V. Prakash, J. Lewandowski, Dynamic deformation of aluminum 6061 in two different heat-treatments, 2005 SEM Annual Conference and Exposition on Experimental and Applied Mechanics, June 7, 2005 June 9, 2005, Society for Experimental Mechanics Inc., Portland, OR, United states, 2005, pp. 149-155.

- [26] K.T. Ramesh, High Rates and Impact Experiments, in: W.N. Sharpe (Ed.), Springer Handbook of Experimental Solid Mechanics, Springer US, Boston, MA, 2008, pp. 929-960.
- [27] B. Song, W. Chen, Energy for specimen deformation in a split Hopkinson pressure bar experiment, Experimental Mechanics 46(3) (2006) 407-410.
- [28] B.A. Gama, S.L. Lopatnikov, J.W. Gillespie, Hopkinson bar experimental technique: a critical review, Applied Mechanics Reviews 57(4) (2004) 223-250.
- [29] G.T. Gray, High-Strain-Rate Testing of Materials: The Split-Hopkinson Pressure Bar, Characterization of Materials, John Wiley & Sons, Inc.2002.
- [30] J. Malinowski, J. Klepaczko, A unified analytic and numerical approach to specimen behaviour in the split-Hopkinson pressure bar, International journal of mechanical sciences 28(6) (1986) 381-391.
- [31] T. Jankowiak, A. Rusinek, T. Lodygowski, Validation of the Klepaczko–Malinowski model for friction correction and recommendations on Split Hopkinson Pressure Bar, Finite Elements in Analysis and Design 47(10) (2011) 1191-1208.
- [32] I.W. Hall, M. Guden, Split Hopkinson pressure bar compression testing of an aluminum alloy: effect of lubricant type, Journal of materials science letters 22(21) (2003) 1533-1535.
- [33] M. Bolduc, R. Arsenault, Response of split Hopkinson pressure bars to end-surface damage, Journal de Physique IV (Proceedings), EDP sciences, 2006, pp. 751-755.
- [34] A. Bouamoul, M. Bolduc, M. th International Conference on the, D. Physical Behaviour of Materials Under Dynamic Loading, Response of split Hopkinson bar apparatus signal to end-surface damage, numerical and experimental studies, EPJ Web Conf. EPJ Web of Conferences 26 (2012).
- [35] D. Parry, A. Walker, P. Dixon, Hopkinson bar pulse smoothing, Measurement Science and Technology 6(5) (1995) 443.
- [36] M.A. Kariem, J.H. Beynon, D. Ruan, Misalignment effect in the split Hopkinson pressure bar technique, International Journal of Impact Engineering 47 (2012) 60-70.
- [37] J. Field, S. Walley, W. Proud, H. Goldrein, C. Siviour, Review of experimental techniques for high rate deformation and shock studies, International journal of impact engineering 30(7) (2004) 725-775.
- [38] M. Al-Mousawi, S. Reid, W. Deans, The use of the split Hopkinson pressure bar techniques in high strain rate materials testing, Proceedings of the Institution of Mechanical Engineers, Part C: Journal of Mechanical Engineering Science 211(4) (1997) 273-292.
- [39] G.T. Gray, High-Strain-Rate Deformation: Mechanical Behavior and Deformation Substructures Induced, Annual Review of Materials Research 42(1) (2012) 285-303.
- [40] E. Davies, S. Hunter, The dynamic compression testing of solids by the method of the split Hopkinson pressure bar, Journal of the Mechanics and Physics of Solids 11(3) (1963) 155-179.

- [41] L. Yang, V. Shim, An analysis of stress uniformity in split Hopkinson bar test specimens, International Journal of Impact Engineering 31(2) (2005) 129-150.
- [42] H. Zhao, G. Gary, On the use of SHPB techniques to determine the dynamic behavior of materials in the range of small strains, International Journal of Solids and structures 33(23) (1996) 3363-3375.
- [43] W. Chen, B. Song, D. Frew, M. Forrestal, Dynamic small strain measurements of a metal specimen with a split Hopkinson pressure bar, Experimental Mechanics 43(1) (2003) 20-23.
- [44] R. Naghdabadi, M. Ashrafi, J. Arghavani, Experimental and numerical investigation of pulse-shaped split Hopkinson pressure bar test, Materials Science and Engineering: A 539 (2012) 285-293.
- [45] F. Jiang, K.S. Vecchio, Hopkinson Bar Loaded Fracture Experimental Technique: A Critical Review of Dynamic Fracture Toughness Tests, Applied Mechanics Reviews 62(6) (2009) 060802-060802-39.
- [46] K.S. Vecchio, F. Jiang, Improved pulse shaping to achieve constant strain rate and stress equilibrium in split-Hopkinson pressure bar testing, Metallurgical and materials transactions A 38(11) (2007) 2655-2665.
- [47] C. Frantz, P. Follansbee, W. Wright, New experimental techniques with the split Hopkinson pressure bar, 8th International Conference on High Energy Rate Fabrication, San Antonio, TX, June, 1984, pp. 17-21.
- [48] J. Kajberg, K.-G. Sundin, Material characterisation using high-temperature Split Hopkinson pressure bar, Journal of Materials Processing Technology 213(4) (2013) 522-531.
- [49] J.J. DeMange, V. Prakash, J.M. Pereira, Effects of material microstructure on blunt projectile penetration of a nickel-based super alloy, International Journal of Impact Engineering 36(8) (2009) 1027-1043.
- [50] D. Frew, M.J. Forrestal, W. Chen, A split Hopkinson pressure bar technique to determine compressive stress-strain data for rock materials, Experimental mechanics 41(1) (2001) 40-46.
- [51] D. Frew, M.J. Forrestal, W. Chen, Pulse shaping techniques for testing brittle materials with a split Hopkinson pressure bar, Experimental mechanics 42(1) (2002) 93-106.
- [52] A. Marchand, J. Duffy, An experimental study of the formation process of adiabatic shear bands in a structural steel, Journal of the Mechanics and Physics of Solids 36(3) (1988) 251-283.
- [53] M. Shazly, V. Prakash, S. Draper, Mechanical behavior of Gamma-Met PX under uniaxial loading at elevated temperatures and high strain rates, International journal of solids and structures 41(22) (2004) 6485-6503.
- [54] Z. Rosenberg, D. Dawicke, E. Strader, S. Bless, A new technique for heating specimens in split-Hopkinson-bar experiments using induction-coil heaters, Experimental Mechanics 26(3) (1986) 275-278.
 [55] J. Chiddister, L. Malvern, Compression-impact testing of aluminum at elevated temperatures,

Experimental Mechanics 3(4) (1963) 81-90.

- [56] V.-T. Kuokkala, M. Apostol, M. Hokka, High and low temperature techniques in Hopkinson split bar testing, Proceedings of the IMPLAST 2010 Conference, 2010, pp. 12-14.
- [57] Y. Wang, Z. Jiang, Dynamic compressive behavior of selected aluminum alloy at low temperature, Materials Science and Engineering: A 553 (2012) 176-180.
- [58] A. Lennon, K. Ramesh, A technique for measuring the dynamic behavior of materials at high temperatures, International Journal of Plasticity 14(12) (1998) 1279-1292.
- [59] B. Song, B. Antoun, X. Nie, W. Chen, High-rate characterization of 304L stainless steel at elevated temperatures for recrystallization investigation, Experimental mechanics 50(4) (2010) 553-560.
- [60] D.A. Clark, W.S. Johnson, Temperature effects on fatigue performance of cold expanded holes in 7050-T7451 aluminum alloy, International journal of fatigue 25(2) (2003) 159-165.
- [61] F.C. Campbell, Chapter 2 Aluminum, Manufacturing Technology for Aerospace Structural Materials, Elsevier Science, Oxford, 2006, pp. 15-92.
- [62] B. Huang, Y. Kaynak, Y. Sun, I.S. Jawahir, Surface Layer Modification by Cryogenic Burnishing of Al 7050-T7451 Alloy and Validation with FEM-based Burnishing Model, Procedia CIRP 31 (2015) 1-6.
- [63] F. Jiang, J. Li, J. Sun, S. Zhang, Z. Wang, L. Yan, Al7050-T7451 turning simulation based on the modified power-law material model, The International Journal of Advanced Manufacturing Technology 48(9-12) (2009) 871-880.
- [64] D. Holt, The strain rate dependence of the flow stress in some aluminum alloys, Trans. ASM 60 (1967) 152-158.
- [65] G. Wulf, The high strain rate compression of 7039 aluminium, International Journal of Mechanical Sciences 20(9) (1978) 609-615.
- [66] B. Mishra, C. Mondal, R. Goyal, P. Ghosal, K.S. Kumar, V. Madhu, Plastic flow behavior of 7017 and 7055 aluminum alloys under different high strain rate test methods, Materials Science and Engineering: A 612 (2014) 343-353.
- [67] G. Chen, C. Ren, Z. Ke, J. Li, X. Yang, Modeling of flow behavior for 7050-T7451 aluminum alloy considering microstructural evolution over a wide range of strain rates, Mechanics of Materials 95 (2016) 146-157.
- [68] J.H. Song, H. Huh, The effect of strain rate on the material characteristics of nickel-based superalloy Inconel 718, Key Engineering Materials, Trans Tech Publ, 2007, pp. 283-288.
- [69] T.J. Liutkus, Digital Image Correlation in Dynamic Punch Testing and Plastic Deformation Behavior of Inconel 718, The Ohio State University, 2014.
- [70] X. Wang, C. Huang, B. Zou, H. Liu, H. Zhu, J. Wang, Dynamic behavior and a modified Johnson—Cook constitutive model of Inconel 718 at high strain rate and elevated temperature, Materials Science and Engineering: A 580 (2013) 385-390.

- [71] G. Malakondaiah, M. Srinivas, P.R. Rao, Ultrahigh-strength low-alloy steels with enhanced fracture toughness, Progress in materials Science 42(1-4) (1997) 209-242.
- [72] F.C. Campbell, Chapter 5 High Strength Steels, Manufacturing Technology for Aerospace Structural Materials, Elsevier Science, Oxford, 2006, pp. 175-209.
- [73] S.S. Zhang, M.Q. Li, Y.G. Liu, J. Luo, T.Q. Liu, The growth behavior of austenite grain in the heating process of 300M steel, Materials Science and Engineering: A 528(15) (2011) 4967-4972.
- [74] W. Lee, H. Lam, Mechanical response and dislocation substructure of high strength Ni-Cr-Mo steel subjected to impact loading, Le Journal de Physique IV 4(C8) (1994) C8-307-C8-312.
- [75] G. Owolabi, D. Odoh, A. Odeshi, H. Whitworth, Occurrence of Dynamic Shear Bands in AISI 4340 Steel under Impact Loads, WJM World Journal of Mechanics 03(02) (2013) 139-145.
- [76] B. Song, W. Chen, B. Antoun, D. Frew, Determination of early flow stress for ductile specimens at high strain rates by using a SHPB, Experimental Mechanics 47(5) (2007) 671-679.
- [77] W.-S. Lee, C.-R. Lin, Deformation behavior and microstructural evolution of 7075-T6 aluminum alloy at cryogenic temperatures, Cryogenics 79 (2016) 26-34.
- [78] W.-S. Lee, C.-F. Lin, T.-H. Chen, H.-W. Chen, Dynamic Impact Response of Inconel 718 Alloy under Low and High Temperatures, Materials Transactions 52(9) (2011) 1734-1740.
- [79] U. Kocks, H. Mecking, Physics and phenomenology of strain hardening: the FCC case, Progress in materials science 48(3) (2003) 171-273.
- [80] S. Nemat-Nasser, W.-G. Guo, Thermomechanical response of HSLA-65 steel plates: experiments and modeling, Mechanics of Materials 37(2) (2005) 379-405.
- [81] L.W. Meyer, T. Halle, N. Herzig, L. Krüger, S.V. Razorenov, Experimental investigations and modelling of strain rate and temperature effects on the flow behaviour of 1045 steel, J. Phys. IV France 134 (2006) 75-80.
- [82] J. Noble, B. Goldthorpe, P. Church, J. Harding, The use of the Hopkinson bar to validate constitutive relations at high rates of strain, Journal of the Mechanics and Physics of Solids 47(5) (1999) 1187-1206.
- [83] A.B. Tanner, R.D. McGinty, D.L. McDowell, Modeling temperature and strain rate history effects in OFHC Cu, International Journal of Plasticity 15(6) (1999) 575-603.
- [84] F.J. Zerilli, R.W. Armstrong, Dislocation-mechanics-based constitutive relations for material dynamics calculations, Journal of Applied Physics Journal of Applied Physics 61(5) (1987) 1816-1825.
- [85] S. Nemat-Nasser, Y. Li, Flow stress of fcc polycrystals with application to OFHC Cu, Acta Materialia 46(2) (1998) 565-577.
- [86] A. Rusinek, R. Zaera, J.R. Klepaczko, Constitutive relations in 3-D for a wide range of strain rates and temperatures—application to mild steels, International Journal of Solids and Structures 44(17) (2007) 5611-5634.

- [87] C. Gao, L. Zhang, Constitutive modelling of plasticity of fcc metals under extremely high strain rates, International Journal of Plasticity 32 (2012) 121-133.
- [88] H. Huh, K. Ahn, J.H. Lim, H.W. Kim, L.J. Park, Evaluation of dynamic hardening models for BCC, FCC, and HCP metals at a wide range of strain rates, Journal of Materials Processing Technology 214(7) (2014) 1326-1340.
- [89] A.S. Khan, H. Liu, Variable strain rate sensitivity in an aluminum alloy: Response and constitutive modeling, International Journal of Plasticity 36 (2012) 1-14.
- [90] R. Liu, M. Salahshoor, S. Melkote, T. Marusich, A unified material model including dislocation drag and its application to simulation of orthogonal cutting of OFHC Copper, Journal of Materials Processing Technology 216 (2015) 328-338.
- [91] J. Rämö, V.-T. Kuokkala, T. Vuoristo, Influence of strain rate and adiabatic heating on the deformation behavior of cold heading steels, Journal of Materials Processing Technology 209(11) (2009) 5186-5194.
- [92] G.R. Johnson, W.H. Cook, A constitutive model and data for metals subjected to large strains, high strain rates and high temperatures, Proceedings of the 7th International Symposium on Ballistics, The Hague, The Netherlands, 1983, pp. 541-547.
- [93] S. Nemat-Nasser, W.-G. Guo, Thermomechanical response of DH-36 structural steel over a wide range of strain rates and temperatures, Mechanics of Materials 35(11) (2003) 1023-1047.
- [94] R. Liang, A.S. Khan, A critical review of experimental results and constitutive models for BCC and FCC metals over a wide range of strain rates and temperatures, 15 (1999) 963-980.
- [95] Y. Lin, X.-M. Chen, A critical review of experimental results and constitutive descriptions for metals and alloys in hot working, Materials & Design 32(4) (2011) 1733-1759.
- [96] J.Q. Tan, M. Zhan, S. Liu, T. Huang, J. Guo, H. Yang, A modified Johnson–Cook model for tensile flow behaviors of 7050-T7451 aluminum alloy at high strain rates, Materials Science and Engineering: A 631 (2015) 214-219.
- [97] M. Vural, J. Caro, Experimental analysis and constitutive modeling for the newly developed 2139-T8 alloy, Materials Science and Engineering: A 520(1) (2009) 56-65.
- [98] H. Zhao, G. Gary, The testing and behaviour modelling of sheet metals at strain rates from 10–4 to 104 s–1, Materials Science and Engineering: A 207(1) (1996) 46-50.
- [99] L. Schwer, Optional Strain-rate forms for the Johnson Cook Constitutive Model and the Role of the parameter Epsilon_0.
- [100] A. Rusinek, R. Zaera, J.R. Klepaczko, R. Cheriguene, Analysis of inertia and scale effects on dynamic neck formation during tension of sheet steel, Acta Materialia 53(20) (2005) 5387-5400.

- [101] H. Shin, J.-B. Kim, A phenomenological constitutive equation to describe various flow stress behaviors of materials in wide strain rate and temperature regimes, Journal of Engineering Materials and Technology 132(2) (2010) 021009.
- [102] M. Hokka, T. Leemet, A. Shrot, M. Bäker, V.-T. Kuokkala, Dynamic behavior and numerical modeling of titanium 15-3-3-3 alloy, Dynamic Behavior of Materials, Volume 1, Springer2013, pp. 235-242.
- [103] G. Ravichandran, A.J. Rosakis, J. Hodowany, P. Rosakis, On the Conversion of Plastic Work into Heat during High-Strain-Rate Deformation, AIP conference proceedings. (620) (2002) 557-562.
- [104] T. Kobayashi, J. Simons, C. Brown, D. Shockey, Plastic flow behavior of Inconel 718 under dynamic shear loads, International Journal of Impact Engineering 35(5) (2008) 389-396.
- [105] A.S. Khan, S. Huang, Experimental and theoretical study of mechanical behavior of 1100 aluminum in the strain rate range 10–5–104s–1, International Journal of Plasticity 8(4) (1992) 397-424.
- [106] A.S. Khan, R. Kazmi, B. Farrokh, M. Zupan, Effect of oxygen content and microstructure on the thermo-mechanical response of three Ti–6Al–4V alloys: experiments and modeling over a wide range of strain-rates and temperatures, International Journal of Plasticity 23(7) (2007) 1105-1125.
- [107] W.W. Chen, B. Song, Kolsky Compression Bar Experiments on Soft Materials, Split Hopkinson (Kolsky) Bar: Design, Testing and Applications, Springer US, Boston, MA, 2011, pp. 119-175.
- [108] W.W. Chen, B. Song, Conventional Kolsky bars, Split Hopkinson (Kolsky) Bar: Design, Testing and Applications, Springer US, Boston, MA, 2011, pp. 1-35.
- [109] W.W. Chen, B. Song, Kolsky Compression Bar Experiments at High/Low Temperatures, Split Hopkinson (Kolsky) Bar: Design, Testing and Applications, Springer US, Boston, MA, 2011, pp. 233-260.
- [110] S. Curtze, M. Kundu, V.-T. Kuokkala, S. Datta, P. Chattopadhyay, Dynamic properties of new generation high-strength steels for armoring applications, Proceedings of the 2008 SEM XI International Congress and Exposition on Experimental and Applied Mechanics, June 2-5, 2008, Orlando, Florida, USA, 2008.
- [111] C. Bianchetti, Analytical fatigue life prediction for shot peened AA7050-T7451 (Unpublished Doctoral Thesis, Ecole Polytechnique, Montreal), 2016.
- [112] T. Klotz, Analytical fatigue life prediction for shot peened IN718 (Unpublished Doctoral Thesis, Ecole Polytechnique, Montreal), 2016.
- [113] A. Bag, Analytical fatigue life prediction for shot peened 300M (Unpublished Doctoral Thesis, Ecole Polytechnique, Montreal), 2016.

- [114] J. Johansson, Influence of microstructure of alloy 718 on high strain rate deformation, Materials Science and Technology Conference and Exhibition 2013, MS and T 2013; Montreal, QC; Canada; 27 October 2013 through 31 October 2013, 2013, pp. 2563-2570.
- [115] A.S. Khan, R. Liang, Behaviors of three BCC metal over a wide range of strain rates and temperatures: experiments and modeling, International Journal of Plasticity 15(10) (1999) 1089-1109.
- [116] C.A. Bronkhorst, E.K. Cerreta, Q. Xue, P.J. Maudlin, T.A. Mason, G.T. Gray, An experimental and numerical study of the localization behavior of tantalum and stainless steel, International Journal of Plasticity 22(7) (2006) 1304-1335.
- [117] Z.Q. Wang, J.F. Li, J. Sun, F. Jiang, J. Zhou, Flow stress determination of aluminum alloy 7050-T7451 using inverse analysis method, Key Engineering Materials, Trans Tech Publ, 2010, pp. 174-177.
- [118] S. Seo, O. Min, H. Yang, Constitutive equation for Ti–6Al–4V at high temperatures measured using the SHPB technique, International Journal of Impact Engineering 31(6) (2005) 735-754.
- [119] J.M. Pereira, B.A. Lerch, Effects of heat treatment on the ballistic impact properties of Inconel 718 for jet engine fan containment applications, International Journal of Impact Engineering 25(8) (2001) 715-733.
- [120] J.A. Canaveral, Application of material constitutive models and Split-Hopkinson pressure bar technique to two aerospace alloys: IN718 & 300m steel, (2017).
- [121] A.S. Khan, Y.S. Suh, R. Kazmi, Quasi-static and dynamic loading responses and constitutive modeling of titanium alloys, International Journal of Plasticity 20(12) (2004) 2233-2248.
- [122] H. Ledbetter, M. Austin, Elastic constant versus temperature behavior of three hardened maraging steels, Materials Science and Engineering 72(1) (1985) 65-69.
- [123] T. Skiba, B. Baufeld, O. Van der Biest, Shaped metal deposition of 300M steel, Proceedings of the Institution of Mechanical Engineers, Part B: Journal of Engineering Manufacture 225(6) (2011) 831-839.
- [124] C. International Nickel, Properties of some metals and alloys, International Nickel Co., New York, 1982.
- [125] S. Lin, F. Peng, Y. Liu, S. Yang, R. Yan, Finite Element Research on Cutting Force and Temperature in Milling 300M Steel, in: J. Lee, M.C. Lee, H. Liu, J.-H. Ryu (Eds.), Intelligent Robotics and Applications: 6th International Conference, ICIRA 2013, Busan, South Korea, September 25-28, 2013, Proceedings, Part II, Springer Berlin Heidelberg, Berlin, Heidelberg, 2013, pp. 481-490.
- [126] E. Lach, R. Schnitzer, H. Leitner, A. Redjaimia, H. Clemens, Behaviour of a maraging steel under quasi-static and dynamic compressive loading, International Journal of Microstructure and Materials Properties 5(1) (2010) 65-78.

- [127] W. Mocko, J.A. Rodríguez-Martínez, Z.L. Kowalewski, A. Rusinek, Compressive viscoplastic response of 6082-T6 and 7075-T6 Aluminium Alloys under wide range of strain rate at room temperature: experiments and modelling, STR Strain 48(6) (2012) 498-509.
- [128] G. Mylonas, G. Labeas, Mechanical Characterisation of Aluminium Alloy 7449 T7651 at High Strain Rates and Elevated Temperatures Using Split Hopkinson Bar Testing, Experimental Techniques 38(2) (2014) 26-34.
- [129] M. Alkhader, L. Bodelot, Large strain mechanical behavior of HSLA-100 steel over a wide range of strain rates, Journal of Engineering Materials and Technology 134(1) (2012) 011005.
- [130] J.Z. Malinowski, J.R. Klepaczko, Z.L. Kowalewski, Miniaturized Compression Test at Very High Strain Rates by Direct Impact, Experimental Mechanics 47(4) (2007) 451-463.

Appendix A

Example MATLAB code for fitting Johnson Cook constitutive model to Aluminum 7050-T7451 data with five experimental conditions shown in Figure 5.1b)

```
% Read experimental data from excel file.
filename = uigetfile('*.xlsx');
AA7050 = xlsread(filename, -1);
strain = AA7050(:,1);
stress = AA7050 (:,2);
rate = AA7050 (:,3);
temp = AA7050 (:, 4);
weight = AA7050 (:,5);
% Define average true strain rate and homologous temperature.
R = mean(rate(1:201));
T = (temp + 110) / (630 + 110);
% Define minimization function, boundary values and run lsqnonlin
solver.
F = Q(x)(((x(1)+x(2).*strain.^x(3)).*(1+x(4).*log(rate./R)).*(1-x(4).*log(rate./R)).*(1-x(4).*log(rate./R)).*(1-x(4).*log(rate./R)).*(1-x(4).*log(rate./R)).*(1-x(4).*log(rate./R)).*(1-x(4).*log(rate./R)).*(1-x(4).*log(rate./R)).*(1-x(4).*log(rate./R)).*(1-x(4).*log(rate./R)).*(1-x(4).*log(rate./R)).*(1-x(4).*log(rate./R)).*(1-x(4).*log(rate./R)).*(1-x(4).*log(rate./R)).*(1-x(4).*log(rate./R)).*(1-x(4).*log(rate./R)).*(1-x(4).*log(rate./R)).*(1-x(4).*log(rate./R)).*(1-x(4).*log(rate./R)).*(1-x(4).*log(rate./R)).*(1-x(4).*log(rate./R)).*(1-x(4).*log(rate./R)).*(1-x(4).*log(rate./R)).*(1-x(4).*log(rate./R)).*(1-x(4).*log(rate./R)).*(1-x(4).*log(rate./R)).*(1-x(4).*log(rate./R)).*(1-x(4).*log(rate./R)).*(1-x(4).*log(rate./R)).*(1-x(4).*log(rate./R)).*(1-x(4).*log(rate./R)).*(1-x(4).*log(rate./R)).*(1-x(4).*log(rate./R)).*(1-x(4).*log(rate./R)).*(1-x(4).*log(rate./R)).*(1-x(4).*log(rate./R)).*(1-x(4).*log(rate./R)).*(1-x(4).*log(rate./R)).*(1-x(4).*log(rate./R)).*(1-x(4).*log(rate./R)).*(1-x(4).*log(rate./R)).*(1-x(4).*log(rate./R)).*(1-x(4).*log(rate./R)).*(1-x(4).*log(rate./R)).*(1-x(4).*log(rate./R)).*(1-x(4).*log(rate./R)).*(1-x(4).*log(rate./R)).*(1-x(4).*log(rate./R)).*(1-x(4).*log(rate./R)).*(1-x(4).*log(rate./R)).*(1-x(4).*log(rate./R)).*(1-x(4).*log(rate./R)).*(1-x(4).*log(rate./R)).*(1-x(4).*log(rate./R)).*(1-x(4).*log(rate./R)).*(1-x(4).*log(rate./R)).*(1-x(4).*log(rate./R)).*(1-x(4).*log(rate./R)).*(1-x(4).*log(rate./R)).*(1-x(4).*log(rate./R)).*(1-x(4).*log(rate./R)).*(1-x(4).*log(rate./R)).*(1-x(4).*log(rate./R)).*(1-x(4).*log(rate./R)).*(1-x(4).*log(rate./R)).*(1-x(4).*log(rate./R)).*(1-x(4).*log(rate./R)).*(1-x(4).*log(rate./R)).*(1-x(4).*log(rate./R)).*(1-x(4).*log(rate./R)).*(1-x(4).*log(rate./R)).*(1-x(4).*log(rate./R)).*(1-x(4).*log(rate./R)).*(1-x(4).*log(rate./R)).*(1-x(4).*log(rate./R)).*(1-x(4).*log(rate./R)).*(1-x(4).*log(rate./R)).*(1-x(4).*log(rate./R)).*(1-x(4).*log(rate./R)).*(1-x(4).*log(rate./R)).*(1-x(4).*log(rate./R)).*(1-x(4).*log(rate./R)).*(1-x(4).*log(rate./R)).*(1-x(4).*log(ra
                        T.^x(5)) - stress).*weight;
1b = [430; 380; 0.1; 0.005; 1];
x0 = [450; 440; 0.4; 0.0075; 1.2];
ub = [470; 480; 0.5; 0.01; 1.5];
problem = createOptimProblem('lsqnonlin', 'x0', x0, 'lb', lb, 'ub'
,ub, 'objective', F, 'xdata', strain,' ydata', stress);ms =
MultiStart('PlotFcns', @gsplotbestf)
[x, fval, eflag, output, manymins] = run(ms, problem, 80);
% Assign experimental values (strain, stress, temperature, strain
rate) of each test condition to variables.
strain1 = strain(1:201);
strain2 = strain(203:390);
strain3 = strain(398:560);
strain4 = strain(565:750);
strain5 = strain(755:895);
stress1 = stress(1:201);
stress2 = stress(203:390);
stress3 = stress(398:560);
stress4 = stress(565:750);
stress5 = stress(755:895);
```

```
R1 = rate(1:201);
R2 = rate(203:390);
R3 = rate(398:560);
R4 = rate(565:750);
R5 = rate(755:895);
T1 = T(1:201);
T2 = T(203:390);
T3 = T(398:560);
T4 = T(565:750);
T5 = T(755:895);
% Evaluate Johnson Cook model stress using solved model parameters for
each experiment condition.
JC1 = (x(1)+x(2).*strain1.^x(3)).*(1+x(4).*log(R1./R)).*(1-T1.^x(5));
JC2 = (x(1)+x(2).*strain2.^x(3)).*(1+x(4).*log(R2./R)).*(1-T2.^x(5));
JC3 = (x(1)+x(2).*strain3.^x(3)).*(1+x(4).*log(R3./R)).*(1-T3.^x(5));
JC4 = (x(1)+x(2).*strain4.^x(3)).*(1+x(4).*log(R4./R)).*(1-T4.^x(5));
JC5 = (x(1)+x(2).*strain5.^x(3)).*(1+x(4).*log(R5./R)).*(1-T5.^x(5));
% Evaluate mean-squared error (MSE) and R2(NRMSE) values between each
measured stress and fitted stress.
cost func = 'MSE';
ms1 = goodnessOfFit(JC1, stress1, cost func);
ms2 = goodnessOfFit(JC2, stress2, cost func);
ms3 = goodnessOfFit(JC3, stress3, cost func);
ms4 = goodnessOfFit(JC4, stress4, cost func);
ms5 = goodnessOfFit(JC5, stress5, cost func);
cost func = 'NMSE';
r1 = goodnessOfFit(JC1, stress1, cost func);
r2 = goodnessOfFit(JC2, stress2, cost func);
r3 = goodnessOfFit(JC3, stress3, cost func);
r4 = goodnessOfFit(JC4, stress4, cost func);
r5 = goodnessOfFit(JC5, stress5, cost func);
% Evaluate mean-squared error (MSE) and R2 (NRMSE) values for the
measured stress and fitted stress altogether.
JC = (x(1)+x(2).*strain.^x(3)).*(1+x(4).*log(rate./R)).*(1-T.^x(5));
cost func = 'MSE';
ms = goodnessOfFit(JC, stress, cost func);
cost func = 'NMSE';
r = goodnessOfFit(JC, stress, cost func);
```

116